Hyphenation of scanning electrochemical microscopy with other instrumental systems

Dissertation

Zur Erlangung des Doktorgrades (Dr. rer. nat.) an der

Naturwissenschaftlichen Fakultät IV

– Chemie und Pharmazie –

der Universität Regensburg

vorgelegt von

Stefan Wert

aus Waldkraiburg

15.04.2021

Die vorgelegte Dissertation entstand im Zeitraum zwischen April 2018 und April 2021 am Institut für Analytische Chemie, Chemo- und Biosensorik der Fakultät Chemie und Pharmazie der Universität Regensburg.

Die Arbeit wurde angeleitet von Prof. Dr. Frank-Michael Matysik.

Das Promotionsgesuch wurde eingeleitet am: 15.04.2021

Termin des Kolloquiums: 18.06.2021

Der Prüfungsausschuss setzte sich zusammen aus:

Prüfungsvorsitz: Prof. Dr. Alkwin Slenczka

Erstgutachter: Prof. Dr. Frank-Michael Matysik

Zweitgutachter: Prof. Dr. Gerd-Uwe Flechsig

Drittprüfer: Prof. Dr. Werner Kunz

Danksagung

Vorab möchte ich mich hiermit bei allen Personen bedanken, die mich auf meinem Weg vom Studium bis zur Promotion begleitet haben.

Mein besonderer Dank gilt dabei:

Herrn Prof. Dr. Frank-Michael Matysik für die intensive Betreuung der Arbeit und die wertvollen Diskussionen.

Herrn Prof. Dr. Gerd-Uwe Flechsig für die Tätigkeit als Zweitgutachter und –Prüfer.

Herrn Prof. Dr. Werner Kunz für die Tätigkeit als Drittprüfer.

Herrn Prof. Dr. Alkwin Slenczka für den Vorsitz des Prüfungsausschusses.

Dr. Timo Raith, der mich durch die vielen persönlichen und fachlichen Ratschläge geprägt und inspiriert hat und mich bereits während der Masterarbeit betreut hat.

Dr. Christian Iffelsberger aufgrund der vielen wissenschaftlichen Diskussionen und Anreize, sowie seinem wertvollen Beitrag zu mehreren Publikationen. Insbesondere bin ich ihm dankbar für das Ermöglichen meines Forschungsaufenthalts am CEITEC.

Prof. Dr. Martin Pumera für die Aufnahme als Forschungspraktikant in seiner Arbeitsgruppe am CEITEC. Besonders dankbar bin ich für die Perspektive, als Postdoktorand Teil seiner Arbeitsgruppe zu werden.

Der Bayerisch-Tschechischen Hochschulagentur und dem Erasmus-Programm für die finanzielle Unterstützung während meines Forschungsaufenthalts.

Allen Mitgliedern des AK Matysik für die großartige Arbeitsatmosphäre, Hilfsbereitschaft und die gemeinsam erlebten Momente.

Meinen Freunden und meiner Familie für den stetigen Rückhalt und die Unterstützung in allen Lebenslagen.

Table of contents

List of publications

Development and characterization of electrochemical flow cells for hydrodynamic scanning electrochemical microscopy

Timo Raith, Stefan Wert, Christian Iffelsberger, Frank-Michael Matysik

Monatshefte für Chemie - Chemical Monthly 149 (2018) 1671–1677.

Abstract:

In the frame of this contribution, two electrochemical flow cells developed for scanning electrochemical microscopy (SECM) are presented. Forced convection was generated by a flow of the mediator solution through the flow cells. A description of the mandatory design aspects of the experimental flow cell setups is included. Using a macroscopic working electrode as a substrate electrode, forced convection leads to the formation of a stable diffusion layer during amperometric experiments in contrast to a growing diffusion layer in quiescent solution. To characterize the effects of forced convection, the diffusion layer around a platinum substrate electrode integrated into the cells was investigated utilizing chronoamperometric measurements and hydrodynamic SECM imaging in amperometric substrate generation/tip collection (SG/TC) mode. Both methods proved the stability and the time independency of the diffusion layer. Mathematical simulations using COMSOL Multiphysics were computed to investigate the flow profile generated by the flowing mediator solution in the relevant region close to the substrate electrode. In summary, two different electrochemical flow cells for SECM were developed and characterized. Both cell designs enabled steady-state diffusion layer characteristics at a macroscopic substrate electrode offering interesting possibilities such as time-independent measurements in the context of the SG/TC mode.

Scanning Electrochemical Microscopy of Electrically Heated Wire Substrates

Stefan Wert, Alexander Fußstetter, Christian Iffelsberger, Frank-Michael Matysik

Molecules 25 (2020) 1169.

Abstract:

We report a new configuration for enhancing the performance of scanning electrochemical microscopy (SECM) via heating of the substrate electrode. A flattened Pt microwire was

employed as the substrate electrode. The substrate was heated by an alternating current (AC), resulting in an increased mass transfer between the wire surface and the bulk solution. The electrochemical response of the Pt wire during heating was investigated by means of cyclic voltammetry (CV). The open circuit potential (OCP) of the wire was recorded over time, while varied heating currents were applied to investigate the time needed for establishing steady-state conditions. Diffusion layer studies were carried out by performing probe approach curves (PACs) for various measuring modes of SECM. Finally, imaging studies of a heated substrate electrode surface, applying feedback, substrate generation/tip collection (SG/TC), and the competition mode of SECM, were performed and compared with room temperature results.

A cost-efficient approach for simultaneous scanning electrochemical microscopy and scanning ion conductance microscopy

Stefan Wert, Simona Baluchová, Karolina Schwarzová-Pecková, Silvia Sedláková, Andrew Taylor, Frank-Michael Matysik

Monatshefte für Chemie - Chemical Monthly 151 (2020) 1249-1255.

Abstract:

A novel and cost-efficient probe fabrication method yielding probes for performing simultaneous scanning electrochemical microscopy (SECM) and scanning ion conductance microscopy (SICM) is presented. Coupling both techniques allows distinguishing topographical and electrochemical activity information obtained by SECM. Probes were prepared by deposition of photoresist onto platinum-coated, pulled fused silica capillaries, which resulted in a pipette probe with an integrated ring ultramicroelectrode. The fabricated probes were characterized by means of cyclic voltammetry and scanning electron microscopy. The applicability of probes was demonstrated by measuring and distinguishing topography and electrochemical activity of a model substrate. In addition, porous boron-doped diamond samples were investigated via simultaneously performed SECM and SICM.

Flow reactor: highly spatially resolved catalyst formation and in operando monitoring of the catalytic activity

Christian Iffelsberger, Stefan Wert, Frank-Michael Matysik, Martin Pumera

Submitted for publication.

Abstract:

Flow reactors are of increasing importance and became crucial devices due to their wide application in chemical synthesis, electrochemical hydrogen evolution reaction (HER) or electrochemical wastewater treatment. In many of these applications, catalyst materials such as transition metal chalcogenides (TMC) for HER are providing the desired electrochemical reactivity. Generally, the flow electrolyzers' performance is evaluated as overall output, but the decrease in activity of the electrolyzer is due to localized failure of the catalyst. Herein, we present a method for the highly spatially resolved (tens of micrometers) in-situ analysis of the catalytic activity under real operation conditions as well as the localized deposition of the catalyst in an operating model flow reactor. For these purposes, scanning electrochemical microscopy was applied for MoS_x catalyst deposition as well as for localized tracking of the TMC activity with a resolution of 25 µm. This approach offers detailed information about the catalytic performance and should find broad application for the characterization and optimization of flow reactor catalysis under real operation conditions.

Development of a temperature-pulse enhanced electrochemical glucose biosensor and characterization of its stability via scanning electrochemical microscopy

Stefan Wert, Heiko Iken, Michael J. Schöning, Frank-Michael Matysik

Electroanalysis 33 (2021).

Abstract:

Glucose oxidase (GOx) is an enzyme frequently used in glucose biosensors. We investigated the impact of temperature pulses on GOx that was drop-coated on flattened Pt microwires. The wires were heated by an alternating current according to the concept of hot-wire electrochemistry. The sensitivity towards glucose and the temperature stability of GOx was investigated by amperometric techniques. An up to 22-fold increase of sensitivity was observed. Localized enzyme activity changes were investigated via scanning electrochemical microscopy (SECM). The application of short (<100 ms) heat pulses to the sensor was associated with less thermal inactivation of the immobilized GOx than long-term heating.

Edges more electroactive than basal planes in crystalline TiS_2 and $TiSe_2$

Stefan Wert, Christian Iffelsberger, Katarina Novčić, Frank-Michael Matysik, Martin Pumera

Submitted for publication.

Abstract:

Layered materials and derived 2D material couples such as graphite/graphene, layered and single layer pnictogens (i.e., black phosphorus and phosphorene) and transition metal dichalcogenides (TMDs) have gained a lot of attention due to their electrocatalytic properties and as potential materials for energy storage. It was shown that graphite, MoS_2 and pnictogens show faster electron transfer at the edges of crystals and defects than on the basal plane. The persisting question is if this is a general trend in nature. To come closer to the answer of this question, we studied TiS_2 and $TiSe_2$ regarding their local catalytic activity via scanning electrochemical microscopy (SECM). Both TMDs have shown increased catalytic activity near edges and defects, and decreased activity was observed at surfaces with higher oxygen content. For correlation, optical and topographical analysis was performed via scanning electron microscopy (SEM) and atomic force microscopy (AFM). We show that so far, the higher electroactivity at edges and defects is persistent across the layered materials. This is of huge industrial and scientific importance and there are very important implications for applications of layered materials.

Conference contributions

Oral presentations

2nd Cross-Border Seminar on Electroanalytical Chemistry, 10-12.04.2019, České Budějovice, Czech Republic:

A simple technique for the fabrication of ring ultramicroelectrode pipette tips for combined scanning electrochemical microscopy and scanning ion conductance microscopy

7th Regional Symposium on Electrochemistry for South-East Europe/ Kurt Schwabe Symposium – Satellite Regional Student Symposium on Electrochemistry, 25-30.05.2019, Split, Croatia:

Hyphenation of scanning electrochemical microscopy and scanning ion conductance microscopy using photoresist-coated micropipettes

15th International Students Conference 'Modern Analytical Chemistry', 19-20.09.2019, Prague, Czech Republic:

Novel probe fabrication method for simultaneous scanning electrochemical microscopy and scanning ion conductance microscopy measurements

3rd Cross-Border Seminar on Electroanalytical Chemistry, 08-09.04.2021, Regensburg, Germany:

Development of a temperature-pulse enhanced electrochemical glucose biosensor and characterization of its stability via scanning electrochemical microscopy

Poster contributions

Electrochemistry 2018, 24-26.09.2018, Ulm, Germany:

Development and optimization of an electrochemical flow cell configuration for hydrodynamic scanning electrochemical microscopy

ANAKON 2019, 25-28.03.2019, Münster, Germany:

Development and optimization of an electrochemical flow cell configuration for hydrodynamic scanning electrochemical microscopy

ANAKON 2019, 25-28.03.2019, Münster, Germany:

Fabrication of ring disk ultramicroelectrodes for the hyphenation of scanning electrochemical microscopy and scanning ion conductance microscopy

7th Regional Symposium on Electrochemistry for South-East Europe/ Kurt Schwabe Symposium, 25-30.05.2019, Split, Croatia:

A simple approach for the preparation of ring ultramicroelectrodes in the context of combined scanning electrochemical microscopy and scanning ion conductance microscopy

Declaration of collaboration

The author performed the major amount of work presented in this thesis. Nevertheless, some results were obtained in collaboration with other researchers. According to § 8 Abs. 1 Satz 2 Punkt 7 of the Ordnung zum Erwerb des akademischen Grades eines Doktors der Naturwissenschaften (Dr. rer. nat.) an der Universität Regensburg vom 18. Juni 2009, this section describes the scope of said collaborations.

A cost-efficient approach for simultaneous scanning electrochemical microscopy and scanning ion conductance microscopy

Conceptual design and writing were done by the author, except for the experimental details describing the preparation of porous boron-doped diamond, which was written by Simona Baluchová. Said samples were provided by Simona Baluchová as well and were fabricated by Silvia Sedláková and Andrew Taylor. SECM measurements were performed by the author and Simona Baluchová. SEM imaging of probes was done with the help of Evgeny Melekhov. Graphical illustrations were prepared in collaboration with Dr. Thomas Herl. Prof. Dr. Frank-Michael Matysik, Simona Baluchová and Dr. Timo Raith were involved in discussions. The work was supervised by Dr. Karolina Schwarzová-Pecková and Prof. Dr. Frank-Michael Matysik.

Scanning Electrochemical Microscopy of Electrically Heated Wire Substrates

Conceptual design and writing were done by the author. Dr. Christian Iffelsberger developed the device used for the heating of substrates and conducted preliminary experiments regarding the fabrication of substrates. Alexander Fußstetter performed the temperature calibration. Graphical illustrations were prepared in collaboration with Dr. Thomas Herl. Dr. Christian Iffelsberger, Prof. Dr. Frank-Michael Matysik and Dr. Timo Raith were involved in discussions. Prof. Dr. Frank-Michael Matysik supervised the project.

Development of a temperature-pulse enhanced electrochemical glucose biosensor and characterization of its stability via scanning electrochemical microscopy

Conceptual design, writing, and measurements were done by the author. The drop-coating of glucose oxidase was done with the help of Heiko Iken and Prof. Dr. Michael J. Schöning. Dr. Thomas Herl contributed to the design of the graphical illustrations. Dr. Christian Iffelsberger and Prof. Dr. Frank-Michael Matysik were involved in discussions. Prof. Dr. Frank-Michael Matysik supervised the project.

Flow reactor: highly spatially resolved catalyst formation and in operando monitoring of the catalytic activity

The design and 3D printing were done in by Dr. Christian Iffelsberger. The author performed and analyzed the electrochemical characterization of the flow cell. Dr. Christian Iffelsberger performed and analyzed the localized electrochemical deposition of MoS_x and the associated experiments for HER characterization. Prof. Dr. Frank-Michael Matysik and Prof. Dr. Martin Pumera supervised this work. Dr. Christian Iffelsberger and Prof. Dr. Martin Pumera originated the idea. The manuscript was written through contributions of all persons involved in the project.

Edges more electroactive than basal planes in crystalline TiS_2 and $TiSe_2$

Writing of the manuscript was done by the author. The conceptual design was done in cooperation with Dr. Christian Iffelsberger and Prof. Dr. Martin Pumera. Katarina Novčić developed the sample preparation procedure. The author recorded scanning electrochemical micrographs. Dr. Christian Iffelsberger performed scanning electron microscopy, energy-dispersive X-ray spectroscopy, and atomic force microscopy measurements. Dr. Christian Iffelsberger, Prof. Dr. Martin Pumera, and Prof. Dr. Matysik were involved in discussions and supervised the project.

List of abbreviations

a_i	Activity of species i	
A	Area	[m^2]
AFM	Atomic force microscopy	
BDD	Boron-doped diamond	
c_i	Concentration of species i	[mol L^{-1} or M]
c_0	Bulk concentration	[mol L^{-1} or M]
C	Capacity	[F]
CE	Counter electrode	
CLSM	Confocal laser scanning microscope	
CV	Cyclic voltammetry/ voltammogram	
d	Substrate-to-tip distance	[m]
D	Diffusion coefficient	[cm^2 s^{-1}]
DE	Detection electrode	
e^-	Electron	
E	Potential	[V]
E_A	Activation energy	[J mol^{-1}]
E_0	Standard potential	[V]
$E_{0'}$	Formal standard potential	[V]
EAM	Electrochemical additive manufacturing	
EDS	Energy dispersive X-ray spectroscopy	
F	Faraday constant	[9.64853×10^4 C mol^{-1}]
FcMeOH	Ferrocenemethanol	
FFM	Fused filament modeling	
GC	Glassy carbon	

GOx	Glucose oxidase	
HER	Hydrogen evolution reaction	
HPLC	High performance liquid chromatography	
I	Current	[A]
I_C	Capacitive current	[A]
I_L	Limiting current	[A]
IHP	Inner Helmholtz plane	
J	Flux of species	[mol cm^{-2} s^{-1}]
k	Reaction rate	[mol m^{-2} s^{-1}]
k_B	Boltzmann constant	[1.38065×10^{-23} m^2 kg s^{-2} K^{-1}]
L	Normalized distance	
n	Amount of substance	[mol]
O	Oxidized species	
OHP	Outer Helmholtz plane	
PAC	Probe approach curve	
PEEK	Polyether ether ketone	
PLA	Polylactic acid	
PSC	Probe scan curve	
PTFE	Polytetrafluoroethylene	
R	Universal gas constant	[8,31447 J mol^{-1} K^{-1}]
	Resistance	[Ω]
	Reduced species	
r	Radius	[m]
RE	Reference electrode	
RG	RG value	
SECM	Scanning electrochemical microscope(y)	
SEM	Scanning electron microscope(y)	

SG/TC	Substrate generation/tip collection	
SICM	Scanning ion conductance microscopy	
STL	Standard triangle language	
T	Temperature	[K]
t	Time	[s]
TG/SC	Tip generation/substrate collection	
TMC/TMD	Transition metal chalcogenide / dichalcogenide	
UME	Ultramicroelectrode	
WE	Working electrode	
x	Distance	[m]
z	Number of exchanged electrons	
δ	Diffusion layer thickness	[m]
η	Dynamic viscosity	[Pa s]
ν	Flow velocity	[m s^{-1}]
Φ	Electric potential	[V]

1. Introduction

Since its origins in the late 1980s [1, 2], scanning electrochemical microscopy (SECM) has evolved into an established scanning probe technique for the investigation of electrochemical activity and topography of surfaces. Generally, it involves a small electrode employed as probe, where redox-active species can be converted, yielding a current as imaging signal. This technique is frequently used in corrosion research [3–7], investigation of biological samples involving enzyme [8, 9] and cell studies [10–14], as well as material characterization [15–20]. Over the years, instrumental advancements including novel measurement modes [21–26] and probe fabrication methods [27–31] were described.

Moreover, an increasing interest in coupling SECM with other scanning probe techniques has emerged. As a result, SECM was coupled with various other methods, including atomic force microscopy (AFM) [3, 32–34], mass spectrometry [35], optical microscopy [36], and scanning ion conductance microscopy (SICM) [37–45]. The latter is a scanning probe technique introduced by Prater et al. [46], which similarly to SECM allows for non-contact characterization of surfaces, revealing morphological properties. As performing SECM and SICM in parallel delivers both electrochemical and topographical information, one goal of the thesis was the development of a cost-efficient method for SECM-SICM probe fabrication, which, in contrast to the established protocols, requires no sophisticated equipment.

Another aspect of the thesis was expanding the field of SECM performed under the impact of forced convection. In the past 5 years, the Matysik group has published multiple studies, showing that forced convection generated by either stirring the solution [47–50] or employing a flow cell [51] increases resolution and reproducibility of SECM images. To simplify the latter approach, a 3D printed flow cell powered by a syringe pump was characterized in cooperation with Dr. Christian Iffelsberger.

Similar to forced convection, elevated temperatures can increase mass transport due to electrothermal fluid flow, which consequently leads to more species converted at electrodes and higher currents measured [52]. A convenient way to realize fast temperature adjustments is using “hot-wire electrochemistry”, where microwires are heated by a high-frequency alternating current [53, 54]. In this thesis, the aim was to develop a setup, which enables the heating of the substrate via alternating current. The system was consecutively utilized for the localized characterization of the enzyme activity of glucose oxidase under the influence of elevated temperatures.

References

1. Bard AJ, Fan FRF, Kwak J, Lev O (1989) Scanning electrochemical microscopy. Introduction and principles. Anal. Chem. 61(2):132–138
2. Engstrom RC, Pharr CM (1989) Scanning electrochemical microscopy. Anal. Chem. 61(19):1099A-1104A
3. Davoodi A, Pan J, Leygraf C, Norgren S (2005) In Situ Investigation of Localized Corrosion of Aluminum Alloys in Chloride Solution Using Integrated EC-AFM/SECM Techniques. Electrochem. Solid-State Lett. 8(6):B21
4. Hampel M, Schenderlein M, Schary C, Dimper M, Ozcan O (2019) Efficient detection of localized corrosion processes on stainless steel by means of scanning electrochemical microscopy (SECM) using a multi-electrode approach. Electrochem. Commun. 101:52–55
5. Jamali SS, Moulton SE, Tallman DE, Forsyth M, Weber J, Wallace GG (2014) Applications of scanning electrochemical microscopy (SECM) for local characterization of AZ31 surface during corrosion in a buffered media. Corros. Sci. 86:93–100
6. Nickchi T, Rostron P, Barsoum I, Alfantazi A (2019) Measurement of local galvanic surface corrosion using scanning electrochemical microscopy on ductile cast iron. J. Mater. Sci. 54(12):9213–9221
7. Simões AM, Bastos AC, Ferreira MG, González-García Y, González S, Souto RM (2007) Use of SVET and SECM to study the galvanic corrosion of an iron–zinc cell. Corros. Sci. 49(2):726–739
8. Gdor E, Shemesh S, Magdassi S, Mandler D (2015) Multienzyme Inkjet Printed 2D Arrays. ACS Appl. Mater. Interfaces 7(32):17985–17992
9. Nogala W, Szot K, Burchardt M, Roelfs F, Rogalski J, Opallo M, Wittstock G (2010) Feedback mode SECM study of laccase and bilirubin oxidase immobilised in a sol-gel processed silicate film. Analyst 135(8):2051–2058
10. Conzuelo F, Schulte A, Schuhmann W (2018) Biological imaging with scanning electrochemical microscopy. Proc. R. Soc. A 474(2218):20180409
11. Henderson JD, Filice FP, Li MSM, Ding Z (2017) Tracking Live-Cell Response to Hexavalent Chromium Toxicity by using Scanning Electrochemical Microscopy. ChemElectroChem 4(4):856–863
12. Nebel M, Grützke S, Diab N, Schulte A, Schuhmann W (2013) Visualization of oxygen consumption of single living cells by scanning electrochemical microscopy: the influence of the faradaic tip reaction. Angew. Chem. Int. Ed. 52(24):6335–6338

13. Ramanavicius A, Morkvenaite-Vilkonciene I, Kisieliute A, Petroniene J, Ramanaviciene A (2017) Scanning electrochemical microscopy based evaluation of influence of pH on bioelectrochemical activity of yeast cells - Saccharomyces cerevisiae. Colloids Surf. B 149:1–6

14. Takahashi Y, Shevchuk AI, Novak P, Babakinejad B, Macpherson J, Unwin PR, Shiku H, Gorelik J, Klenerman D, Korchev YE, Matsue T (2012) Topographical and electrochemical nanoscale imaging of living cells using voltage-switching mode scanning electrochemical microscopy. Proc. Natl. Acad. Sci. U.S.A. 109(29):11540–11545

15. Ben Jadi S, El Guerraf A, Kiss A, El Azrak A, Bazzaoui EA, Wang R, Martins JI, Bazzaoui M (2020) Analyses of scanning electrochemical microscopy and electrochemical impedance spectroscopy in direct methanol fuel cells: permeability resistance and proton conductivity of polyaniline modified membrane. J. Solid State Electrochem 24(7):1551–1565

16. Filotás D, Fernández-Pérez BM, Nagy L, Nagy G, Souto RM (2020) A novel scanning electrochemical microscopy strategy for the investigation of anomalous hydrogen evolution from AZ63 magnesium alloy. Sens. Actuator B Chem. 308:127691

17. Kim J, Renault C, Nioradze N, Arroyo-Currás N, Leonard KC, Bard AJ (2016) Electrocatalytic Activity of Individual Pt Nanoparticles Studied by Nanoscale Scanning Electrochemical Microscopy. J. Am. Chem. Soc. 138(27):8560–8568

18. Mirkin MV, Sun T, Yu Y, Zhou M (2016) Electrochemistry at One Nanoparticle. Acc. Chem. Res. 49(10):2328–2335

19. O'Connell MA, Lewis JR, Wain AJ (2015) Electrochemical imaging of hydrogen peroxide generation at individual gold nanoparticles. Chem. Commun. (Cambridge, England) 51(51):10314–10317

20. Shi W, Baker LA (2015) Imaging heterogeneity and transport of degraded Nafion membranes. RSC Adv. 5(120):99284–99290

21. Wipf DO, Bard AJ, Tallman DE (1993) Scanning electrochemical microscopy. 21. Constant-current imaging with an autoswitching controller. Anal. Chem. 65(10):1373–1377

22. Eckhard K, Chen X, Turcu F, Schuhmann W (2006) Redox competition mode of scanning electrochemical microscopy (RC-SECM) for visualisation of local catalytic activity. Phys. Chem. Chem. Phys. 8(45):5359–5365

23. James PI, Garfias-Mesias L.F., Moyer P.J., Smyrl W.H. (1998) Scanning Electrochemical Microscopy with Simultaneous Independent Topography. J. Electrochem. Soc. 145(4):L64

24. Koch JA, Baur MB, Woodall EL, Baur JE (2012) Alternating current scanning electrochemical microscopy with simultaneous fast-scan cyclic voltammetry. Anal. Chem. 84(21):9537–9543

25. Nebel M, Eckhard K, Erichsen T, Schulte A, Schuhmann W (2010) 4D shearforce-based constant-distance mode scanning electrochemical microscopy. Anal. Chem. 82(18):7842–7848

26. Zigah D, Rodríguez-López J, Bard AJ (2012) Quantification of photoelectrogenerated hydroxyl radical on TiO_2 by surface interrogation scanning electrochemical microscopy. Phys. Chem. Chem. Phys. 14(37):12764–12772

27. Bach CE, Nichols RJ, Beckmann W, Meyer H, Schulte A, Besenhard JO, Jannakoudakis PD (1993) Effective Insulation of Scanning Tunneling Microscopy Tips for Electrochemical Studies Using an Electropainting Method. J. Electrochem. Soc. 140(5):1281

28. Liljeroth P, Johans C, Slevin CJ, Quinn BM, Kontturi K (2002) Micro ring–disk electrode probes for scanning electrochemical microscopy. Electrochem. Commun. 4(1):67–71

29. Liu B, Rolland JP, DeSimone JM, Bard AJ (2005) Fabrication of ultramicroelectrodes using a "teflon-like" coating material. Anal. Chem. 77(9):3013–3017

30. Schulte A, Chow RH (1996) A simple method for insulating carbon-fiber microelectrodes using anodic electrophoretic deposition of paint. Anal. Chem. 68(17):3054–3058

31. Sun P, Zhang Z, Guo J, Shao Y (2001) Fabrication of nanometer-sized electrodes and tips for scanning electrochemical microscopy. Anal. Chem. 73(21):5346–5351

32. Macpherson JV, Unwin PR (2000) Combined scanning electrochemical-atomic force microscopy. Anal. Chem. 72(2):276–285

33. Kueng A, Kranz C, Lugstein A, Bertagnolli E, Mizaikoff B (2003) Integrated AFM-SECM in tapping mode: simultaneous topographical and electrochemical imaging of enzyme activity. Angew. Chem. Int. Ed. 42(28):3238–3240

34. Velmurugan J, Agrawal A, An S, Choudhary E, Szalai VA (2017) Fabrication of Scanning Electrochemical Microscopy-Atomic Force Microscopy Probes to Image Surface Topography and Reactivity at the Nanoscale. Anal. Chem. 89(5):2687–2691

35. Momotenko D, Qiao L, Cortés-Salazar F, Lesch A, Wittstock G, Girault HH (2012) Electrochemical push-pull scanner with mass spectrometry detection. Anal. Chem. 84(15):6630–6637

36. Lee Y, Bard AJ (2002) Fabrication and characterization of probes for combined scanning electrochemical/optical microscopy experiments. Anal. Chem. 74(15):3626–3633

37. Comstock DJ, Elam JW, Pellin MJ, Hersam MC (2010) Integrated ultramicroelectrode-nanopipet probe for concurrent scanning electrochemical microscopy and scanning ion conductance microscopy. Anal. Chem. 82(4):1270–1276

38. Morris CA, Chen C-C, Baker LA (2012) Transport of redox probes through single pores measured by scanning electrochemical-scanning ion conductance microscopy (SECM-SICM). Analyst 137(13):2933–2938

39. Nadappuram BP, McKelvey K, Al Botros R, Colburn AW, Unwin PR (2013) Fabrication and characterization of dual function nanoscale pH-scanning ion conductance microscopy (SICM) probes for high resolution pH mapping. Anal. Chem. 85(17):8070–8074

40. Nadappuram BP, McKelvey K, Byers JC, Güell AG, Colburn AW, Lazenby RA, Unwin PR (2015) Quad-barrel multifunctional electrochemical and ion conductance probe for voltammetric analysis and imaging. Anal. Chem. 87(7):3566–3573

41. Page A, Kang M, Armitstead A, Perry D, Unwin PR (2017) Quantitative Visualization of Molecular Delivery and Uptake at Living Cells with Self-Referencing Scanning Ion Conductance Microscopy-Scanning Electrochemical Microscopy. Anal. Chem. 89(5):3021–3028

42. Şen M, Takahashi Y, Matsumae Y, Horiguchi Y, Kumatani A, Ino K, Shiku H, Matsue T (2015) Improving the electrochemical imaging sensitivity of scanning electrochemical microscopy-scanning ion conductance microscopy by using electrochemical Pt deposition. Anal. Chem. 87(6):3484–3489

43. Takahashi Y, Shevchuk AI, Novak P, Murakami Y, Shiku H, Korchev YE, Matsue T (2010) Simultaneous noncontact topography and electrochemical imaging by SECM/SICM featuring ion current feedback regulation. J. Am. Chem. Soc. 132(29):10118–10126

44. Takahashi Y, Shevchuk AI, Novak P, Zhang Y, Ebejer N, Macpherson JV, Unwin PR, Pollard AJ, Roy D, Clifford CA, Shiku H, Matsue T, Klenerman D, Korchev YE (2011) Multifunctional nanoprobes for nanoscale chemical imaging and localized chemical delivery at surfaces and interfaces. Angew. Chem. Int. Ed. 50(41):9638–9642

45. Takahashi Y, Ida H, Matsumae Y, Komaki H, Zhou Y, Kumatani A, Kanzaki M, Shiku H, Matsue T (2017) 3D electrochemical and ion current imaging using scanning electrochemical-scanning ion conductance microscopy. Phys. Chem. Chem. Phys. 19(39):26728–26733

46. Hansma PK, Drake B, Marti O, Gould SA, Prater CB (1989) The scanning ion-conductance microscope. Science (New York, N.Y.) 243(4891):641–643

47. Iffelsberger C, Raith T, Vatsyayan P, Vyskočil V, Matysik F-M (2018) Detection and imaging of reactive oxygen species associated with the electrochemical oxygen evolution by hydrodynamic scanning electrochemical microscopy. Electrochim. Acta 281:494–501

48. Raith T, Iffelsberger C, Vatsyayan P, Matysik F-M (2019) Impacts of Forced Convection Generated via High Precision Stirring on Scanning Electrochemical Microscopy Experiments in Feedback Mode. Electroanalysis 31(2):273–281

49. Iffelsberger C, Vatsyayan P, Matysik F-M (2017) Scanning Electrochemical Microscopy with Forced Convection Introduced by High-Precision Stirring. Anal. Chem. 89(3):1658–1664

50. Raith T, Kröninger A, Mickert MJ, Gorris HH, Matysik F-M (2020) Enhanced resolution of generator-collector studies of enzymatic structures by means of hydrodynamic scanning electrochemical microscopy. Talanta 214:120844

51. Raith T, Wert S, Iffelsberger C, Matysik F-M (2018) Development and characterization of electrochemical flow cells for hydrodynamic scanning electrochemical microscopy. Monatsh. Chem. 149(9):1671–1677

52. Gründler P (2015) In-situ thermoelectrochemistry. Working with heated electrodes. Monographs in electrochemistry. Springer, Berlin

53. Gründler P, Flechsig G-U (1998) Deposition and stripping at heated microelectrodes. Arsenic(V) at a gold electrode. Electrochim. Acta 43(23):3451–3458

54. Gründler P, Kirbs A, Zerihun T (1996) Hot-wire electrodes: voltammetry above the boiling point. Analyst 121(12):1805–1810

55. Boika A, Zhao Z (2016) First principles of hot-tip scanning electrochemical microscopy: Differentiating substrates according to their thermal conductivities. Electrochem. Commun. 68:36–39

56. Zhao Z, Leonard KC, Boika A (2019) Hot-Tip Scanning Electrochemical Microscopy: Theory and Experiments Under Positive and Negative Feedback Conditions. Anal. Chem. 91(4):2970–2977

2. Theoretical background

2.1. Electrochemistry

2.1.1. Basic principles

Electrochemistry is a discipline that is concerned with conversion processes taking place at electrode surfaces. As a potential sufficient for the conversion of an electroactive species is applied to the electrode, a reaction of the following kind occurs:

$$\mathrm{O} + \mathrm{n}e^- \rightleftharpoons \mathrm{R} \qquad \textbf{(1)}$$

A reversible reaction is depicted, where the oxidized species O is converted to the reduced species R, requiring a certain amount n of electrons e^-. The potential E of such a reaction and its relation to the concentration of the reactants is described by the Nernst equation [1, 2]:

$$\mathrm{E} = E_0 + \frac{RT}{zF} ln \frac{a_O}{a_R} \qquad \textbf{(2)}$$

Herein, E_0 describes the standard electrode potential, R the universal gas constant, T the temperature, z the number of exchanged electrons, F the Faraday constant, and $\mathrm{a_O}$ and $\mathrm{a_R}$ the activities of oxidized and reduced species, respectively. Since the activity coefficients for individual species are often unknown, a variant of the Nernst equation using the formal potential $E_{0'}$ is frequently used [1].

$$\mathrm{E} = E_{0'} + \frac{RT}{zF} ln \frac{c_O}{c_R} \qquad \textbf{(3)}$$

As $E_{0'}$ includes E_0 and the activity coefficients of both species, the concentrations c_O and c_R are used instead of the respective activities.

For the electrochemical investigation of reactions, experiments are usually carried out using three electrodes immersed into solution [1] (**Figure 2.1.1**). The first one is the working electrode (WE), where the reaction of interest takes place. Its potential is adjusted with respect to the reference electrode (RE). In order to maintain a constant potential at the RE, the counter electrode (CE) serves as “electron sink”, as electron transfer during a reaction occurs at the CE instead of the RE, as the latter usually exhibits a high resistance. Consequently, no noticeable reaction occurs at the RE that could alter the reference potential.

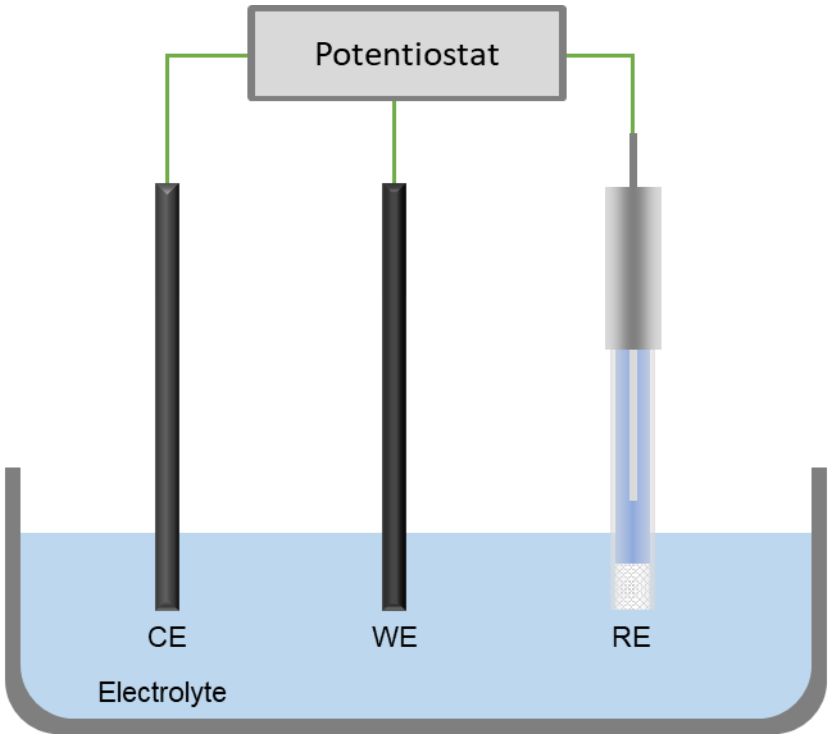

Figure 2.1.1: Three-electrode setup frequently used in electrochemical experiments. The working electrode (WE), counter electrode (CE) and reference electrode (RE) are immersed into electrolyte solution containing electroactive species. A potentiostat is required for potential and current control and readout.

2.1.2. Transport processes

When a constant potential is applied at the WE and an electroactive species reacts at its surface, two kinds of current contribute to the total current measured: The faradaic current I_F, resulting from the conversion of substance, and the capacitive current I_C, which is caused by the so-called electrical double layer formed at the electrode surface [2]. The double layer consists of ions with opposite charge, which are attracted towards the electrode in order to compensate the excess charge. Multiple models were developed over the years to describe the interfacial region. **Figure 2.1.2** depicts the “Bockris, Devanthan, Müller” model [3], taking into consideration the interactions of electrode surface, ions and solvent molecules. According to this model, the inner Helmholtz plane (IHP) at a negatively polarized electrode consists of positively charged ions and solvent molecules (and vice versa). The latter form a solvation layer at the electrode as if it was a giant ion. In the outer Helmholtz plane (OHP), solvated positively charged ions are located. Together, the IHP and OHP are referred to as the compact layer, which is very stable and able to persist even when the electrode is retrieved from solution [4]. The diffuse layer, ranging from the OHP to the bulk solution, consists of nonspecifically adsorbed ions. When a reaction takes place, an ion breaks through the IHP to be converted at the electrode surface.

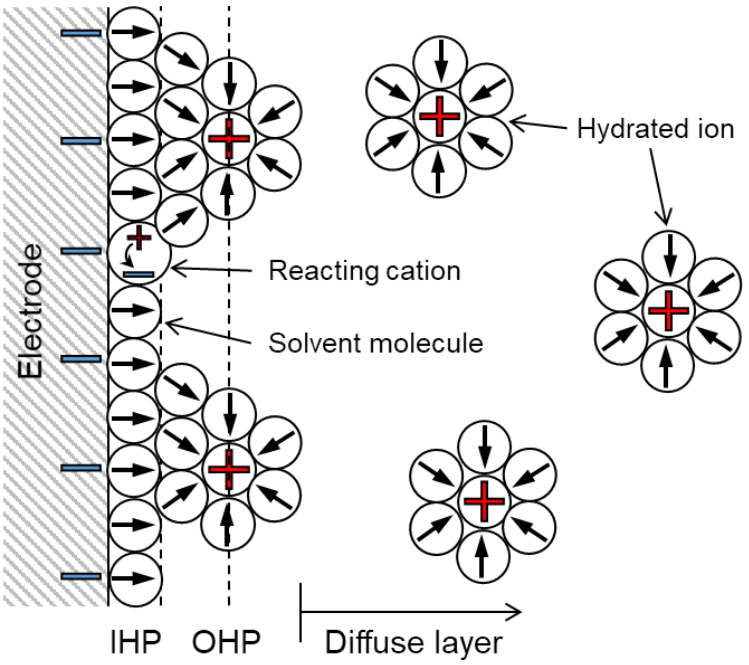

Figure 2.1.2: Bockris, Devanathan, Müller model illustrating the arrangement of ions and solvent molecules at a negatively polarized electrode surface. IHP: Inner Helmholtz plane. OHP: Outer Helmholtz plane. Adapted from [5].

The capacitive current resulting from double layer formation lasts only for up to 0.1 s upon variation of electrode potential. Its magnitude over time t can be described using equation **(4)** [2]:

$$I_C = \frac{\Delta E}{R} \exp\left(\frac{-t}{RC}\right) \quad \textbf{(4)}$$

ΔE represents the potential step, R the solution resistance, and C the double layer capacity. Outside the double layer, in the bulk solution, the movement of ions and molecules depends on multiple processes.

Diffusion, migration and potentially forced convection are the possible factors of transport within a solution. They are summed up in the Nernst-Planck equation [1, 4, 6], which describes the flux of species $J(x)$ in relation to the distance x to the electrode surface.

$$J(x) = -D\frac{\delta c(x)}{\delta x} - \frac{zF}{RT}Dc\frac{\delta \phi(x)}{\delta x} + \upsilon c(x) \quad \textbf{(5)}$$

It contains the diffusion coefficient D, the concentration gradient $\delta c(x)/\delta x$ at distance x, the universal gas constant R, temperature T, Faraday constant F, the charge of the species of interest z and its concentration c, the potential difference $\delta\phi(x)/\delta x$ at distance x, and the convective term υ. The first part is derived from Fick's first law and represents the diffusion term, stating that the flux deriving from diffusion is proportional to the concentration gradient. It is followed by the term describing the migration of charged species. The last term includes

the effect of forced convection applied to the system, thus having no impact in quiescent solution. By the addition of a high concentration of supporting electrolyte consisting of charged, non-electroactive ions, migration effects affecting the electroactive species of interest can be minimized. The addition of supporting electrolytes is associated with further benefits. The reduction of solution resistance connected with a lower i-R drop leads to an enhanced potential accuracy between working and reference electrode. In addition, the supporting electrolyte can be used for setting the reaction conditions such as pH and ionic strength [4].

At the electrode surface, the diffusion process consists of two separate types of diffusion [2, 7]. On the one hand, the lateral diffusion, which is the species transport oriented perpendicular to the electrode surface, and on the other hand the spherical diffusion appearing at spherical electrodes or at the edges of flat electrodes. Both processes are illustrated in **Figure 2.1.3** in case of a planar macroelectrode.

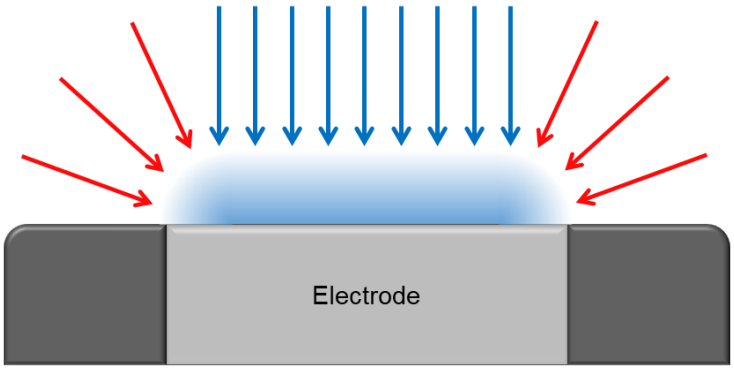

Figure 2.1.3: Lateral (blue) and radial (red) diffusion at a macroelectrode surface. Adapted from [7].

These diffusion processes result from the conversion of electroactive species and can be described by solving Fick´s second law, given in equation **(6)**. It is derived from the first law (first term in equation **(5)**), considering both in- and outflow of species over time [2].

$$\frac{\partial c}{\partial t} = D\nabla^2 c \qquad \textbf{(6)}$$

By modifying the Laplacian operator ∇^2, the diffusion processes for different electrode geometries can be characterized. In the cases of lateral and spherical diffusion, equations **(7)** and **(8)** need to be applied, respectively [1].

$$\frac{\partial c(x,t)}{\partial t} = D\frac{\partial^2 c(x,t)}{\partial x^2} \qquad \textbf{(7)}$$

$$\frac{\partial c(x,t)}{\partial t} = D\left(\frac{\partial^2 c(r,t)}{\partial r^2} + \frac{2}{r}\frac{\partial c(r,t)}{\partial r}\right) \qquad \textbf{(8)}$$

Solving both of these equations yields equations **(9)** and **(10)**, which are used to describe the electrochemical current measured at electrodes of planar and spherical shape, respectively [1].

$$I_{planar} = \frac{nFA\sqrt{D}c_0}{\sqrt{\pi t}} \quad \textbf{(9)}$$

$$I_{spherical} = \frac{nFA\sqrt{D}c_0}{\sqrt{\pi t}} + \frac{nFADc_0}{r_s} \quad \textbf{(10)}$$

In equation **(9)**, also known as the Cottrell equation, n, F, A, D, and c_0 correspond to the amount of converted species, the Faraday constant, the electrode area, the diffusion coefficient, and the bulk concentration of electroactive substance, respectively. Assuming the reactant is initially distributed homogeneously in solution, the Cottrell equation describes the current deriving from analyte conversion with respect to the growing concentration gradient evolving over time. A purely lateral diffusion is attributed to this equation, which is a suitable approximation in case of macroelectrodes as the contribution of radial diffusion is minor. For spherical electrodes, the Cottrell equation is extended by a term for the radial diffusion, including the radius of the sphere r_s. Notably, this addition is time-independent, thus the radial diffusion does not contribute to diffusion layer growth over time. In addition, for decreasing electrode size, an increasing radial diffusion behavior is expected [7].

2.1.3. Ultramicroelectrodes

Ultramicroelectrodes (UMEs) are generally considered to be electrodes with an electroactive diameter of <25 µm. These dimensions result in a different diffusion at the electrode surface compared to macroelectrodes [7]. A diffusion behavior similar to small spherical electrodes is observed, however more complex due to a non-uniform current density originating from its geometry. In short summary, solving Fick´s second law results in the following expression [7, 8]:

$$I_{UME} = \frac{4nFADc_0}{\pi r_0} f(\tau) \quad \textbf{(11)}$$

Herein, $f(\tau)$ is a dimensionless, time-dependent term, and r_0 is the electrode radius. At short reaction times, a linear diffusion occurs. As time proceeds and a diffusion layer thickness similar to the electrode radius is reached, the radial diffusion becomes more dominant. Eventually, a hemispherical diffusion field is established, generally in a matter of milliseconds with shorter times required for smaller electrodes. In addition, a steady-state current according to the following equation is reached as $f(\tau)$ approaches a value of 1 [9]:

$$I_{UME} = 4nFDc_0r_0 \quad \textbf{(12)}$$

The diffusion layer development at UMEs is shown schematically in **Figure 2.1.4**. As soon as a steady-state diffusion layer is reached, the rate of species conversion is equal to the amount of fresh species diffusing towards the electrode surface [7]. The fast steady-state establishment makes UMEs a practical tool for many voltammetric techniques, and crucial for the employment as probes in SECM, as will be discussed later.

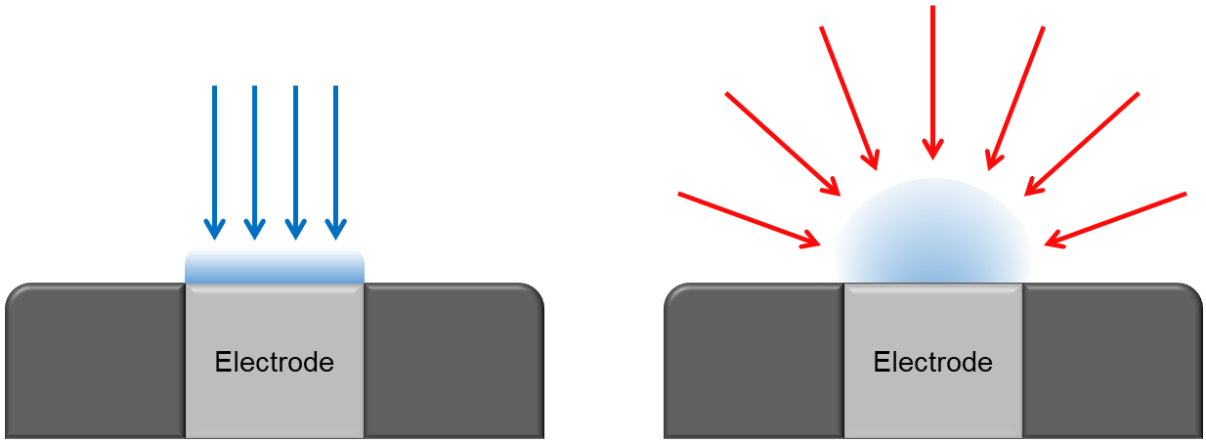

Figure 2.1.4: Diffusion layer formation at UMEs. Initially, linear growth is predominant (left). As a certain diffusion layer thickness is reached, the impact of radial diffusion increases, and a steady state is established (right). Adapted from [7].

2.1.4. Voltammetry

In general, the term “voltammetry” sums up all experiments including the application of (varying) working electrode potentials connected with the monitoring of the resulting current. In the simplest voltammetric experiment, chronoamperometry, a constant potential sufficient for species conversion is applied and the resulting current is measured over time [10].

In **Figure 2.1.5**, exemplary chronoamperograms recorded at a macroelelctrode and an UME are shown. Initially, when the potential is applied, both capacitive and faradaic current sum up to a very high current [2, 7]. Since the electrode surface is usually charged in a matter of milliseconds the capacitive current has no impact thereafter. The faradaic current is initially high due to a large amount of electroactive species being close to the electrode surface. As measurement time proceeds, differences in current response between macroelectrodes and UMEs become apparent. In both cases, a concentration gradient is formed because of analyte conversion. However, due to the respective growth of diffusion layers discussed in the chapters before, steady-state currents are reached faster in case of UMEs compared to macroelectrodes [2].

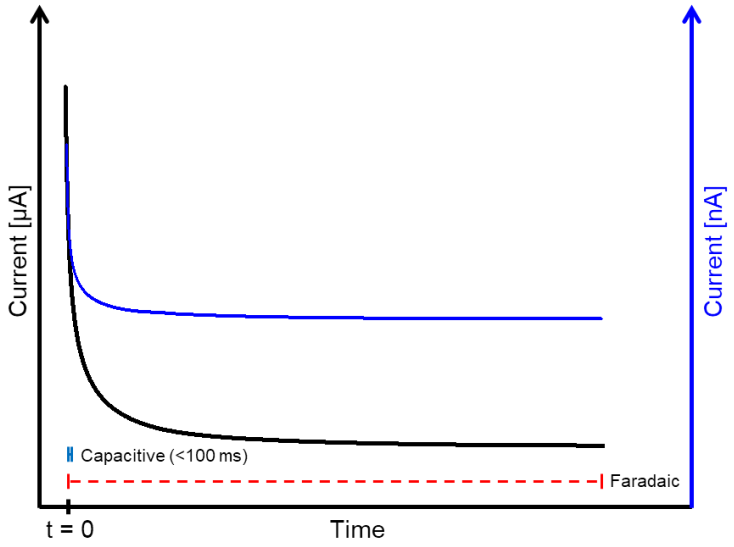

Figure 2.1.5: Development of current during a chronoamperometric experiment at macroelectrodes (black) vs ultramicroelectrodes (blue). The time periods during which capacitive and faradaic current contribute to the overall current are indicated.

A commonly applied technique for the electrochemical investigation of oxidation and reduction processes is cyclic voltammetry (CV) [1, 10]. It delivers information about thermodynamic and kinetic reaction parameters and shows if reactions are diffusion- or adsorption-controlled. Furthermore, it is frequently applied for the determination of reaction rate constants and mechanisms [2]. The method features the linear variation of electrode potential, going from an initial potential E_1 to a vertex potential E_2. Thereafter, the same potential range is consecutively scanned in the opposite direction, completing a scan cycle. In many cases, multiple cycles are performed as illustrated in **Figure 2.1.6**.

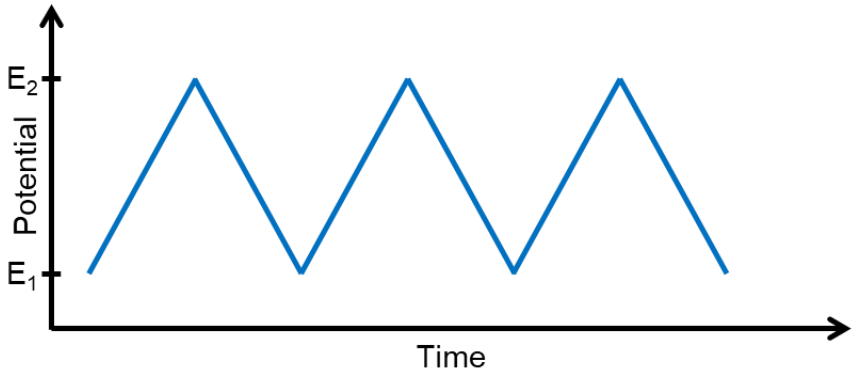

Figure 2.1.6: Working electrode potential over time in a cyclic voltammetry experiment consisting of three scan cycles. The potential is linearly varied between E_1 and E_2. Adapted from [4].

While cycling the potential, the resulting current is recorded. When electrochemical oxidation or reduction takes place within the investigated potential range, it is manifested as an increase or decrease of current. Negative and positive changes in current indicate reduction and

oxidation processes, respectively. In cyclic voltammograms (CVs), which display the measured current vs the applied potential, these processes are often visible as shown in **Figure 2.1.7A**. In this example, a reversible reaction with a one-electron transfer at a macroelectrode is demonstrated, with an oxidation taking place during the forward sweep from negative to positive potential, followed by a reduction peak during the backwards scan. The shape of the peaks can be explained by taking into account diffusion processes and electrode kinetics. In case of the forward scan, the initially low potential thermodynamically favors the reduced species, which is already present. Therefore, low and mostly capacitive currents are measured. As the potential is raised, the oxidized form becomes the more favored form, and the current starts to increase. The current peak indicates the point where all reduced species is consumed at the electrode surface and diffusion starts to be the limiting factor of the reaction, resulting to a continuous decrease in current according to the Cottrell equation **(9)** due to a growth of the diffusion layer [1]. The entire process is analogous for the reverse scan. In **Figure 2.1.7B**, the same reaction is shown, but conducted at an UME. Due to the spherical diffusion being dominant in this case, the steady state occurs sooner, and oxidation and reduction plateaus are exhibited instead of peaks. After a maximum current is reached during a potential scan, the current remains mostly stable as the diffusion layer thickness and thus the rate at which species is transported between electrode surface and bulk solution remains constant. In addition, capacitive currents are lower compared to macroelectrodes [1].

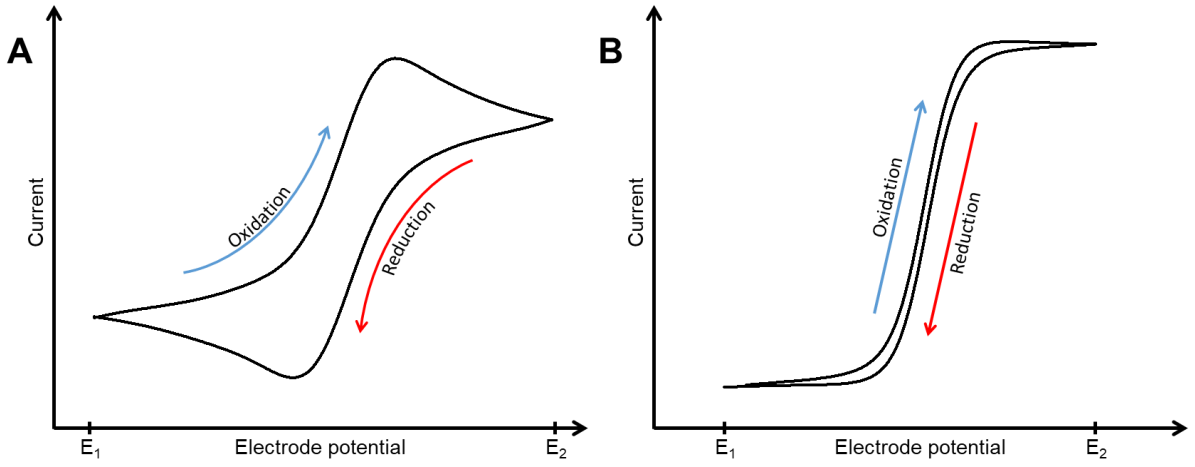

Figure 2.1.7: Cyclic voltammograms recorded at a macroelectrode (**A**) and an UME (**B**).

2.1.5. Forced convection in electrochemical experiments

Introducing forced convection in electrochemical measurements comes with multiple experimental benefits. Firstly, enhanced mass transport results in an increased conversion rate at electrodes, noticeable as generally higher currents. In addition, steady-state conditions are established which are useful for the analysis of homogeneous and heterogeneous kinetics

[10]. Forced convection can be realized by multiple methods. Using the principle of rotary motion either by rotating electrodes [6] or by stirring the electrolyte is possible [11]. Alternatively, employing a pump, working in a flow cell [12] or by directing a flow towards the surface of an electrode in a so-called wall-jet configuration were demonstrated to be feasible [13].

For all of the mentioned methods, the flux of species described by the Nernst-Planck equation **(5)** changes to the following [2]:

$$J(x) = -D\frac{\delta c(x)}{\delta x} + \upsilon c(x) \qquad \textbf{(13)}$$

Since the addition of excess supporting electrolyte is assumed, the migration term is neglected, while the diffusion and the convection term remain. To characterize the diffusion layer properties at the electrode surface, the change of flux over time described in equation **(14)** is of interest. In this case, one-dimensional diffusion and convection in x-direction are assumed [1].

$$\frac{\partial J(x)}{\partial t} = -D\frac{\partial^2 c(x)}{\partial x^2} + \upsilon\frac{\partial c(x)}{\partial x} \qquad \textbf{(14)}$$

When constant forced convection is applied, $\partial J(x)/\partial t = 0$, representing the earlier mentioned steady-state conditions. Consequently, a diffusion layer of constant thickness is established, resulting in a limiting current I_L measured at the electrode. This also called steady-state current can be brought into direct correlation with the diffusion layer thickness δ by solving equation **(14)**, yielding [6]:

$$I_L = \frac{nFADc_0}{\delta} \qquad \textbf{(15)}$$

The impact of forced convection on the concentration profile at the electrode surface is illustrated in **Figure 2.1.8**, where the difference between a growing diffusion layer in quiescent solution vs a diffusion layer of constant thickness due to elevated mass transfer is shown.

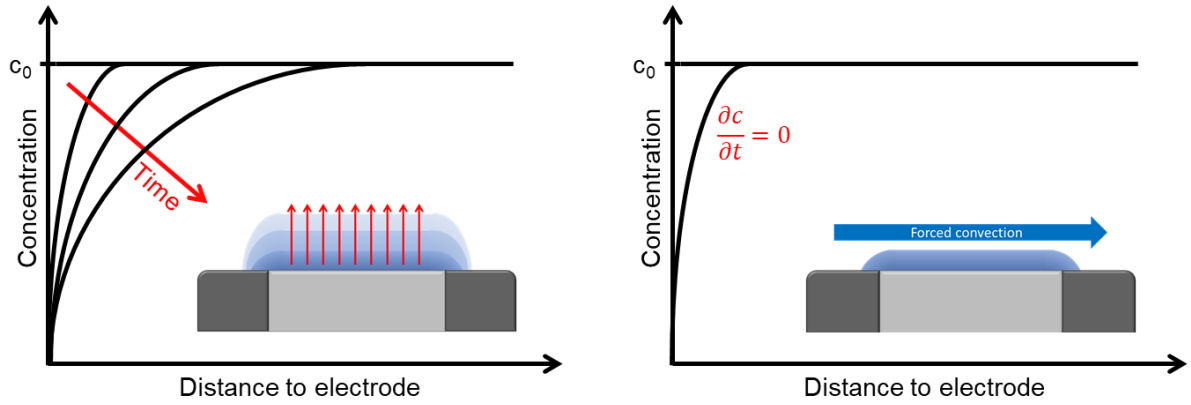

Figure 2.1.8: Development of the concentration profile and the correlating diffusion layer thickness at a macroelectrode during an electrochemical reaction under quiescent conditions (left) and when forced convection is introduced (right). Adapted from [6].

In case of UMEs, a constant diffusion layer can also be observed in quiescent solution as mainly time-independent spherical diffusion occurs. Nevertheless, they benefit from forced convection, as higher currents are recorded due to the increased mass transfer.

2.1.6. Thermoelectrochemistry and Hot-wire electrochemistry

In the field of modern thermoelectrochemistry, the temperature is treated as a further variable added to the classical variables of electrochemistry, which are considered to be potential, time and current [14]. Similar to forced convection, temperature can be used to alter the magnitude of motion within a solution. At increased temperatures, reduced friction between molecules results in a lower viscosity of the solvent and thus enhanced diffusion. The temperature dependence of diffusion can be described with the Stokes-Einstein relation, showing that the diffusion coefficient of a solution increases with temperature [14]:

$$D = \frac{k_B T}{6\pi\eta r} \qquad \textbf{(16)}$$

Herein, k_B represents the Boltzmann constant, η the dynamic viscosity and r the hydrodynamic radius of the diffusing species. Furthermore, when a temperature gradient is present, the so-called Soret diffusion occurs, resulting in molecules moving from hot to cold regions [14].

Apart from its influence on flux in the bulk solution, temperature impacts all processes during electrode reactions, including adsorption, desorption, charge transfer, species conversion, as well as transport of educts and products towards and away from the electrode surface. All these processes contribute to the reaction rate constant k as reflected by the Arrhenius equation [14]:

$$k = A \cdot \exp\left(-\frac{E_A}{RT}\right) \quad \textbf{(17)}$$

Herein, A represents a preexponential factor and E_A is the activation energy. As can be derived from this equation, increased temperatures result in elevated electrode kinetics due to a higher k.

Heating can be performed isothermally or non-isothermally, meaning that either the entire or only part of the cell is heated. The former however suffers from limitations such as slow temperature adjustments and the need for precautions to protect the reference electrode from temperature variations. Otherwise, a shift in reference potential will occur during experiments. Consequently, non-isothermal heating is usually preferred, and a popular method for achieving this was termed “hot-wire electrochemistry” [15]. In this technique, noble metal microwires, usually of gold or platinum with a diameter of 25 µm, are heated by an alternating current (AC) of a frequency typically higher than 100 kHz. Additionally, the heating AC can be superimposed by a direct current from a potentiostat. As a result, a temperature-adjustable microwire employable as working electrode is obtained. In terms of applications, this technique was employed e.g. for the analysis of various elements [16, 17], nucleic acid studies [18], and the oxidation of acetaminophen [19].

When an electrode is heated, its surface temperature changes over time as indicated in **Figure 2.1.9**. During the initial few seconds, a temperature peak is expressed after which a certain equilibrium temperature is established. With higher heat intensity, the peaks are sharper and temperatures above the boiling point of the aqueous electrolyte are reached for a short period. This occurs since the thermal convection that distributes the heat around the electrode is delayed due to the inertia of the solvent molecules [14]. Furthermore, no boiling occurs when the time of overheating remains short. Making use of this phenomenon, short temperature pulses were included in electrochemical experiments to enhance the electrochemical response [17, 20, 21].

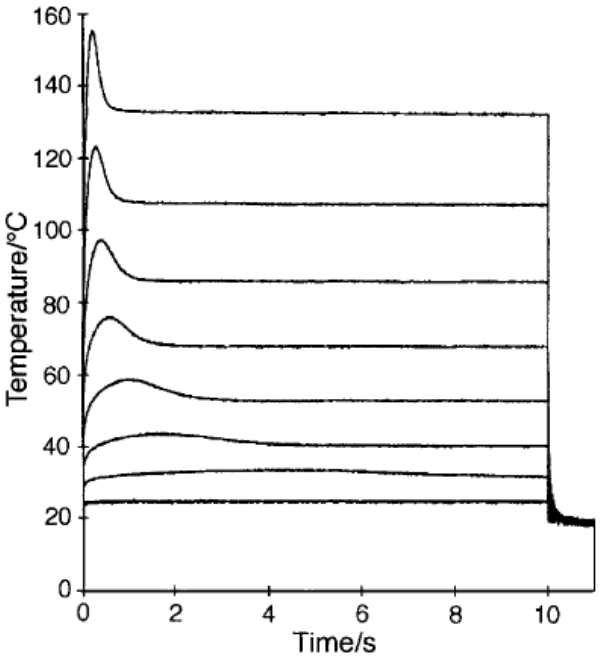

Figure 2.1.9: Surface temperature of a horizontally oriented wire electrode (Pt, 25 µm diameter) heated by constant power of different magnitudes. Reproduced from Ref. [15] with permission from The Royal Society of Chemistry.

2.2. Scanning electrochemical microscopy

Scanning electrochemical microscopy (SECM) is a tool for the analysis of surfaces and interfaces regarding their local electrochemical activity and conductivity. It was originally introduced by the groups of Bard [22] and Engstrom [23] and belongs to the group of scanning probe microscopy techniques. Methods in this field generally have in common that a probe is scanned across a surface of interest while gathering information about the surface with respect to probe position. In case of SECM, an UME is employed as probe, and in most of the measurement modes, a current recorded at the probe serves as measurement signal. In the upcoming chapters, an overview of the SECM features used in this thesis will be given, followed by a short chapter covering scanning ion conductance microscopy (SICM).

2.2.1. Instrumental setup

A schematic setup commonly used for SECM studies is shown in **Figure 2.2.1**.

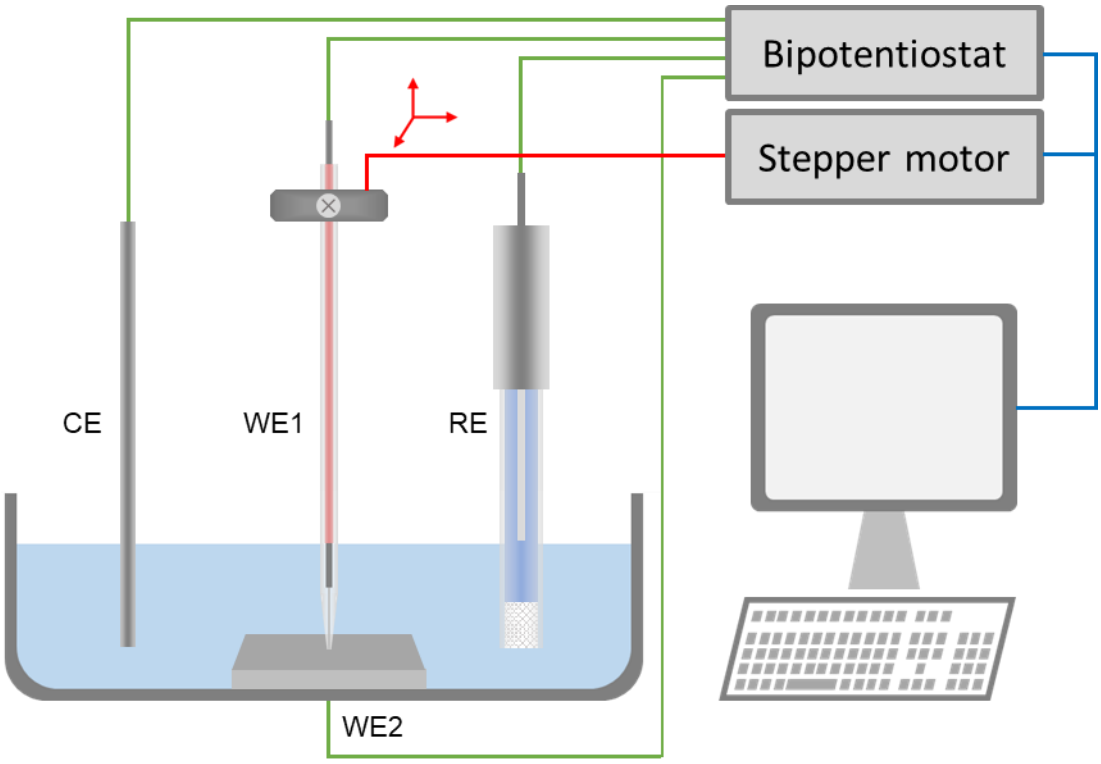

Figure 2.2.1: Components required for SECM. Experiments are carried out in a cell containing the sample, redox mediator solution, and electrodes (WE1, RE, CE). An UME is employed as WE1 and can be moved in all directions by a stepper motor. Optionally, a potential can be applied to the sample using the secondary working electrode (WE2) channel. Potentials are applied via a bipotentiostat.

Experiments are usually performed in an electrochemical cell containing the sample to be studied and a solution consisting of supporting electrolyte and a redox mediator. The latter is a redox active species that can be converted electrochemically in a reversible way. An UME is utilized as primary WE, at which the current from mediator conversion is measured. It is placed in a probe holder above the cell, which can be scanned across the sample surface via stepper motors. Furthermore, the cell contains a CE and RE for completion of the electrochemical setup. Dependent on the SECM operating mode, the substrate can be employed as a second WE [24].

2.2.2. Probe preparation and characterization

Typically, probes for SECM are disk-shaped UMEs with an electroactive diameter of less than 25 µm. A lower diameter thereby results in a higher image resolution. So far, probes with diameters down to the nanometer range have been fabricated [25]. Multiple protocols for probe fabrication were developed. A common practice to obtain probes in the micrometer range features the placement of a thin wire of electrode material inside a pulled glass capillary. The capillary tip is molten to seal the wire, followed by mechanical polishing to retrieve a flat disk

UME surrounded by glass [26]. **Figure 2.2.2** shows a detailed view of a probe fabricated by this method.

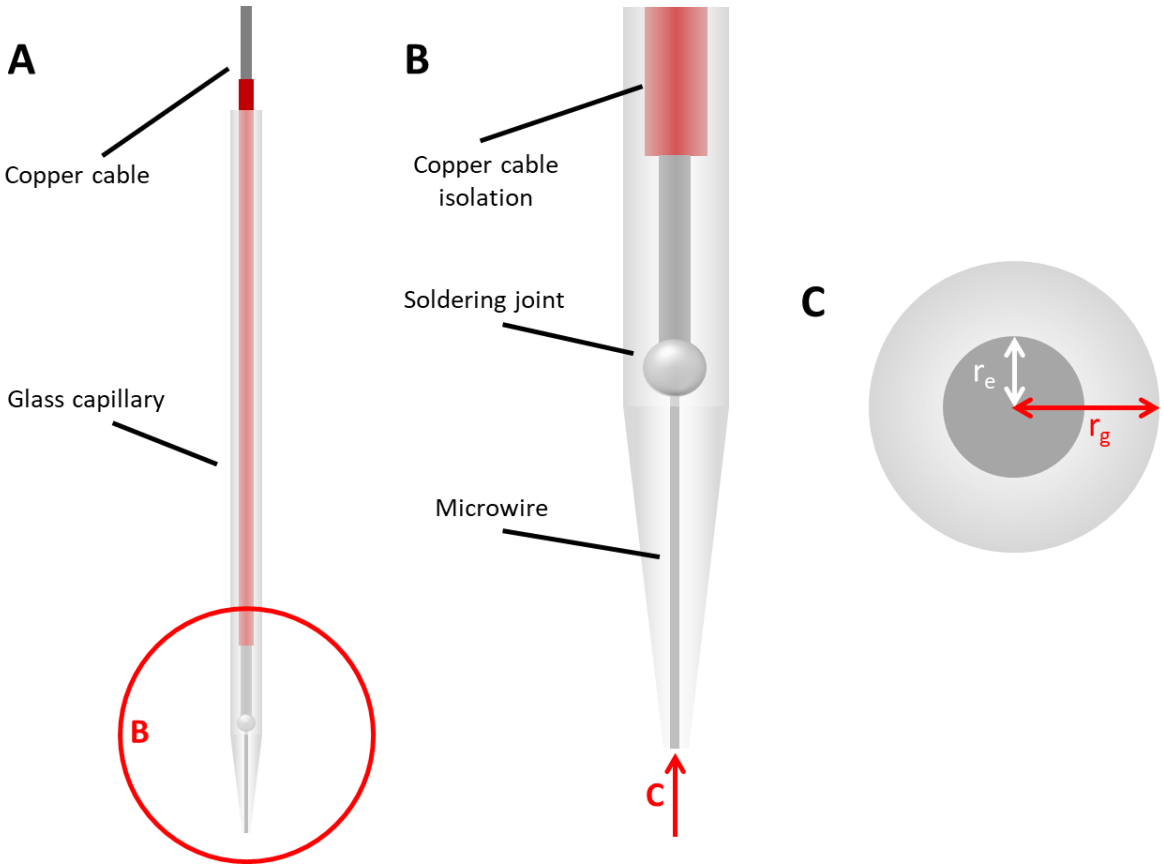

Figure 2.2.2: Schematic assembly of an UME probe used for SECM. **A:** View of the entire probe. **B:** Pulled end of the probe showing the microwire soldered to the supporting copper cable. **C:** Probe tip consisting of a microwire sealed in glass. r_e: Electrode radius. r_g: glass sheath radius.

Apart from electrode material and electroactive area, an important characteristic is the RG-value, which is defined as the ratio between the isolating sheath radius r_g and the electrode radius r_e [24]:

$$RG = \frac{r_g}{r_e} \tag{18}$$

This ratio is relevant since the thickness of insulation influences the diffusion process between bulk solution and electrode surface. When the insulation is thinner, the diffusion is slightly less hindered [24].

2.2.3. Measurement modes

Most SECM experiments are carried out in amperometric measurement modes, where a current originating from a reaction at the probe tip is measured. The most prominent one is the

feedback mode, in which the redox mediator is directly converted at the UME tip. In principle, when the probe is positioned in the bulk solution, a certain current is measured. When moving the tip closer to the substrate to be studied, the current increases or decreases dependent on whether the substrate is a conductor or an isolator, respectively. These two kinds of response are termed as positive and negative feedback and are illustrated in **Figure 2.2.3** [24].

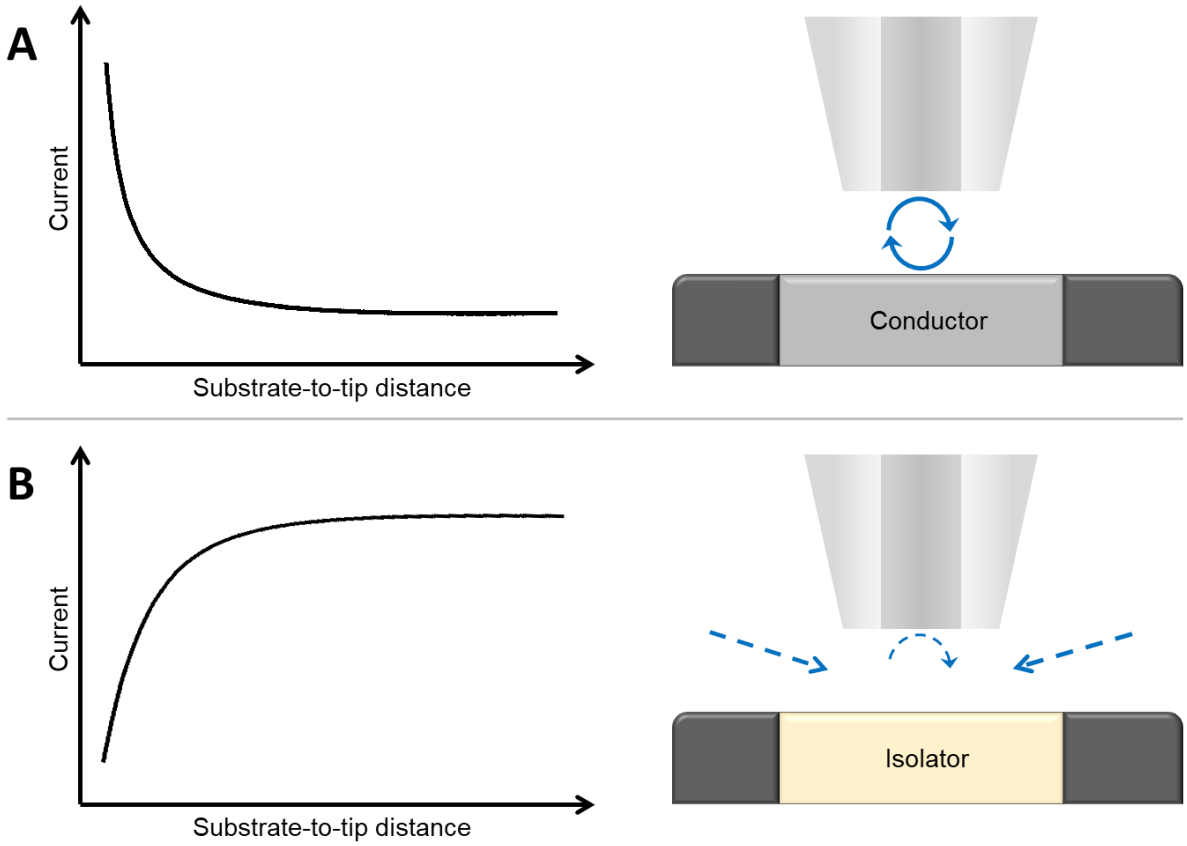

Figure 2.2.3: Positive (**A**) and negative (**B**) feedback response obtained while the probe approaches a conductor and an isolator, respectively. Additionally, the processes occurring at the tip when close to the surface are illustrated. Adapted from [24].

In **Figure 2.2.3A**, the positive feedback response is depicted. When the probe is far from the surface, the current corresponds to the amount of mediator diffusing towards the tip. As the tip gets close to the surface, a so-called feedback-loop is established, which describes the process of cycling the redox active species between its reduced and oxidized state. This is happening since the conductive surface can provide or take up electrons in order to revert the electrochemical process occurring at the probe tip. Therefore, as more convertible species is available at the tip when close to a conductor, an increased current is measured at small substrate-to-tip distances [22]. In case of approaching an isolator, the current measured at the probe decreases as indicated in **Figure 2.2.3B**. Since fresh mediator can only reach the tip via diffusion and the surface is hindering diffusion, a decreasing current is measured when the probe approaches the substrate [22].

The approach responses for both cases have been described theoretically. Simulations have yielded the following equations to describe the negative [27] and positive [28] feedback response, respectively.

$$\frac{i_T}{i_{T,\infty}} = \frac{\frac{2.08}{RG^{0.358}}\left(L - \frac{0.145}{RG}\right) + 1.585}{\frac{2.08}{RG^{0.358}}(L + 0.0023RG) + 1.57 + \frac{\ln RG}{L} + \frac{2}{\pi RG}\ln\left(1 + \frac{\pi RG}{2L}\right)} \quad \textbf{(19)}$$

$$\frac{i_T}{i_{T,\infty}} = \alpha(RG) + \frac{\pi}{4\beta(RG)\arctan(L)} + \left(1 - \alpha(RG) - \frac{1}{2\beta(RG)}\right)\frac{2}{\pi}\arctan(L) \quad \textbf{(20)}$$

The current response is given in normalized form as the ratio between measured current i_T and current in the bulk solution $i_{T,\infty}$. Furthermore, L represents the normalized distance given by the ratio of substrate-to-tip distance d and r_e [27].

$$L = \frac{d}{r_e} \quad \textbf{(21)}$$

In addition, $\alpha(RG)$ and $\beta(RG)$ are dimensionless extensions to equation **(20)** [28]:

$$\alpha(RG) = \ln 2 + \ln 2\left(1 - \frac{2}{\pi}\arccos\left(\frac{1}{RG}\right)\right) - \ln 2\left(1 - \left(\frac{2}{\pi}\arccos\left(\frac{1}{RG}\right)\right)^2\right) \quad \textbf{(22)}$$

$$\beta(RG) = 1 + 0.639\left(1 - \frac{2}{\pi}\arccos\left(\frac{1}{RG}\right)\right) - 0.186\left(1 - \left(\frac{2}{\pi}\arccos\left(\frac{1}{RG}\right)\right)^2\right) \quad \textbf{(23)}$$

These equations are especially useful for the characterization of UMEs. By performing probe approach curves (PACs), the RG value and thus the thickness of the isolating layer can be determined. The electrode area can be derived from the steady-state current given in equation **(12)**.

Another important amperometric SECM operation mode is the generation/collection (G/C) mode. It can be subdivided further in the substrate generation/tip collection (SG/TC) and the tip generation/substrate collection (TG/SC) mode. In case of the SG/TC mode, the method features the generation of an electroactive species at the substrate, which is subsequently collected at the probe tip [24]. Apart from electrochemical generation, collectable species can also be generated by an enzymatic reaction to investigate the local enzymatic activity [29]. In the TG/SC mode, the roles of probe and substrate are vice versa. Instead of generating species to be collected at the other electrode, both probe and substrate can have the same potential applied to compete for redox active species in the competition mode [24]. **Figure 2.2.4** illustrates the processes occurring these three modes. In general, these modes can be applied for the analysis of electrocatalysts.

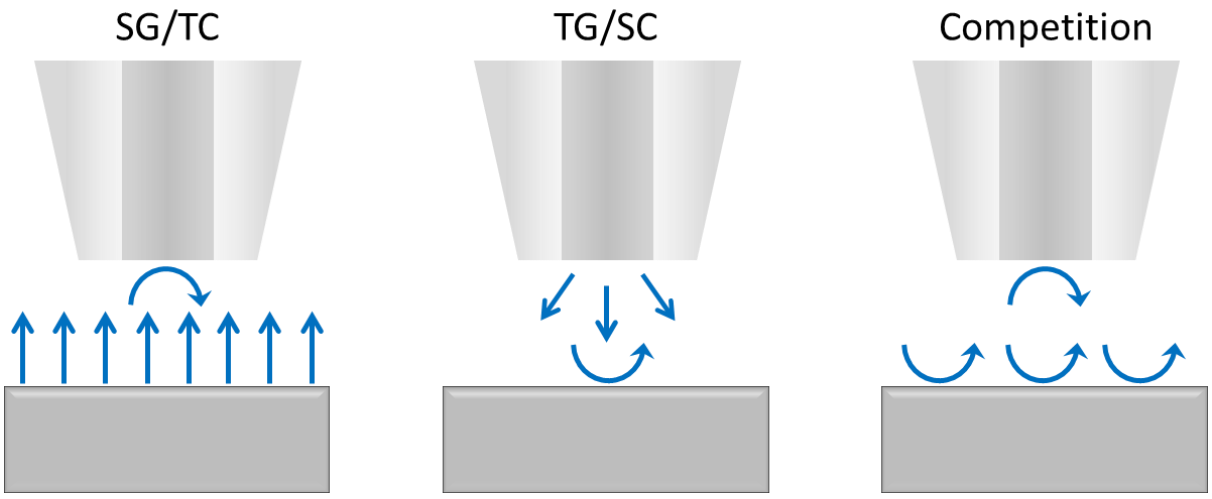

Figure 2.2.4: Illustration of the processes occurring at the probe and the substrate during SG/TC, TG/SC and competition mode. In the SG/TC mode, electroactive substance is generated at the substrate and converted at the probe. The opposite process occurs in the TG/SC mode. In the competition mode, both probe and substrate consume electroactive species contained in the electrolyte.

2.2.4. Forced convection in SECM

When operating the SECM in SG/TC or competition mode, a diffusion layer is usually growing at the substrate over time since it generally resembles a macroelectrode. As a result, a transient signal is measured at the probe when scanning across the substrate. To avoid this, the imaging process is started as soon as the diffusion layer growth is negligible. This can be problematic if images need to be recorded in quick succession. To overcome this limitation, forced convection can be used to establish diffusion layers of constant thickness as discussed in chapter 2.1.5. So far, forced convection was introduced into SECM either via stirring the solution [11] or by establishing a flow cell setup [12]. **Figure 2.2.5** shows the difference between successive SG/TC mode images recorded under quiescent conditions and while stirring the electrolyte [11].

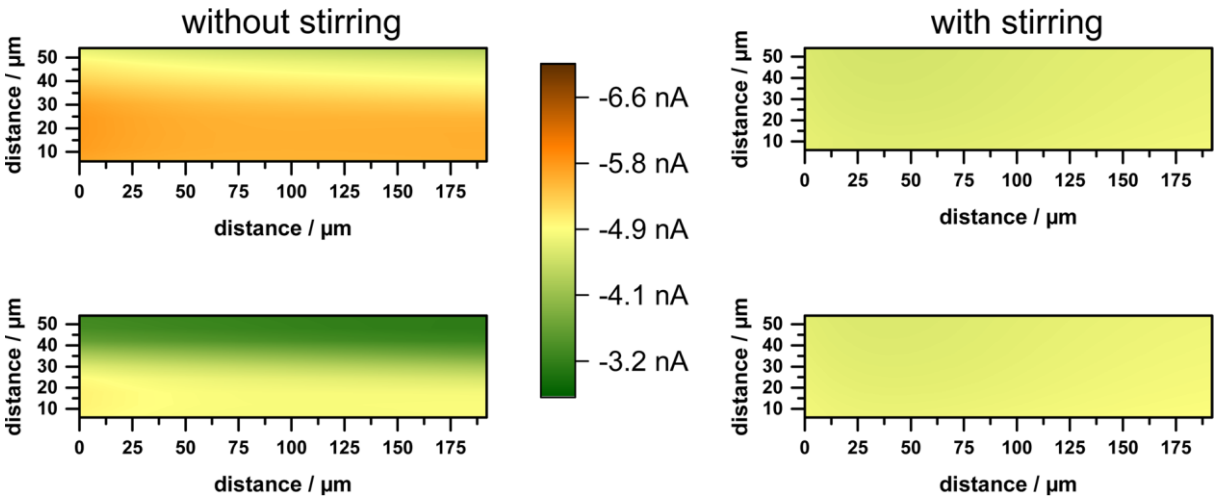

Figure 2.2.5: Successive SECM images of a 2 mm diameter Pt electrode recorded in SG/TC mode. Images were either recorded under stationary conditions (left) or while the electrolyte was stirred (right). In contrast to measurements in quiescent solution, stirring resulted in reproducible images and a constant signal. Reprinted with permission from [11]. Copyright (2017) American Chemical Society.

2.3. Scanning ion conductance microscopy

Scanning ion conductance microscopy, which is a scanning probe technique introduced by Hansma el al. [30], allows for the investigation of local topography without surface contact. The measurement principle is further illustrated in **Figure 2.3.1**. The general setup is very similar to SECM with the following main differences: Instead of an UME, the method involves the usage of a small, electrolyte-filled pipette as probe. In addition, since no electrochemical processes occur, quasi-reference electrodes (usually Ag/AgCl wires) are used. One electrode is placed inside the pipette while another one is positioned in the measurement cell. As the surface of interest is scanned, a potential is applied between the electrodes and the ion current flowing between the pipette interior and the surrounding bulk solution is monitored. When the probe is close to the substrate, the pipette aperture is blocked, resulting in a hindered flux of ions and thus a lower measured current [30].

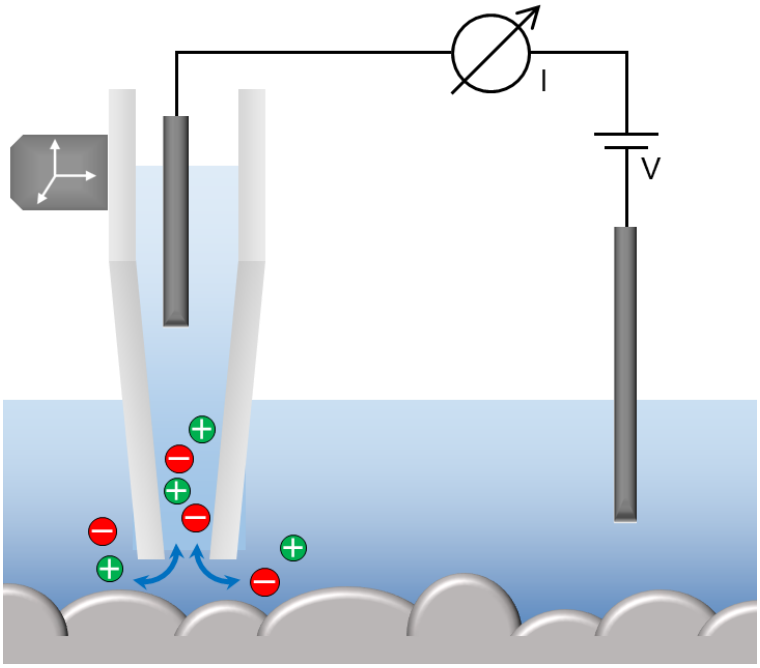

Figure 2.3.1: Measurement principle of SICM. A small pipette is used as probe, which is filled with electrolyte and a Ag/AgCl wire. Another Ag/AgCl wire is placed in the measurement cell. The ion current between both electrodes is measured during a scan. When the pipette is close to the surface, the resulting hindered ion migration leads to a current decrease.

Surfaces can be scanned in a variety of modes. As no contact between probe and substrate occurs during imaging, SICM is a popular technique for the analysis of fragile samples and is predominantly applied for the investigation of biological cell surfaces. Apart from morphological studies [31], ion flux across membranes can be assessed in order to locate and characterize ion channels [32]. Furthermore, pipets with diameters in the nanometer range have been used to pierce through cell membranes to study processes inside cells [33].

References

1. Bard AJ, Faulkner LR (2001) Electrochemical methods. Fundamentals and applications, 2nd ed. Wiley, Hoboken, NJ
2. Brett CMA, Oliveira Brett AM (2005) Electrochemistry. Principles, methods, and applications, 1. publ. 1993, reprinted 2005. Oxford science publications. Oxford Univ. Press, Oxford
3. Bockris JO, Devanathan MAV, Müller K, Butler JAV (1963) On the structure of charged interfaces. Proc. R. Soc. Lond. A 274(1356):55–79
4. Wang J (2006) Analytical electrochemistry, 3rd ed. Wiley-VCH, Hoboken, N.J
5. Endo M, Takeda T, Kim Y, Koshiba K, Ishii K (2001) High Power Electric Double Layer Capacitor (EDLC's); from Operating Principle to Pore Size Control in Advanced Activated Carbons. Carbon letters 1
6. Zoski CG (2007) Handbook of electrochemistry. Elsevier, Amsterdam
7. Montenegro MI, Queirós MA, Daschbach JL (1991) Microelectrodes. Theory and Applications. Springer Netherlands, Dordrecht
8. Aoki K, Osteryoung J (1984) Formulation of the diffusion-controlled current at very small stationary disk electrodes. J. Electroanal. Chem. Interf. Electrochem. 160(1):335–339
9. Polcari D, Dauphin-Ducharme P, Mauzeroll J (2016) Scanning Electrochemical Microscopy: A Comprehensive Review of Experimental Parameters from 1989 to 2015. Chem. Rev. 116(22):13234–13278
10. Compton RG, Laborda E, Ward KR (2014) Understanding voltammetry. Simulation of electrode processes. Imperial College Press, London
11. Iffelsberger C, Vatsyayan P, Matysik F-M (2017) Scanning Electrochemical Microscopy with Forced Convection Introduced by High-Precision Stirring. Anal. Chem. 89(3):1658–1664
12. Raith T, Wert S, Iffelsberger C, Matysik F-M (2018) Development and characterization of electrochemical flow cells for hydrodynamic scanning electrochemical microscopy. Monatsh. Chem. 149(9):1671–1677
13. Karyakin AA, Karyakina EE, Lo Gorton (1998) The electrocatalytic activity of Prussian blue in hydrogen peroxide reduction studied using a wall-jet electrode with continuous flow. J. Electroanal. Chem. 456(1-2):97–104
14. Gründler P (2015) In-situ thermoelectrochemistry. Working with heated electrodes. Monographs in electrochemistry. Springer, Berlin

15. Gründler P, Kirbs A, Zerihun T (1996) Hot-wire electrodes: voltammetry above the boiling point. Analyst 121(12):1805–1810

16. Gründler P, Flechsig G-U (1998) Deposition and stripping at heated microelectrodes. Arsenic(V) at a gold electrode. Electrochim. Acta 43(23):3451–3458

17. Gründler P, Flechsig G-U (2006) Principles and Analytical Applications of Heated Electrodes. Microchim. Acta 154(3):175–189

18. Peter J, Reske T, Flechsig G-U (2007) Comparison of DNA Hybridization at Rotating and Heated Gold Disk Electrodes. Electroanalysis 19(13):1356–1361

19. Mathivanan J, Chang Z, Galagedera SKK, Flechsig G-U (2018) Thermoelectrochemistry of Paracetamol - Studied at Directly Heated Micro-wire and Rotating Disk Electrodes. Electroanalysis 30(7):1479–1486

20. Flechsig G-U, Walter A (2012) Electrically Heated Electrodes: Practical Aspects and New Developments. Electroanalysis 24(1):23–31

21. Gründler P, Kirbs A (1999) The Technology of Hot-Wire Electrochemistry. Electroanalysis 11(4):223–228

22. Bard AJ, Fan FRF, Kwak J, Lev O (1989) Scanning electrochemical microscopy. Introduction and principles. Anal. Chem. 61(2):132–138

23. Engstrom RC, Pharr CM (1989) Scanning electrochemical microscopy. Anal. Chem. 61(19):1099A–1104A

24. Bard AJ, Mirkin MV (2012) Scanning electrochemical microscopy, 2nd ed. CRC Press, Boca Raton, Fla

25. Kai T, Zoski CG, Bard AJ (2018) Scanning electrochemical microscopy at the nanometer level. Chem. Commun. (Cambridge, England) 54(16):1934–1947

26. Zoski CG (2002) Ultramicroelectrodes: Design, Fabrication, and Characterization. Electroanalysis 14(15-16):1041–1051

27. Cornut R, Lefrou C (2007) A unified new analytical approximation for negative feedback currents with a microdisk SECM tip. J. Electroanal. Chem. 608(1):59–66

28. Lefrou C (2006) A unified new analytical approximation for positive feedback currents with a microdisk SECM tip. J. Electroanal. Chem. 592(1):103–112

29. Raith T, Kröninger A, Mickert MJ, Gorris HH, Matysik F-M (2020) Enhanced resolution of generator-collector studies of enzymatic structures by means of hydrodynamic scanning electrochemical microscopy. Talanta 214:120844

30. Hansma PK, Drake B, Marti O, Gould SA, Prater CB (1989) The scanning ion-conductance microscope. Science (New York, N.Y.) 243(4891):641–643

31. Gorelik J, Zhang Y, Shevchuk AI, Frolenkov GI, Sánchez D, Lab MJ, Vodyanoy I, Edwards CR, Klenerman D, Korchev YE (2004) The use of scanning ion conductance microscopy to image A6 cells. Mol. Cell. Endocrinol. 217(1):101–108

32. Torres-Pérez JV, Naeem H, Thompson CL, Knight MM, Novak P (2020) Nanoscale Mapping Reveals Functional Differences in Ion Channels Populating the Membrane of Primary Cilia. Cell. Physiol. Biochem. 54(1):15–26

33. Pan R, Hu K, Jia R, Rotenberg SA, Jiang D, Mirkin MV (2020) Resistive-Pulse Sensing Inside Single Living Cells. J. Am. Chem. Soc. 142(12):5778–5784

3. Experimental

3.1. Instrumentation and chemicals

In this section, the commercially available instruments, software, materials, and chemicals, which were used during this work, are listed.

Instruments:

Device	Provider
3D printer Prusa i3 MK3	Prusa Research, Prague, Czech Republic
ASTeX 5010	Seki Technotron, Tokyo, Japan
Confocal laser scanning microscope	Olympus, Tokyo, Japan
Digital microscope VHX-7000	Keyence, Osaka, Japan
Digital USB microscope	dnt DigiMicro Profi, Dietzenbach, Germany
Electrical BL-DC-motor (2250S012BX4 CSD 3830)	Dr. Fritz Faulhaber GmbH & Co., KG, Schönaich, Germany
Flashlight Fenix LD02	Fenix Lighting LLC, Littleton, Colorado, USA
Gas chromatograph HP 5890 Series II	Hewlett Packard, Palo Alto, California, USA
Hot glue gun (Pattex)	Henkel AG & Co. KGaA, Düsseldorf, Germany
HPLC pump 6400 884	Knauer GmbH, Berlin, Germany
Milli-Q Advantage A10 system	Merck Millipore, Merck KGaA, Darmstadt, Germany
SECM 920C	CH Instruments, Austin, Texas, USA
SECM with bipotentiostat (Autolab PGSTAT302N)	Sensolytics GmbH, Bochum, Germany Metrohm, Herisau, Switzerland
SEM JSM-6400F	Jeol Ltd., Akishima, Japan
SEM MIRA 3 with EDS XFlash 5010	TESCAN, Brno, Czech Republic Bruker, Billerica, Massachusetts, Vereinigte Staaten
Soldering station	WE CP-20, Weller, Wetzlar, Germany
Syringe pump	New Era Pump Systems Inc., East Farmingdale, New York, USA

Wide stand microscope x100	PEAK, Bornheim-Roisdorf, Germany

Software:

Software	Provider
CHI920C	CH Instruments, Austin, Texas, USA
COMSOL Multiphysics 5.2	COMSOL AB, Stockholm, Sweden
Microsoft Office 365	Microsoft, Redmond, Washington, USA
NOVA 2.1	Metrohm AG, Herisau, Switzerland
Origin 2019-2021	OriginLab, Northampton, Massachusetts, USA
Slic3r Prusa	Prusa Research, Prague, Czech Republic

Materials:

Material	Provider
Abrasive paper (80 and 100 grit size)	-
Ag/AgCl/3M KCl Reference electrode	CH Instruments, Austin, Texas, USA
Bladder syringe (100 mL)	BD Corp., Franklin Lakes, New Jersey, Vereinigte Staaten
Copper tube (ID: 1.1 mm,OD: 2.0 mm)	Albion Alloys, Bournemouth, United Kingdom
Copper wire (ID: 0.5 mm; OD: 1.1 mm)	Pollin Electronic GmbH, Pförring, Germany
Diamond lapping sheets (0.1, 0.3, 0.5, 1, 3, 5, 9, 30 micron)	Precision Surfaces International, Houston, Texas, USA
Epoxydharz L (Epoxy resin)	R&G Faserverbundstoffe GmbH, Waidenbuch, Germany
Emitters for electrospray ionization	New Objective, Woburn, Massachusetts
Glassy carbon plate	Sigradur G, Hochtemperatur-Werkstoff GmbH, Germany
GlucoSmart® Swing (Screen-printed electro-chemical sensor)	MSP bodmann GmbH, Bobingen, Germany

Hot glue sticks	Pattex, Henkel AG & Co. KGaA, Düsseldorf, Germany
Microscope slides	servoprax GmbH, Wesel, Germany
Peltier elements	KIMILAR, TEC1-12706
Poly lactic acid filament (Galaxy Silver)	Prusa Research, Prague, Czech Republic
Pt disk UME (10 µm diameter, RG > 10)	Sensolytics, Bochum, Germany
Pt wires (1 mm, 25 µm and 12.5 µm diameter)	Goodfellow, Cambridge, Great Britain
Silver conductive paint	VS Electronic, Aschaffenburg, Germany
Silver Epoxy 8331	MG Chemicals, Ontario, Canada
Soda lime glass capillaries (ID = 1.1 mm; OD = 1.8 mm)	Glaswerke Ilmenau, Ilmenau, Germany
SYLGARD™ 184 (Silicone elastomer kit)	Dow Inc., Midland, Michigan, USA
UHU plus endfest 300 (Epoxy resin)	UHU GmbH & Co. KG, Bühl, Germany
UHU Max Repair Extreme (Adhesive)	UHU GmbH & Co. KG, Bühl, Germany

Chemicals:

Chemical	**Provider**
Ammonium tetrathiomolybdate (NH_4MoS_4)	99.97%, Sigma-Aldrich, St. Louis, Missouri, USA
Disodium hydrogen phosphate dodecahydrate	Merck KGaA, Darmstadt, Germany
Ethanol (analytical grade)	Merck KGaA, Darmstadt, Germany
Ferrocenemethanol (FcMeOH)	99%, ABCR, Karlsruhe, Germany
Glucose monohydrate	Merck KGaA, Darmstadt, Germany
Glucose oxidase (GOx)	Merck KGaA, Darmstadt, Germany
Hexaaminеruthenium(III) chloride ($Ru(NH_3)_6Cl_3$)	ABCR, Karlsruhe, Germany
Potassium chloride (KCl)	Analytical grade, Merck KGaA, Darmstadt, Germany
Potassium ferricyanide ($K_3(Fe(CN)_6$)	Merck KGaA, Darmstadt, Germany

Potassium ferrocyanide ($K_4(Fe(CN)_6$)	Merck KGaA, Darmstadt, Germany
Potassium nitrate (KNO_3)	Merck KGaA, Darmstadt, Germany
Disodium hydrogen phosphate dodecahydrate	Merck KGaA, Darmstadt, Germany
Sodium dihydrogen phosphate monohydrate	Merck KGaA, Darmstadt, Germany
SU8-5 photoresist	Microchem Corp., Westborough, United States
Sulfuric acid (H_2SO_4) ROTIPURAN®Supra 95%	Carl Roth GmbH + Co. KG, Karlsruhe, Germany

3.2. Preparation procedures

3.2.1. Solutions

All solutions were prepared using Milli-Q water. Experiments involving GOx were carried out with solutions containing phosphate buffer (pH 7).

Mediators

For most electrochemical experiments, an aqueous mediator solution of 1.5 mM FcMeOH and 0.2 M KNO_3 was used. It was prepared with degassed water. Degassing was achieved by stirring water for 30 min at 60 °C while bubbling it with nitrogen. Dissolving of FcMeOH was supported by ultrasonication for 30 min at 50 °C. Before usage, the solution was kept at room temperature for 24 h.

For thermoelectrochemical studies, an equimolar solution of 5/5 mM $K_3/K_4(Fe(CN)_6$ in 1 M KCl was used as mediator. When using hydrogen as mediator species, 0.5 or 1.0 M H_2SO_4 was utilized. Glucose solutions of various concentrations were used for the generation of H_2O_2 in GOx activity studies. Other measurements were performed with 1.5 mM $Ru(NH_3)_6Cl_3$ in 0.2 M KCl or 10 mM $K_3(Fe(CN)_6$ in 0.1 M KCl. The respective usages of the mediator solutions are given in each subsection of the results and discussion part.

3.2.2. Ultramicroelectrodes

The procedure for UME fabrication described herein is based on literature protocols [1, 2]. A scheme illustrating the UME fabrication steps is given in **Figure 3.2.1**. Initially, a Pt microwire (1.5 cm length, 12.5 or 25 µm diameter) was soldered to a copper wire which had its isolation removed at both ends, providing a means for establishing electrical contact for the final

electrode. This assembly was inserted into a pulled soda lime glass capillary, making sure that the Pt wire exceeds the narrowed end of the capillary. The glass served two purposes: It provided mechanical stability of the probe to fit properly into the SECM probe holder, and it was used for sealing the Pt wire. The latter was achieved by melting the capillary tip with a gas torch. Polishing with diamond lapping sheets removed the excess wire and resulted in a flat probe tip. During the process, the lapping sheet particle size was continuously decreased from 3.0 to 0.1 micron yielding a smooth electrode surface. The electrodes were characterized by optical microscopy and CV with regards to their dimensions and functionality.

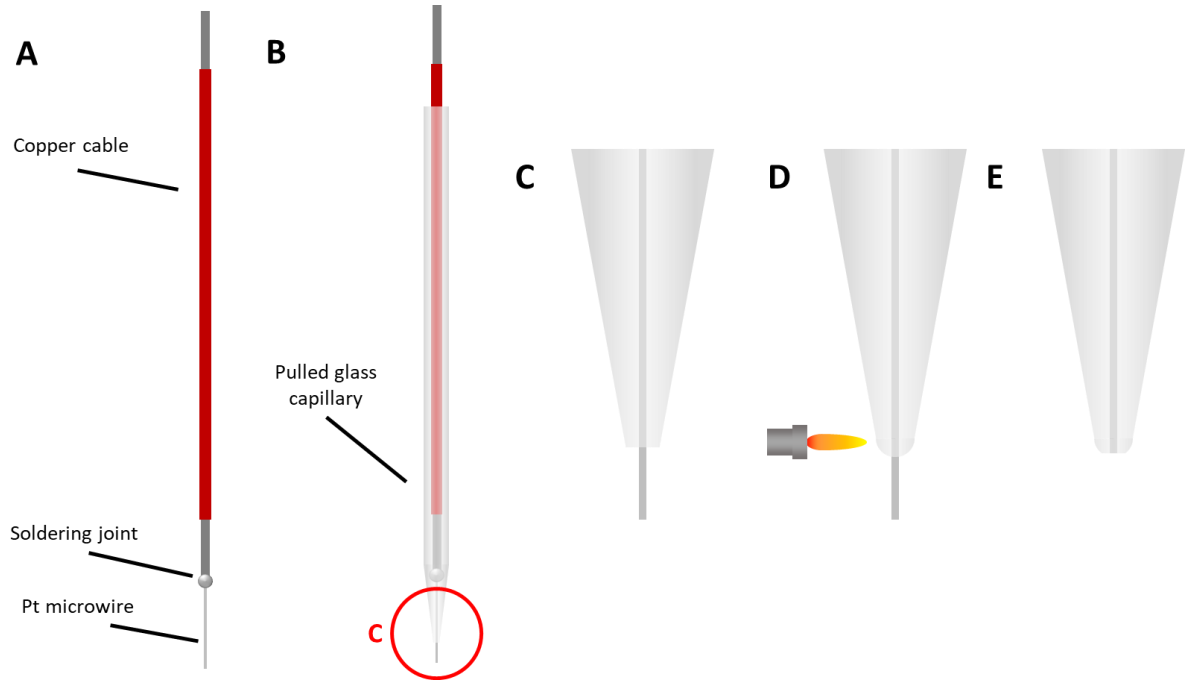

Figure 3.2.1: Fabrication steps for the preparation of SECM probes. **A:** A Pt wire is soldered to a supporting copper wire with removed isolation at both ends. **B:** The assembly is inserted into a pulled soda lime glass capillary so that the Pt wire exceeds the tapered end of the capillary. A closer view of the tip is given in **C**. **D:** Sealing of the Pt wire by melting the glass at the tip using a flame torch. **E:** A flat UME surface is revealed after polishing the tip with diamond lapping sheets.

3.2.3. Probes for combined SECM/SICM

The base material for SECM/SICM probes were commercially available emitters for electrospray ionization (ESI). They consisted of a quartz glass capillary with a tapered end on one side. The capillary came coated with a thin layer of Pt metal, which served as the electrode material for performing SECM. Due to its shape, the pulled capillary could be used as the pipette required for SICM. In order to obtain a functional SECM/SICM probe, modifications to the ESI emitters were applied as illustrated in **Figure 3.2.2**.

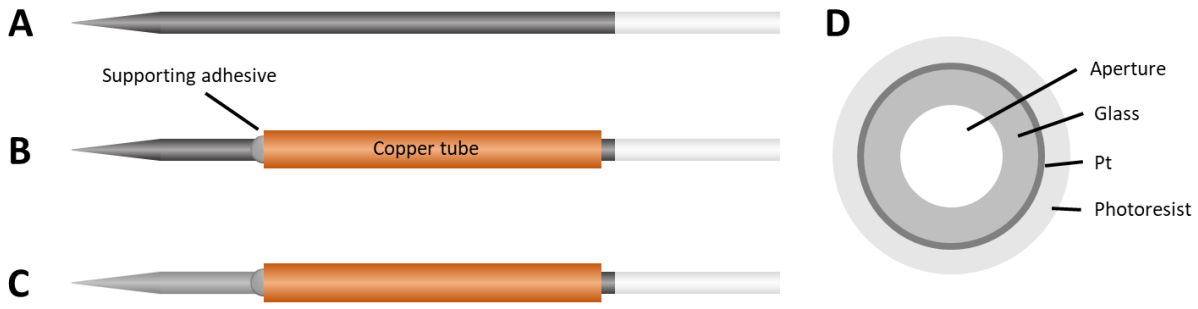

Figure 3.2.2: Modifications to the ESI emitters (**A**) required for obtaining SECM/SICM probes. **B:** The emitters were inserted into a copper tube using conductive paint and adhesive, providing a means for electrical contact and mechanical stabilization. **C:** The area between tip and copper tube was isolated via dip-coating with photoresist, resulting in a ring UME around the tip aperture (**D**).

First, the rear part of the Pt-coated area of the capillary was covered with conductive paint. The emitter was then inserted in a piece of copper tube of 3 cm length, which was positioned where the conductive paint was applied. It was fixed by a small droplet of adhesive. After drying for 2 h, a 10:1 (v:v) mixture of SU8-5 photoresist and ethanol was applied to the capillary tip by dipping the capillary into the mixture while a nitrogen flow was led through the tip to prevent clogging. For hardening of the photoresist, the capillary was placed in a convection oven at 95 °C for 5 min, exposed to UV light (365 nm) for 30 s, and again heated in the oven at 95 °C for 5 min. The coating process was evaluated via optical imaging and CV. Electrode dimensions were estimated by referring to literature values [3, 4]. In case of insufficient coating, more layers of photoresist were applied until a ring electrode was obtained. Another option was to carefully polish the tip with lapping sheets, which also resulted in larger tip diameters. To enable SICM imaging, the capillary was filled with 0.1 M KCl and a 0.3 mm diameter Ag/AgCl wire was inserted.

3.2.4. Hot-wire substrates

The procedure for preparation of hot-wire substrate to be used in conjunction with SECM is illustrated in **Figure 3.2.3**. To provide a flat metal surface, a 3 cm piece of Pt wire (25 µm diameter) was placed between glass slides and polymethylmethacrylate (PMMA) slides, and force was carefully applied on top using a hammer. Hitting the assembly ten times resulted in a flattened wire of about 70 µm width. As base of the substrate, a 2×4 cm piece of a microscope glass slide was used. It was coated with a thin layer of epoxy resin and the flattened wire was placed on top while the resin was still wet. In addition, two 0.5×1 cm pieces were positioned on top of the wire as shown in **Figure 3.2.3D** for additional fixation. Placing the substrate in a convection oven at 65 °C for 1 h led to hardening of the epoxy. Eventually, copper cables were soldered to both ends of the Pt wire, providing a means for electrical contact, and the soldering joints were sealed by applying hot glue.

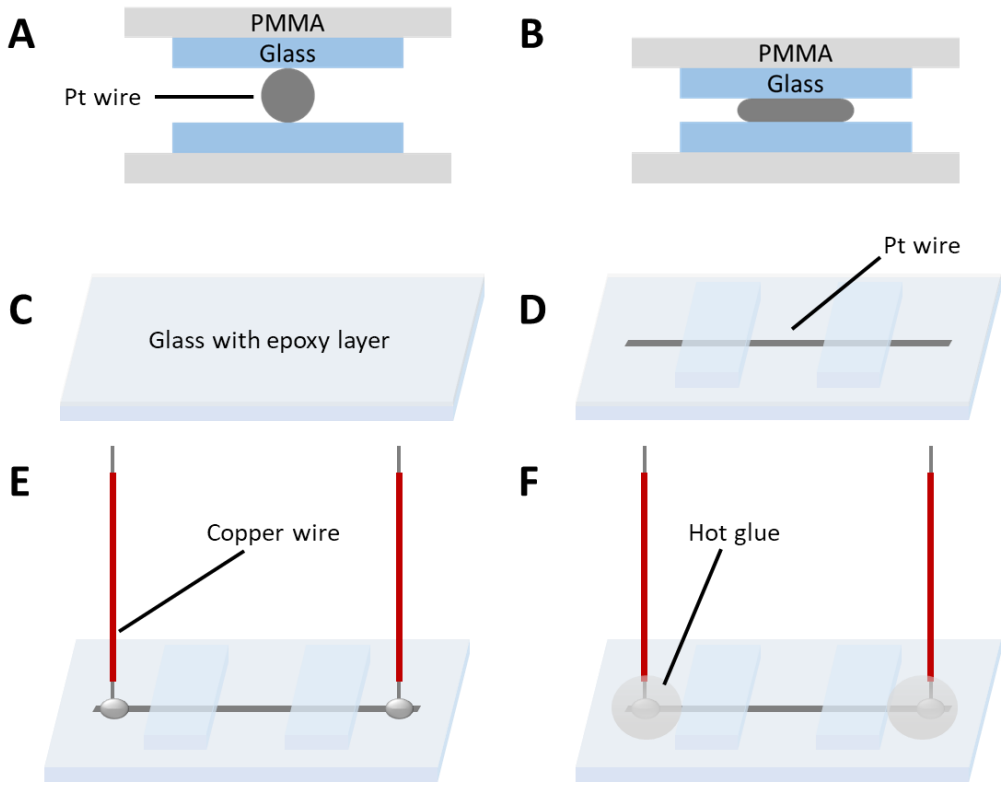

Figure 3.2.3: Fabrication steps for hot-wire SECM substrates. A Pt microwire was placed between glass and PMMA slides (**A**). Applying force on top of the assembly resulted in flattening of the wire (**B**). After application of a thin layer of epoxy resin on a glass substrate (**C**), the flattened wire was placed on top (**D**). Its position was fixed with two additional pieces of glass. Copper wires were soldered to both ends of the Pt wire for electrical contact (**E**). The soldering joints were isolated using hot glue (**F**).

3.3. SECM setup

The SECM was placed on a damped plate to minimize the impact of vibrations. To avoid electrical disturbances, it was surrounded by a faradaic cage, where it was isolated from all other electrical devices that were required for operation.

At the beginning of each experimental session, the quality of the UME was checked by performing a CV in mediator solution. If necessary, the UME surface was renewed by polishing with 0.1 micron lapping sheets.

Prior to SECM imaging, the substrate to be investigated was placed in an electrochemical cell which was fixed on a tilt-adjustable plate. The tilt of the substrate was either determined using a spirit level or by performing PACs of identical parameters at three different spots of the substrate of the same conductivity. Starting the PACs from a fixed global height, the different distances travelled for each location indicated the tilt magnitude. Adjusting the tilt was possible via three different micrometer screws included in the plate. Imaging was performed when the height difference was less than 1 µm mm^{-1}.

Apart from SECM imaging, the device was also used for classical electrochemical experiments such as CV, chronoamperometry or monitoring of the open circuit potential (OCP).

References

1. Zoski CG (2002) Ultramicroelectrodes: Design, Fabrication, and Characterization. Electroanalysis 14(15-16):1041–1051
2. Lee C, Miller CJ, Bard AJ (1991) Scanning electrochemical microscopy: preparation of submicrometer electrodes. Anal. Chem. 63(1):78–83
3. Cornut R, Mayoral M, Fabre D, Mauzeroll J (2010) Scanning Electrochemical Microscopy Approach Curves for Ring Microelectrodes in Pure Negative and Positive Feedback Mode. J. Electrochem. Soc. 157(7):F77
4. Lee Y, Amemiya S, Bard AJ (2001) Scanning electrochemical microscopy. 41. Theory and characterization of ring electrodes. Anal. Chem. 73(10):2261–2267

4. Results and discussion

4.1. A cost-efficient approach for simultaneous scanning electrochemical microscopy and scanning ion conductance microscopy

Stefan Wert, Simona Baluchová, Karolina Schwarzová-Pecková, Silvia Sedláková, Andrew Taylor and Frank-Michael Matysik

Monatshefte für Chemie - Chemical Monthly 151 (2020): 1249.

This chapter was published in the journal above and changed for reasons of uniformity. The changes herein consist of minor corrections and formatting.

Abstract

A novel and cost-efficient probe fabrication method yielding probes for performing simultaneous scanning electrochemical microscopy (SECM) and scanning ion conductance microscopy (SICM) is presented. Coupling both techniques allows distinguishing topographical and electrochemical activity information obtained by SECM. Probes were prepared by deposition of photoresist onto platinum-coated, pulled fused silica capillaries, which resulted in a pipette probe with an integrated ring ultramicroelectrode. The fabricated probes were characterized by means of cyclic voltammetry and scanning electron microscopy. The applicability of probes was demonstrated by measuring and distinguishing topography and electrochemical activity of a model substrate. In addition, porous boron-doped diamond samples were investigated via simultaneously performed SECM and SICM.

4.1.1. Introduction

Scanning electrochemical microscopy (SECM) is a powerful technique for the investigation of electrochemical and topographical properties of surfaces [1]. It belongs to the family of scanning probe techniques and features small electrodes as probes with electroactive diameters of 25 µm or less, which are termed ultramicroelectrodes (UMEs). Measurements are usually performed in a solution containing a reversible redox-active species, the so-called redox mediator. In the amperometric mode of SECM, a constant potential is applied to the UME, leading to the conversion of the mediator associated with a faradaic current that can be recorded. As the probe is scanned over the surface of a substrate in close proximity, the current changes with respect to the surface properties. However, if the substrate of interest exhibits

inhomogeneous topography and electrochemical activity, distinguishing between both types of information becomes challenging. In addition, maintaining a constant probe-to-substrate distance is difficult to guarantee in case of substrates with very inhomogeneous surface topography. To overcome these issues, SECM can be coupled with other techniques such as atomic force microscopy [2, 3]. However, in this approach, contact between the probe and the sample is typically established, which can damage fragile substrates and the probe itself. As a non-contact technique for acquiring topographical information and probe distance control, scanning ion conductance microscopy (SICM) can be utilized [4]. For this technique, a small micropipette is employed as a probe. As it is filled with supporting electrolyte and has a quasi-reference electrode placed within the interior of the pipette, a potential can be applied between the inner electrode and another quasi-reference electrode located in the bulk solution of the measurement cell. This results in an ionic current flowing between the pipette interior and the surrounding solution. Moving the pipette close to the surface leads to hindered ion migration at the pipette orifice, which is manifested by increased resistance and thus, lower current.

Performing SECM and SICM measurements simultaneously enables distinguishable acquisition of topographical and electrochemical activity information on surfaces. For the hyphenation of both techniques, probes with an integrated UME for SECM and a channel with micro- or nanometer size for SICM are required. To date, various approaches for the fabrication of such probes exist. Initial approaches were carried out by Comstock et al. [5] by depositing gold on one side of a nanopipette followed by isolation with Al_2O_3, both applied via atomic layer deposition. Another method features sputtering to create a noble metal surface and isolating the outer surface with electrophoretic paint [6]. Popular means for the fabrication of the UME part of probes feature pyrolysation of butane gas [7–9] or parylene C [10] to create carbon electrodes. The latter has also been used as an insulating material [10, 11]. Alternatively, pulled theta (dual barrel) capillaries were employed as housing of the probe and one barrel was filled with pyrolytic carbon as mentioned above, yielding a carbon barrel for SECM and an empty barrel for SICM. The latter was filled with electrolyte and a Ag/AgCl wire prior to measurements. In all dual-probe fabrication techniques mentioned before, focused ion beam milling is usually utilized to expose the electrode surface. These probes have recently been applied to the investigation of hydrogen peroxide generation at gold nanoparticles [12] and the surface characterization of different cells [9, 13]. Single-barrel nanopipette probes with electrode material deposited around the orifice have been realized with the methods mentioned above [5, 6, 11] and the characterization of such ring microelectrodes has been reported as well [14–17].

Boron-doped diamond (BDD) is a material exhibiting high chemical stability, inertness, and a wide potential window; therefore, being considered a potent electrode material [18, 19]. Porous BDD provides higher surface area, which results in, e.g., higher sensitivity and

selectivity [20, 21]. Non-porous, planar, BDD samples have been investigated via SECM and a non-uniform distribution of electrochemical activity was found [22, 23]. Therefore, in addition to an inhomogeneous surface, variances in the electrochemical activity of porous BDD are expected.

Since existing SECM–SICM dual-probe fabrication methods require sophisticated equipment, we aimed to develop a novel and cost-efficient approach for the preparation of such probes. The fabricated probes were characterized by scanning electron microscopy (SEM) and cyclic voltammetry (CV), revealing information about their size and functionality. The response in SECM and SICM probe approach curves (PACs) towards gold and glass surfaces was tested as well. Eventually, separate images showing the electrochemical activity and morphology of a model substrate and a porous BDD sample were recorded.

4.1.2. Results and discussion

The quality of the coating of the fabricated ring UME pipette probes was investigated by means of CV. **Figure 4.1.1a** shows a CV recorded with a probe being coated six times with a photoresist solution according to the procedure described in the experimental section. Subsequent polishing yielded a probe with a ring diameter of 25 µm. **Figure 4.1.1b** depicts the corresponding CV. The oxidation currents measured in both cases correspond well to ring UME theory [17] for electrodes with ring diameters of 2 µm and 25 µm, respectively. Based on microscopical studies and evaluation of recorded CVs and according to the theory of ring UME voltammetry [17], a thickness of the platinum film of <50 nm can be estimated for both polished and unpolished probes.

To investigate the response of the probes approaching conducting and non-conducting surfaces, PACs towards gold and polymer on a model substrate were performed. In **Figure 4.1.2a**, the SECM feedback curves of a 25-µm ring diameter probe approaching both conductor (gold) and isolator (polymer) are displayed. The typical positive and negative feedback responses were found. For SICM, a response-independent conductivity was expected. The corresponding PAC is shown in **Figure 4.1.2b**. Approaching the surface resulted in initially slowly decreasing current, possibly due to potential shift during the measurement. Nevertheless, when substrate-to-tip distance similar to the pipette aperture radius was reached, the current decreased drastically due to hindered ion migration between pipette interior and bulk solution. Overall, the approach responses indicated proper functionality of the dual probes.

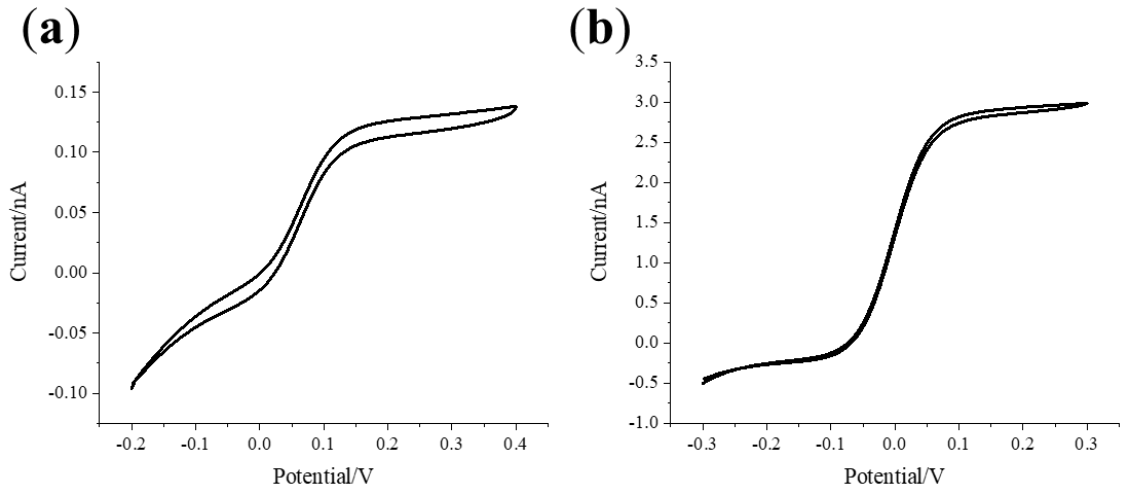

Figure 4.1.1: Cyclic voltammograms (**a**) with an unpolished pipette probe with a ring OD of 2 µm, (**b**) with a polished pipette probe with a ring OD of 25 µm. Scan rate: 20 mV s^{-1}. A Pt wire served as quasireference/counter electrode in a solution containing 1.5 mM FcMeOH and 0.2 M KNO_3.

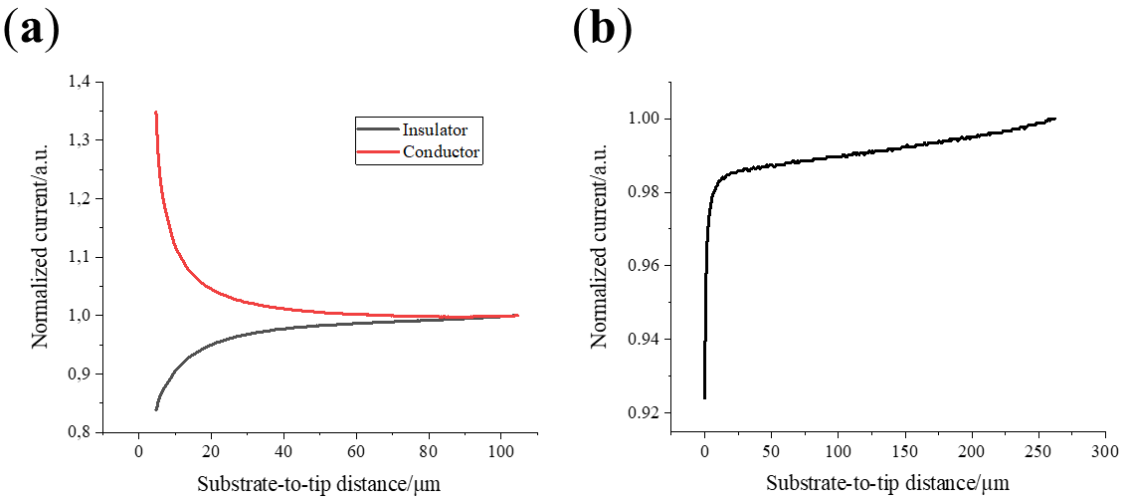

Figure 4.1.2: PACs of a 25 µm OD dual SECM/SICM probe. (**a**): SECM PACs, approaching platinum (conductor, red) and insulating polymer (insulator, black). E (Probe) = 0.3 V (**b**): SICM PAC. E (Probe) = 0.2 V.

Images of the screen-printed model substrate were recorded to test the capability of the fabricated probes to perform simultaneous local topographical and conductivity studies. **Figure 4.1.3** shows the SECM (**a**) and SICM (**b**) responses at the edge of the conductive electrode area. The SECM image clearly shows a sharp current transition from the conducting gold area in the left half of the image to the insulating polymer in the right half, as positive and negative feedback were measured on the left and right side, respectively. The SICM response indicates a significant roughness over the entire area of the sensor. In addition, overall current increase from the conducting to the insulating area shows that the sensor is thicker at the electrode area, since the electrode material was printed onto the polymer carrier. Both observations could be confirmed by digital micrographs (**Figure 4.1.4:** Photo of the model substrate (top

right) and digital micrograph showing the topography of the area within the orange highlighted area (bottom).).

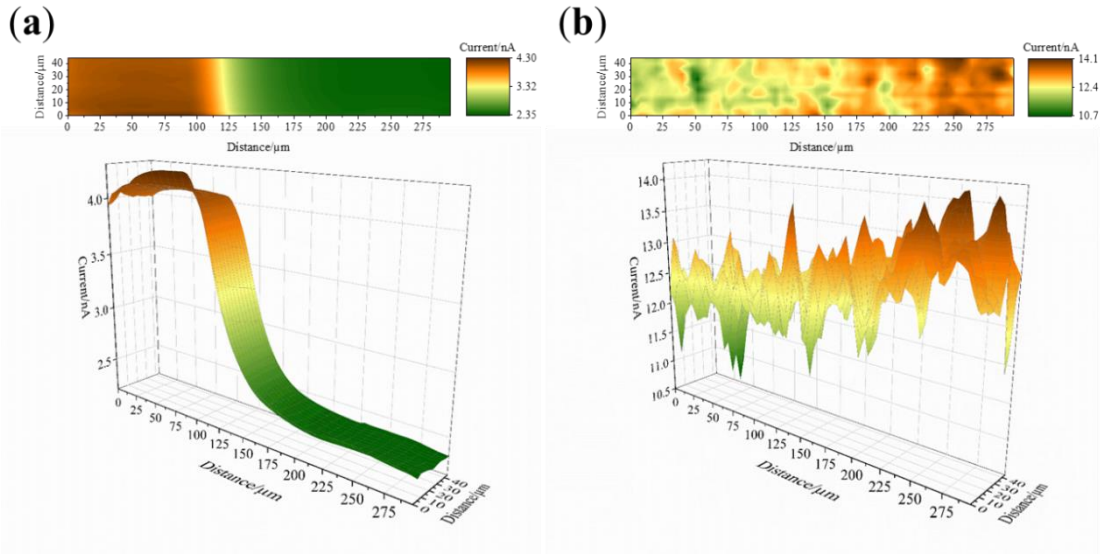

Figure 4.1.3: (**a**) Electrochemical activity (SECM) and (**b**) topographical (SICM) images of an electrochemical sensor substrate obtained via simultaneous SECM and SICM recordings. 2D (top) and 3D (bottom) projections are shown. An area of 45×300 µm was investigated, covering the edge of the working electrode pad of the sensor. E (Probe, SECM) = 0.3 V. E (Probe, SICM) = 0.2 V. Scan rate: 40 µm s^{-1}. Quiet time: 10 s.

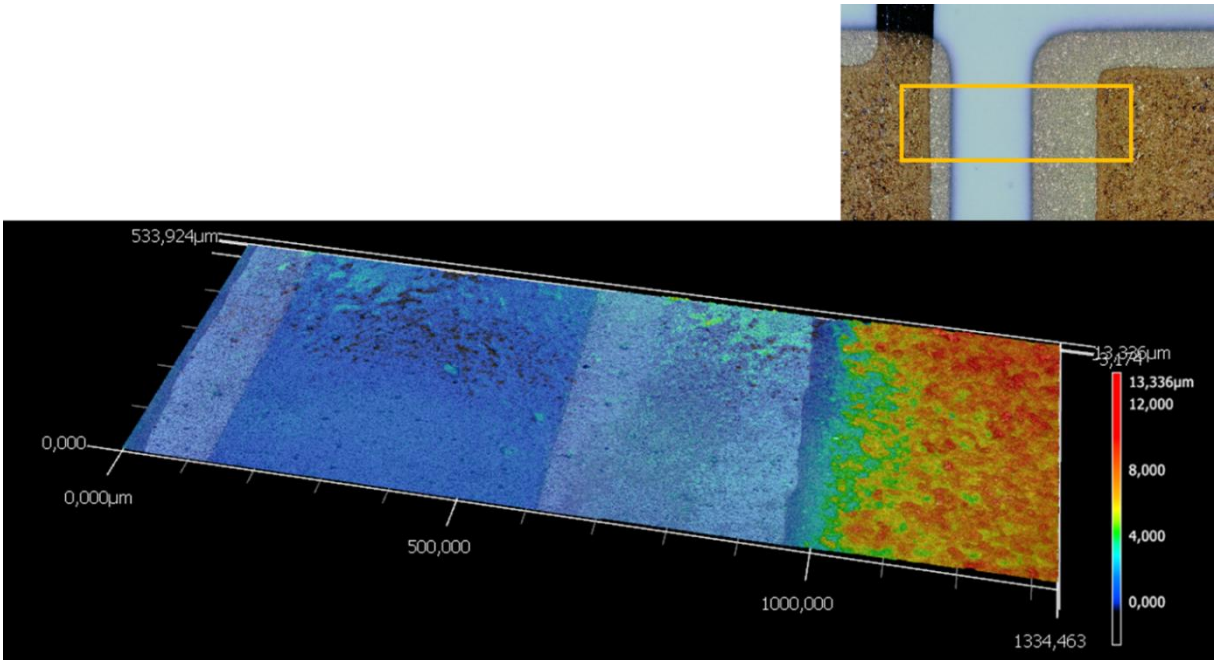

Figure 4.1.4: Photo of the model substrate (top right) and digital micrograph showing the topography of the area within the orange highlighted area (bottom).

Furthermore, the fabricated SECM–SICM probes were utilized to investigate a porous BDD sample regarding its electrochemical surface properties in relation to topography. In **Figure 4.1.5a**, the SECM image showing overlapping electrochemical and topographical information

is presented. Locations exhibiting higher currents indicated either the occurrence of higher electrochemical activity or topographical extrusion of the surface. To differentiate between these two types of information, the SICM image displayed in **Figure 4.1.5b** can be utilized, covering the same area previously investigated via SECM. Herein, low current areas as a result of a small substrate-to-tip distance indicate the presence of topographical elevation. Digital micrographs of the sample, shown in **Figure 4.1.5c**, support these observations. Extrusions generally occur in the same locations where the high current was observed in the SECM image. Nevertheless, deviations were noticeable, as areas exhibiting both low electrochemical activity and topological extrusions occurred as well. Therefore, variations in the SECM might be caused by both inhomogeneous topography and porosity of the sample, in addition to electrochemical differences. The latter is possibly a consequence of non-uniform distribution of boron doping ratio within the BDD layer. Similar observations were made for nonporous BDD samples [24].

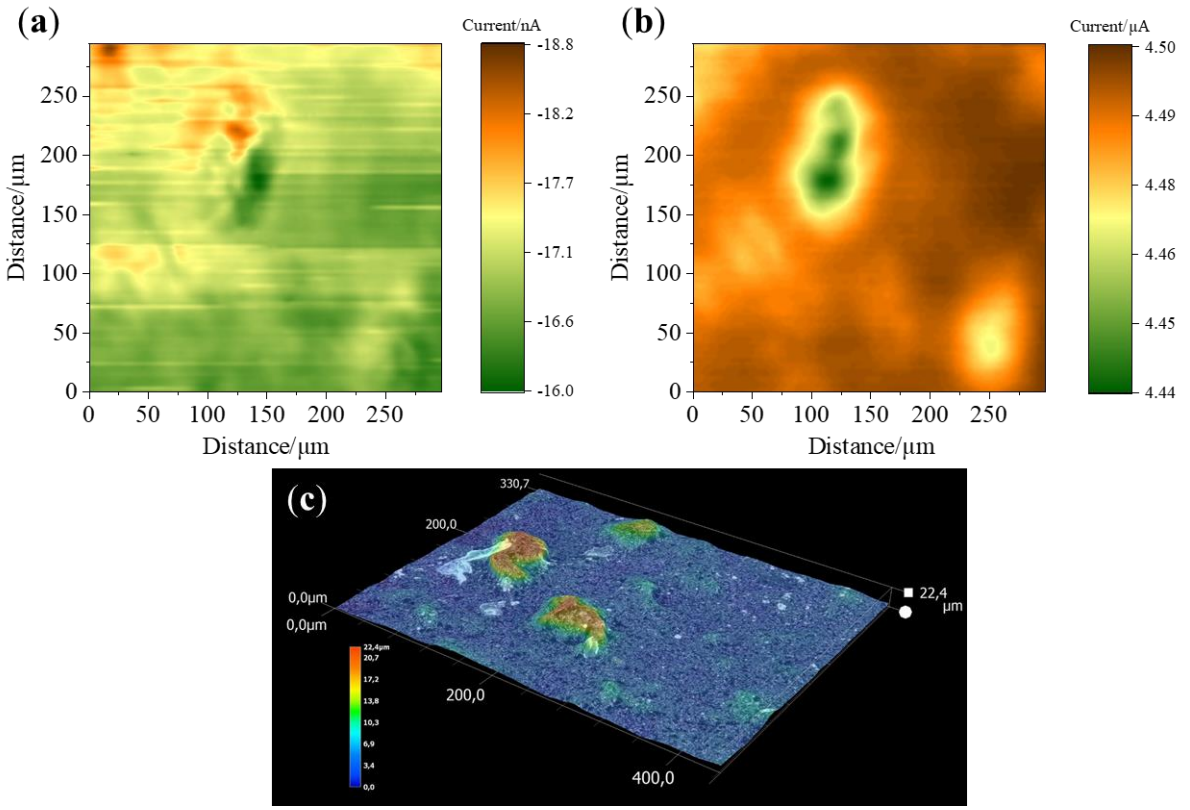

Figure 4.1.5: (**a**) SECM and (**b**) SICM images of a porous BDD sample, recorded simultaneously. An area of 294×294 µm was scanned. Increment distance: 3 µm; mediator for SECM: $Ru(NH_3)_6Cl_3$; E (Probe, SECM) = −0.4 V. E (Substrate, SECM) = 0.0 V. E (Probe, SICM) = 0.2 V. Scan rate: 30 µm s^{-1}. Quiet time: 60 s. (**c**): Optical micrograph of a porous BDD sample showing the topographical characteristics.

4.1.3. Conclusion

A new approach for the fabrication of probes suitable for simultaneous SECM and SICM measurements was developed and functional probes of different size were successfully manufactured. In addition, the materials and instruments required for the preparation of probes are cost efficient and easy to acquire. The probes were characterized via CV, SEM images, and PACs towards isolating and conducting surfaces. Electrochemical and topographical variations at a model substrate surface as well as a porous BDD sample could be resolved. The probe preparation concept suggested in this work facilitates the widespread use of combined SECM and SICM as a means for simultaneous non-contact topographical and electrochemical activity studies of surfaces.

4.1.4. Experimental

All experiments were carried out with ferrocenemethanol (c = 1.5 mM, FcMeOH, 99%, ABCR, Karlsruhe, Germany) or hexaaminеruthenium(III) chloride (c = 1.5 mM, $Ru(NH_3)_6Cl_3$, ABCR, Karlsruhe, Germany) as a redox mediator. To prepare aqueous solutions, Milli-Q water (Milli-Q Advantage A10 system, Merck Millipore, Darmstadt, Germany) was used. KNO_3 (c = 0.2 mM, analytical grade, Merck KGaA, Darmstadt, Germany) and KCl (c = 0.2 M, analytical grade, Merck KGaA, Darmstadt, Germany) served as supporting electrolytes. A 10:1 mixture of SU8.5 photoresist (MicroChem Corp., Westborough, Massachusetts) and ethanol (Merck Millipore, Burlington, Massachusetts) was utilized for preparing isolating coatings.

4.1.5. Instrumentation

Probes were fabricated by modifying platinum-coated emitters for electrospray ionization (New Objective, Woburn, Massachusetts). The fabrication protocol is illustrated in **Figure 4.1.6**. Initially, the capillaries were pushed through a copper tube (1.1 mm ID, 2.0 mm OD, 3.0 cm length, Albion Alloys, Bournemouth, United Kingdom) for establishing electrical contact to the platinum surface of the probes. Contact between copper and platinum was established using silver conductive paint (VS Electronic, Aschaffenburg, Germany) and adhesive (UHU Max Repair Extreme, UHU GmbH & Co. KG, Bühl, Germany). Afterwards, a photoresist solution was applied under N_2 flow, cured by UV light (350 nm, applied for 30 s) and heated in an oven at 95 °C for 5 min to evaporate the remaining solvent. The quality of the coating was investigated by CV and the coating process was repeated if the measured currents were too high. If larger probes were desired, an alternative way to expose a ring electrode surrounding was applied. The tips were polished with alumina lapping sheets (0.3 µm, Precision Surfaces

International, Houston, Texas), while water was flushed through the pipette to prevent clogging.

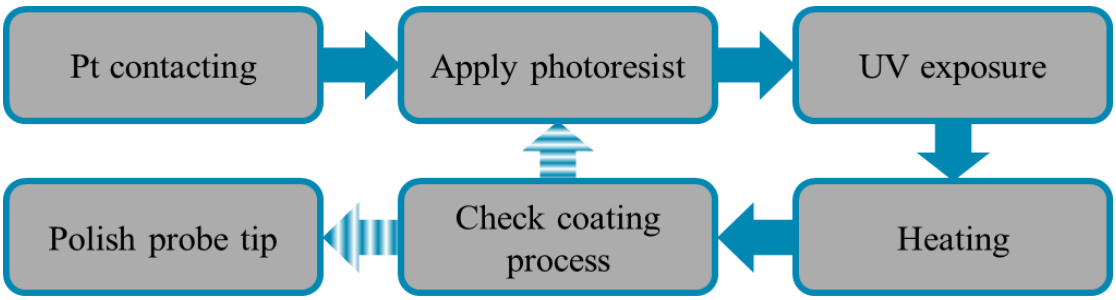

Figure 4.1.6: Probe fabrication scheme. To obtain a functional probe, multiple layers had to be applied or the tip needed to be polished.

Eventually, probes were filled with supporting electrolyte and a Ag/AgCl wire was inserted. **Figure 4.1.7a** shows a typical example of a finished tip. The individual layers of the probe tip are schematically shown in **Figure 4.1.7b**. An image of the tip recorded with a SEM (JSM-6400F, Jeol Ltd., Akishima, Japan) is depicted in **Figure 4.1.7c**.

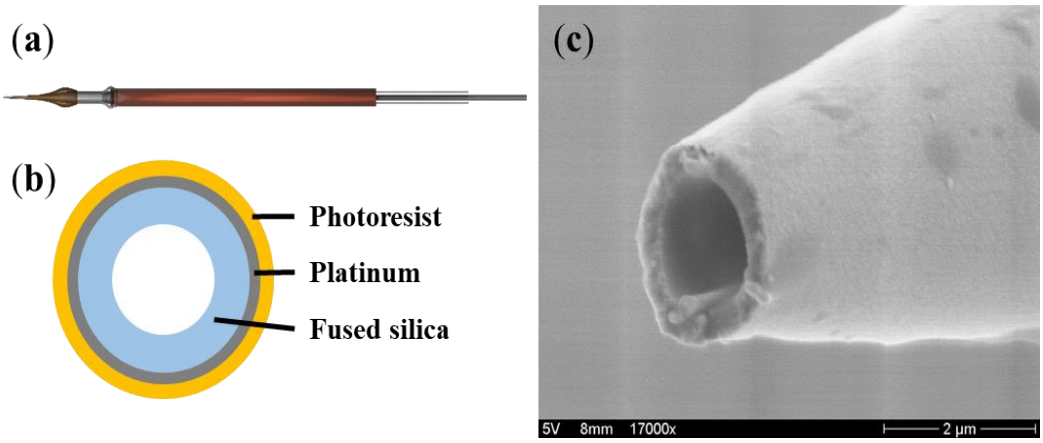

Figure 4.1.7 (**a**): Model of a pipette probe used for SECM/SICM. (**b**): Schematic view of the tip of the probe, highlighting different components of the pipette. (**c**): SEM image of an unpolished pipette probe.

Experiments with the fabricated probes were performed with a second Ag/AgCl wire placed in the bulk solution employed as both counter and reference electrode for SECM measurements. The mentioned potentials herein refer to this reference system if not stated otherwise.

Measurements were performed using a commercially available SECM 920C (CH Instruments, Austin, Texas), with the first electrode channel being connected to the internal Ag/AgCl wire of the ring UME pipette for recording the SICM current and the second channel connected to the copper tube for measuring the SECM current.

The approach response of the fabricated probes was investigated by performing PACs over both gold and polymer of a screen-printed electrochemical sensor (**Figure 4.1.8a**, **b**, GlucoSmart® Swing, MSP bodmann GmbH, Germany) as conductive and non-conductive

surfaces, respectively. A potential of 0.3 V (SECM) was applied and the probe was approached until the SECM current increased to 135% (conductor) or decreased to 85% (insulator) with respect to the current measured in bulk solution. In addition, a quiet time of 60 s was applied prior to approaching and the scan rate was set to 1.25 µm s^{-1}.

For simultaneous SECM and SICM measurements, the contact pads of the same sensor served as a model substrate. Its roughness and the transition between conducting and insulating surface were investigated. Potentials of 0.3 V (SECM) and 0.2 V (SICM) were applied and FcMeOH served as a redox mediator. The scan rate of the probe was 40 µm s^{-1} with a pixel size of 4 µm.

Porous BDD samples were deposited on conductive p-Si wafers with a planar BDD base layer using an ASTeX 5010 (Seki Technotron, Japan) deposition system under the following conditions: 0.5% of methane in hydrogen, gas pressure equal to 50 mbar, microwave power of 1150 W, and substrate temperature of ca. 750 °C. Boron doping was carried out by the addition of trimethylboron in the gas phase to give a B/C ratio of 4000 ppm. Porous BDD samples were obtained by two-step diamond deposition (a growth duration of each step was 5 h) on a ca. 4–5 µm thick 3D template comprising of nanodiamond seeded SiO_2 nanofibers in a polymer solution, which was spin coated (at 3000 rpm for 30 s) on top of a planar BDD base layer and then dried on a hot plate (110 °C/90 s). The surface of fabricated porous BDD samples was hydrogen terminated (as-grown).

The BDD samples were mounted onto a substrate holder prior to measurements (**Figure 4.1.8c**), enabling a well-defined potential setting of the BDD sample. The sample holder consisted of a brass rod sealed with polyvinyl chloride (brass diameter: 3 mm, outer diameter of the polyvinyl chloride hollow cylinder: 6.5 mm, fabricated by the mechanical workshop of the University of Regensburg), with the rod exceeding on one end to facilitate electrical contact and another fat end where porous BDD samples were mounted. Electrical contact between porous BDD and brass rod was established by applying silver conductive paint on the rod and placing the porous BDD sample on top. After drying at room temperature for 1 h, the gap between rod and sample was sealed with epoxide resin (UHU plus endfest 300, UHU GmbH & Co. KG, Bühl, Germany). After hardening of the resin, which required 24 h, the remaining gaps were filled with epoxy resin as before. Excess resin was removed by carefully polishing the edges of the sample with abrasive paper (grit size 100) until the sample fit into the electrochemical cell shown in **Figure 4.1.8d**. Porous BDD samples were measured with $Ru(NH_3)_6Cl_3$ as a mediator, applying 0.0 V to the substrate and −0.4 and 0.2 V to the SECM and SICM parts of the probe, respectively. An area covering 294×294 µm was investigated with a scan rate of 30 µm s^{-1} and a pixel size of 3 µm. Initial surface studies of the samples were performed with a digital microscope (VHX-7000, Keyence, Osaka, Japan).

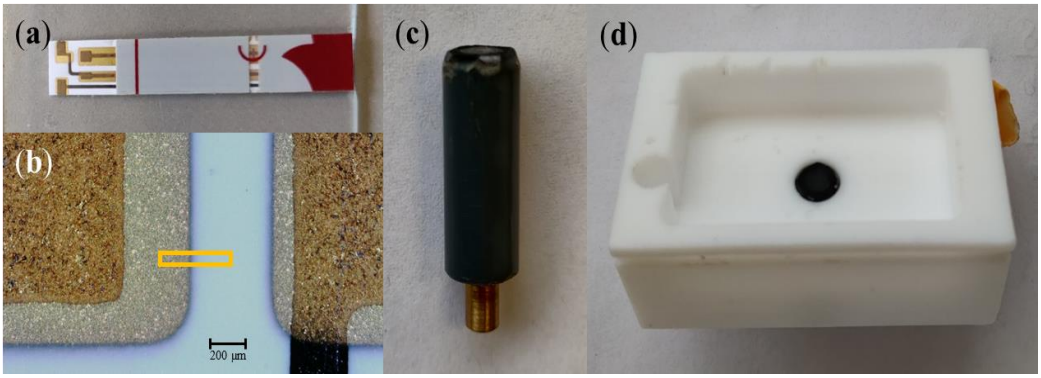

Figure 4.1.8: (**a**) Image of the electrochemical sensor used as a model substrate. (**b**) Zoomed view of the electrode pads of the glucose sensor with the area investigated by means of SECM/SICM highlighted in yellow. (**c**) BDD sample mounted onto a sample holder. (**d**) BDD sample with sample holder mounted in the electrochemical cell used for measurements.

References

1. Bard AJ, Mirkin MV (2012) Scanning electrochemical microscopy, 2nd ed. CRC Press, Boca Raton, Fla

2. Macpherson JV, Unwin PR (2000) Combined scanning electrochemical-atomic force microscopy. Anal. Chem. 72(2):276–285

3. Velmurugan J, Agrawal A, An S, Choudhary E, Szalai VA (2017) Fabrication of Scanning Electrochemical Microscopy-Atomic Force Microscopy Probes to Image Surface Topography and Reactivity at the Nanoscale. Anal. Chem. 89(5):2687–2691

4. Hansma PK, Drake B, Marti O, Gould SA, Prater CB (1989) The scanning ion-conductance microscope. Science (New York, N.Y.) 243(4891):641–643

5. Comstock DJ, Elam JW, Pellin MJ, Hersam MC (2010) Integrated ultramicroelectrode-nanopipet probe for concurrent scanning electrochemical microscopy and scanning ion conductance microscopy. Anal. Chem. 82(4):1270–1276

6. Takahashi Y, Shevchuk AI, Novak P, Murakami Y, Shiku H, Korchev YE, Matsue T (2010) Simultaneous noncontact topography and electrochemical imaging by SECM/SICM featuring ion current feedback regulation. J. Am. Chem. Soc. 132(29):10118–10126

7. Takahashi Y, Shevchuk AI, Novak P, Zhang Y, Ebejer N, Macpherson JV, Unwin PR, Pollard AJ, Roy D, Clifford CA, Shiku H, Matsue T, Klenerman D, Korchev YE (2011) Multifunctional nanoprobes for nanoscale chemical imaging and localized chemical delivery at surfaces and interfaces. Angew. Chem. Int. Ed. 50(41):9638–9642

8. O'Connell MA, Wain AJ (2014) Mapping electroactivity at individual catalytic nanostructures using high-resolution scanning electrochemical-scanning ion conductance microcopy. Anal. Chem. 86(24):12100–12107

9. Page A, Kang M, Armitstead A, Perry D, Unwin PR (2017) Quantitative Visualization of Molecular Delivery and Uptake at Living Cells with Self-Referencing Scanning Ion Conductance Microscopy-Scanning Electrochemical Microscopy. Anal. Chem. 89(5):3021–3028

10. Thakar R, Weber AE, Morris CA, Baker LA (2013) Multifunctional carbon nanoelectrodes fabricated by focused ion beam milling. Analyst 138(20):5973–5982

11. Morris CA, Chen C-C, Baker LA (2012) Transport of redox probes through single pores measured by scanning electrochemical-scanning ion conductance microscopy (SECM-SICM). The Analyst 137(13):2933–2938

12. O'Connell MA, Lewis JR, Wain AJ (2015) Electrochemical imaging of hydrogen peroxide generation at individual gold nanoparticles. Chem. Commun. (Cambridge, England) 51(51):10314–10317

13. Takahashi Y, Kumatani A, Shiku H, Matsue T (2017) Scanning Probe Microscopy for Nanoscale Electrochemical Imaging. Anal. Chem. 89(1):342–357

14. Szabo A (1987) Theory of the current at microelectrodes: application to ring electrodes. J. Phys. Chem. 91(11):3108–3111

15. Walsh DA, Fernández JL, Mauzeroll J, Bard AJ (2005) Scanning electrochemical microscopy. 55. Fabrication and characterization of micropipet probes. Anal. Chem. 77(16):5182–5188

16. Cornut R, Mayoral M, Fabre D, Mauzeroll J (2010) Scanning Electrochemical Microscopy Approach Curves for Ring Microelectrodes in Pure Negative and Positive Feedback Mode. J. Electrochem. Soc. 157(7):F77

17. Lee Y, Amemiya S, Bard AJ (2001) Scanning electrochemical microscopy. 41. Theory and characterization of ring electrodes. Anal. Chem. 73(10):2261–2267

18. Muzyka K, Sun J, Fereja TH, Lan Y, Zhang W, Xu G (2019) Boron-doped diamond: current progress and challenges in view of electroanalytical applications. Anal. Methods 11(4):397–414

19. Baluchová S, Daňhel A, Dejmková H, Ostatná V, Fojta M, Schwarzová-Pecková K (2019) Recent progress in the applications of boron doped diamond electrodes in electroanalysis of organic compounds and biomolecules - A review. Anal. Chim. Acta 1077:30–66

20. Zanin H, May PW, Fermin DJ, Plana D, Vieira SMC, Milne WI, Corat EJ (2014) Porous boron-doped diamond/carbon nanotube electrodes. ACS Appl. Mater. Interfaces 6(2):990–995

21. Baluchová S, Taylor A, Mortet V, Sedláková S, Klimša L, Kopeček J, Hák O, Schwarzová-Pecková K (2019) Porous boron doped diamond for dopamine sensing: Effect of boron doping level on morphology and electrochemical performance. Electrochim. Acta 327:135025

22. Holt KB, Bard AJ, Show Y, Swain GM (2004) Scanning Electrochemical Microscopy and Conductive Probe Atomic Force Microscopy Studies of Hydrogen-Terminated Boron-Doped Diamond Electrodes with Different Doping Levels. J. Phys. Chem. B 108(39):15117–15127

23. Ryl J, Burczyk L, Zielinski A, Ficek M, Franczak A, Bogdanowicz R, Darowicki K (2019) Heterogeneous oxidation of highly boron-doped diamond electrodes and its influence on the surface distribution of electrochemical activity. Electrochim. Acta 297:1018–1027

24. Neufeld AK, O'Mullane AP (2006) Effect of the mediator in feedback mode-based SECM interrogation of indium tin-oxide and boron-doped diamond electrodes. J. Solid State Electrochem. 10(10):808–816

4.2. Scanning electrochemical microscopy of electrically heated wire substrates

Stefan Wert, Alexander Fußstetter, Christian Iffelsberger and Frank-Michael Matysik

Molecules 25 (2020): 1169.

This chapter was published in the journal above and was changed for reasons of uniformity. The changes herein consist of minor corrections, formatting, and the addition of the supporting information to the main text.

Abstract

We report a new configuration for enhancing the performance of scanning electrochemical microscopy (SECM) via heating of the substrate electrode. A flattened Pt microwire was employed as the substrate electrode. The substrate was heated by an alternating current, resulting in an increased mass transfer between the wire surface and the bulk solution. The electrochemical response of the Pt wire during heating was investigated by means of cyclic voltammetry. The open circuit potential of the wire was recorded over time, while varied heating currents were applied to investigate the time needed for establishing steady-state conditions. Diffusion layer studies were carried out by performing probe approach curves for various measuring modes of SECM. Finally, imaging studies of a heated substrate electrode surface, applying feedback, substrate generation/tip collection, and the competition mode of SECM, were performed and compared with room temperature results.

4.2.1. Introduction

Thermoelectrochemistry is a discipline that adds the temperature parameter to the three classical parameters of electrochemistry, known as voltage, current, and time. In a heated electrolyte solution, the resulting increased mass transport yields a higher rate of analyte conversion at the electrode surface. In such an environment, special attention is required to maintain a constant temperature around the reference electrode to prevent a shift of its potential. However, this can be neglected if heating is limited to the area closest to the working electrode, also known as non-isothermal heating. In recent research, non-isothermal heating was mostly achieved either by directly heating the electrode [1] or by irradiating the nearby solution with microwaves [2, 3]. Heated electrodes have been utilized in various applications—for example, for DNA investigation [4–6] or in a thermoresponsive glucose biosensor [7]. Direct application of heat to electrodes was also used for electrode cleaning [8] and prevention of

fouling [9]. The kinetics and heat transport processes at such electrodes were extensively studied as well [10–12]. In addition, the electrochemical behavior of many substances, such as nicotinamide adenine dinucleotide [8], have been characterized using heated electrodes. A convenient way of heating electrodes is the application of an alternating current (100 kHz) to microwires. This technique, based on the work of Gründler et al., is termed “hot-wire electrochemistry” [13, 14]. Usually, gold or platinum microwires with a diameter of about 25 µm are employed as cylindrical electrodes in corresponding hot-wire configurations. Due to the microwires’ low heat capacity, it is possible to change the electrode temperature very rapidly, and even beyond the boiling point of the surrounding solution for a brief moment. Hot-wire electrochemistry has been applied for trace detection of elements like arsenic [15], copper, and mercury [16]. This was also done to compare the performance of a heated wire electrode to a rotating disk electrode, with lower limits of detection achieved using the hot-wire setup. The effects of convection and temperature on the hybridization of DNA and RNA have been investigated as well [17]. Recently, the oxidation kinetics of acetaminophen (paracetamol) was studied, comparing the results obtained using a heated microwire in a cooled electrolyte versus using a rotating disk electrode in heated solution [18]. Further improvements to the hot-wire setup have been achieved by modifying the surface of gold microwires depositing carbon nanotubes, which resulted in increased reversibility of voltammetric experiments [19]. For the electrochemical characterization of surfaces, scanning electrochemical microscopy (SECM) has become an established technique [20–23]. Its key component is an ultramicroelectrode (UME), which is scanned across a surface or interface of interest. A variety of measurement modes can be applied, with the most common ones being the feedback, substrate generation/tip collection (SG/TC), and competition modes. In feedback mode, measurements are carried out in a solution containing a redox-active mediator species while a potential is applied at the UME, resulting in conversion of the mediator at a rate that is dependent on the electrochemical activity and topography of the surface of interest. In SG/TC mode, the species converted at the probe is generated at the substrate, with no detectable species present in the bulk solution, resulting in a lower background current. This is a frequently applied measuring mode, e.g., to study corrosion processes [24–26]. In competition mode, the same potential is applied to probe and substrate, enabling the investigation of the catalytic activity of surfaces [27]. Both SG/TC and competition mode suffer from the limitation of a growing diffusion layer at macroscopic substrates over time, resulting in poor reproducibility of repeated measurements. To overcome this problem, our group has introduced forced convection into the SECM cell, either by stirring [28] or by a flow of the electrolyte solution [29], resulting in a rapidly established steady-state diffusion layer. In addition, forced convection led to a higher contrast in feedback mode measurements [30].

Since heating the electrolyte results in an increased convection rate, the non-isothermal approach increases mass transport exclusively near the heated electrode. Boika et al. have made use of this effect by employing heated UMEs as probes in SECM. They refer to this as “hot tip SECM” [31, 32]. Other groups have investigated the impact of heated samples, showing that temperature impacts the contrast between conductive/non-conductive areas in feedback mode [33], as well as the possibility of altering the activity of immobilized enzymes on surfaces during SECM studies [34]. Numerical simulations have enabled the estimation of convective effects in SECM measurements resulting from temperature differences between the electrolyte and the surrounding environment [35]. The open circuit potential (OCP) of a UME can be used to determine the local temperature at the electrode/electrolyte interface [36]. Another method was described by using a thermocouple probe in conjunction with SECM [37].

In this work, we present a novel hot-wire electrochemistry setup, featuring flattened microwires suitable for SECM studies under well-defined substrate temperature conditions. The steady-state voltammetric behavior under heat application is shown. For several measuring modes of SECM, approach curves of heated wire substrates have been studied, and imaging experiments have been carried out.

4.2.2. Results and discussion

The effect of heating the wire electrode on cyclic voltammograms (CVs) was studied in 5 mM ferro/ferricyanide by applying different magnitudes of alternating current (AC). **Figure 4.2.1** shows CVs recorded while different heating currents were applied. The resistance of the flattened wire (width = 70 µm) substrate at room temperature was 5.8 Ω. Without heating, a CV with the typical shape for a quasi-reversible, one-electron transfer reaction with significant contribution of planar diffusion was obtained (black curve). Upon applying increasing heating currents, steady-state voltammetric responses could be established. This trend corresponded well to the effects observed when forced convection is introduced to macroelectrodes or when decreasing the electrode size down to dimensions for an UME. Disturbances in the voltammetric response started to occur when the wire was heated close to the boiling point of the electrolyte solution, causing the formation of bubbles at the electrode surface (green curve in **Figure 4.2.1a**). The in-situ heating of the wire induced a potential shift towards lower potentials. The half-wave potentials of the recorded CVs could be used to determine the temperature of the wire/solution interface, shown in **Figure 4.2.1b**. Based on this, it was found that a temperature of 57.4 °C (corresponding to a heating current of 322 mA) was sufficient to eliminate the hysteresis of the CVs of the investigated electrochemical system. A linear correlation between heating current and wire/solution interface temperature could be observed as well.

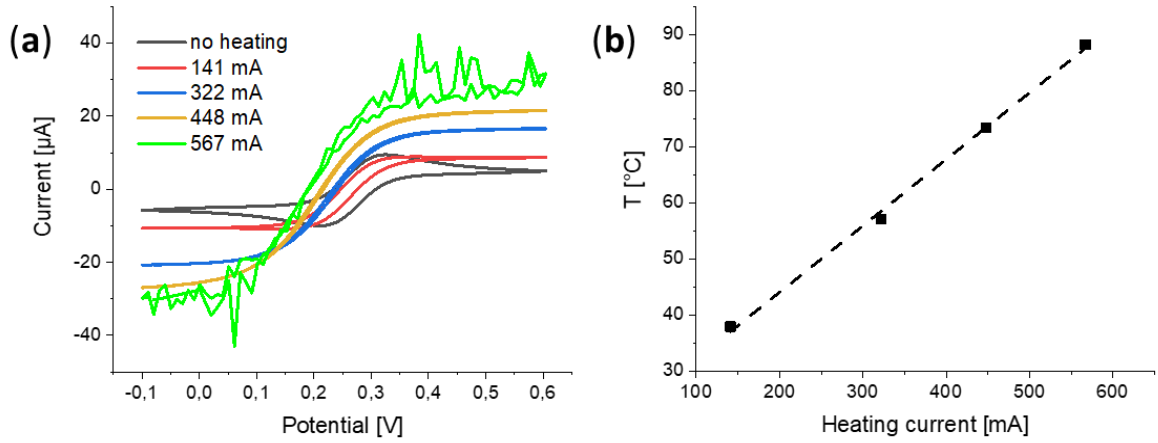

Figure 4.2.1 (**a**): CVs of a flattened Pt wire (width, 70 µm) in 5/5 mM ferro/ferricyanide solution with 1.0 M KNO_3 as supporting electrolyte. The applied AC at the wire varied between the CVs. Scan rate: 100 mV s^{-1}. (**b**): Plot of heating currents applied at the wire during CVs and their respective temperatures, obtained from half-wave potentials.

In the following section, the substrate electrode was studied in a physiologically relevant temperature region. For the investigation of temperature changes directly at the substrate, the OCP dependent on the applied heating AC was measured, which is in direct correlation with the temperature. **Figure 4.2.2** shows the OCP measured at a hot-wire substrate over the course of 250 s, while the heating AC was changed every 20 s. Initially, no heating current was applied, and a temperature of 24 °C was measured. Upon increasing the heating current stepwise to 188 mA, the temperature reached values above 37 °C. However, the time required to establish a stable OCP increased with larger heating steps. For example, a stable OCP was observed after less than 10 s when increasing the AC from 0 to 78 mA, whereas stabilization took longer with increasing heating currents. The opposite effect was observed when decreasing the heating AC stepwise. As the applied AC was decreased from 188 to 131 mA, the temperature stabilized at 32 °C within 20 s. Lowering the AC further led to a prolonged time being needed to establish a constant temperature at the wire, since the heated glass substrate under the wire prevented it from cooling down. Quick temperature adjustments can be done at the wire within seconds; however, larger changes require more time.

The influence of different temperatures of the flattened wire substrate on the approach response of probes in different SECM operational modes was investigated in a solution of ferrocenemethanol (FcMeOH). **Figure 4.2.3** illustrates probe approach curves (PACs) recorded in different measuring modes while heating ACs of different magnitude were applied at the wire. In feedback mode (**Figure 4.2.3a**), the substrate-to-tip region where the feedback response started to occur remained the same for all temperatures investigated. An overall increase of current was observed when the wire was heated, with a greater impact close

to the substrate, since a vertical temperature gradient was established. In SG/TC mode (**Figure 4.2.3b**), heating influenced the diffusion layer around the wire. At higher temperatures, currents started to increase at shorter substrate-to-tip distances, as the diffusion layer thickness tended to decrease. The thinner diffusion layer resulted in higher currents close to the wire, in contrast to lower currents at larger distances. The occurrence of a shrunken diffusion layer at higher temperatures was observed in the competition mode approach curves (**Figure 4.2.3c**) as well. Within the diffusion layer, currents decreased as the probe approached the substrate, since the latter consumed most of the FcMeOH. At large substrate-to-tip distances, higher currents were measured when heating was applied, since convection was increased, and thus more mediator reached the active area of the UME. In addition, in the region out of feedback or diffusion layer range, currents slightly increase in the feedback and competition mode approach curves (**Figure 4.2.3a**, **c**) when the wire was approached. This indicated the presence of a temperature gradient connected with a higher rate of mass transport closer to the wire.

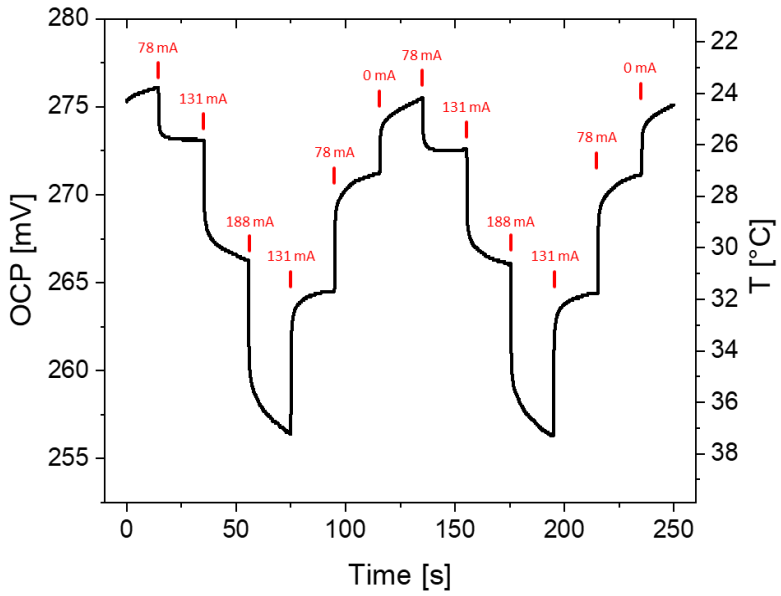

Figure 4.2.2: OCP measured over time at a flattened wire substrate in a solution of 5/5 mM ferro/ferricyanide and 1.0 M KCl. The applied alternating current was varied in time intervals of 20 s (indicated by red marks), and the change in OCP with the corresponding temperature was monitored.

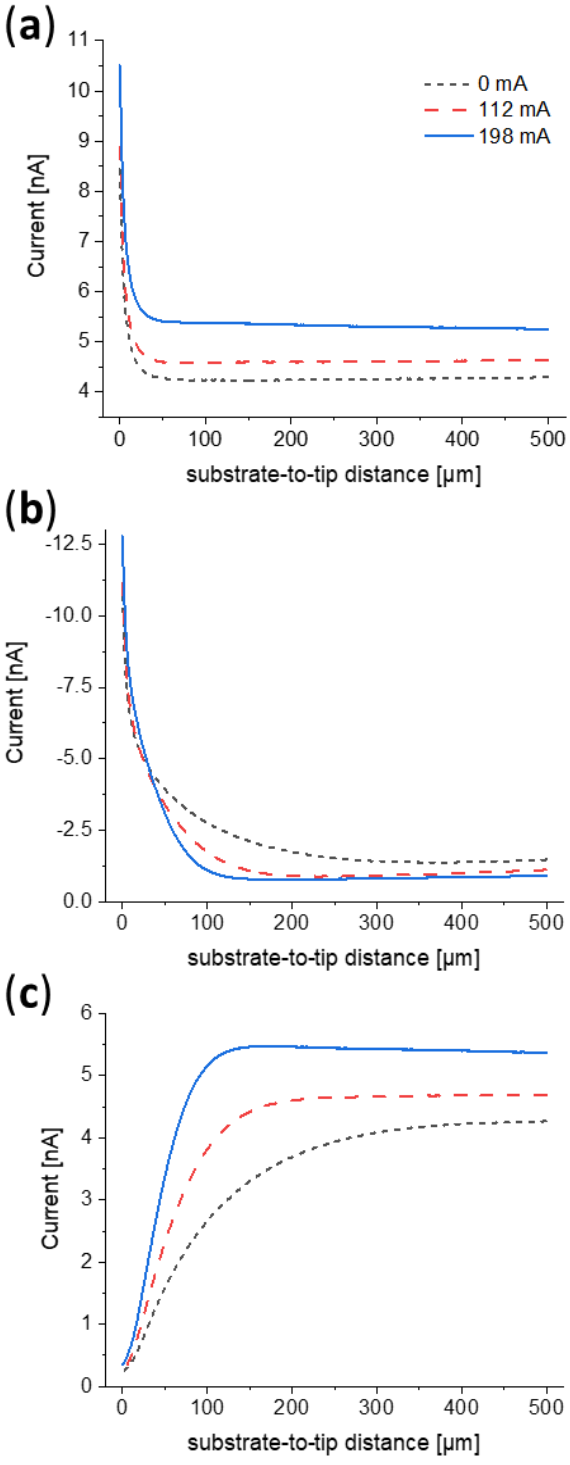

Figure 4.2.3: PACs with a 25 µm probe towards a flattened Pt wire in different SECM operation modes for different heating currents flowing through the wire. Measurements were carried out in 1.5 mM FcMeOH and 200 mM KNO_3. (**a**): Feedback mode: E (probe) = 0.5 V. (**b**): SG/TC mode: E (probe) = 0.0 V, E (wire) = 0.5 V. (**c**): Competition mode: E (probe) = E (wire) = 0.5 V.

The effect of heating of a flattened wire on corresponding SECM images studies in different operational modes is shown in **Figure 4.2.4**. All measurements were done in the constant-height mode. In feedback mode (**Figure 4.2.4a**), heating yielded significantly higher currents

above both the wire and glass surface, due to increased mass transport following the temperature gradient. The current increase above the latter might be a result of heat transfer between the hot wire and the glass substrate, as they were in direct contact. Nevertheless, a significant improvement of contrast was observable under heated conditions, also corresponding well to the feedback approach curves discussed earlier. As the disk diameter of the active probe area is in the same range as the substrate dimension, the images show an enlarged width of the substrate. In the SG/TC mode images (**Figure 4.2.4b**), drastically increased currents above the wire were observed, while no significant change in the glass region was noticeable upon applying heat. As a result, an image exhibiting higher contrast was obtained. In addition, a more compact and stable diffusion layer around the wire was established by convective effects introduced by heating, leading to a sharper contrast. In competition mode (**Figure 4.2.4c**), the background current increased with heating, while the current near the wire remained at a comparable range as was found without heating. The image recorded with heating shows a much better resolution. This observation could be explained by the formation of a stable and compact diffusion layer around the wire, similar as in the SG/TC image with heating.

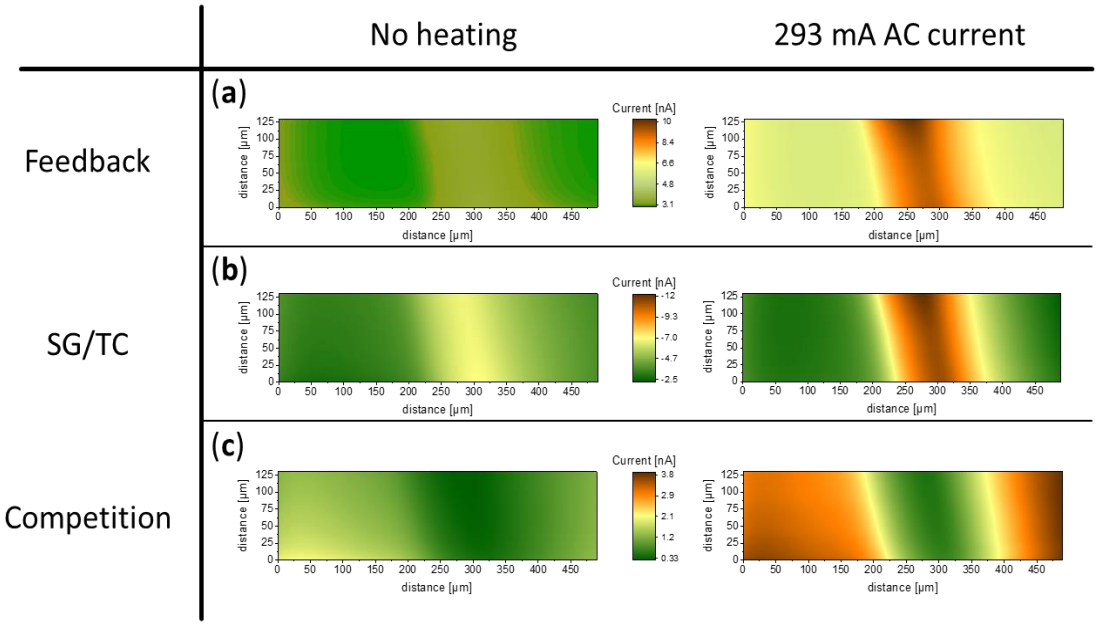

Figure 4.2.4: Images of a flattened Pt wire (width = 70 µm) recorded in different SECM measuring modes, with a 25 µm probe without heating (left side) and with heating (right side). (**a**) Images recorded in feedback mode; (**b**) and (**c**) were obtained in SG/TC and competition mode, respectively. E (Probe) = 0.5 V (feedback and competition mode), 0.0 V (SG/TC mode); E (wire) = 0.5 V (SG/TC and competition mode); scan rate: 100 µm s^{-1}, quiet time 20 s. The probe was approached to a tip-to-wire distance of 7 µm.

4.2.3. Materials and methods

4.2.3.1. Chemicals

For SECM imaging, an aqueous solution of 1.5 mM ferrocenemethanol (FcMeOH, 99%; ABCR, Karlsruhe, Germany) and 0.2 M potassium nitrate (KNO_3, Merck KGaA, Darmstadt, Germany) was used as a mediator solution. All other experiments were carried out in an aqueous solution containing 5 mM of both $K_3(Fe(CN)_6)$ and $K_4(Fe(CN)_6)$, as well as 1 M KNO_3. All solutions were prepared using ultrapure water with a resistivity higher than 18 MΩ cm^{-1} (membraPure, Bodenheim, Germany).

4.2.3.2. Instrumentation

The setup used for all experiments consisted of a commercial SECM (CHI 920C, CH Instruments, Austin, United States), with an electrochemical cell made of polytetrafluoroethylene and a wire heating device, which was used to apply a 100 kHz AC with varying amplitude to Pt wires. Heating intensity could be adjusted by an arbitrary percentage value corresponding to a certain voltage amplitude applied. The heating device was laboratory-built, and mainly consisted of a radio frequency generator and a radio frequency transformer, based on the constructions proposed by Gründler [13]. The working electrode channel of the bipotentiostat, which was used for measurements directly at the heated wire, was connected to the wire heating device, enabling voltammetric measurements without interference from heating AC. A scheme of the configuration is shown in **Figure 4.2.5a**. For the fabrication of flattened microwires, a 3 cm piece of Pt wire with a diameter of 25 µm (Goodfellow GmbH, Hamburg, Germany) was placed between two glass slides, and force was applied using a hammer. To prevent breaking of the glass, the glass slides were placed between polymethylmethacrylate plates. When a flattened wire with a diameter of 70 µm (**Figure 4.2.5b**) was obtained, it was fixed on a glass slide below two additional sheets of glass to prevent wire movement, leaving about 5 mm of blank wire between them. These sheets were adhered using SU8.5 photoresist (Microchem Corp.,Westborough, United States). Hardening of the photoresist was achieved by heating the substrate (95 °C, 5 min) in a convection oven, exposing it to UV light (365 nm, 0.2 W, 30 s), followed by another heating step (95 °C, 5 min). Prior to establishing electrical connections at both ends of the wire, a layer of SU8.5 was applied to the remaining glass substrate, except for the area between the glass sheets, and was then processed as before. This was done to improve the adhesion of hot glue and soldering tin applied later. Both ends of the wire were soldered onto the substrate, together with copper wires (0.5 mm inner diameter, 1.1 mm outer diameter, Pollin Electronic GmbH, Pförring, Germany) that had 5 mm of insulation removed at either end. The soldering joints were sealed by applying hot glue (Pattex, Henkel AG & Co. KGaA, Düsseldorf, Germany).

Figure 4.2.5c shows a finished substrate. It was fixed in the electrochemical cell using a lab-constructed polyether ether ketone sample holder (**Figure 4.2.5d**).

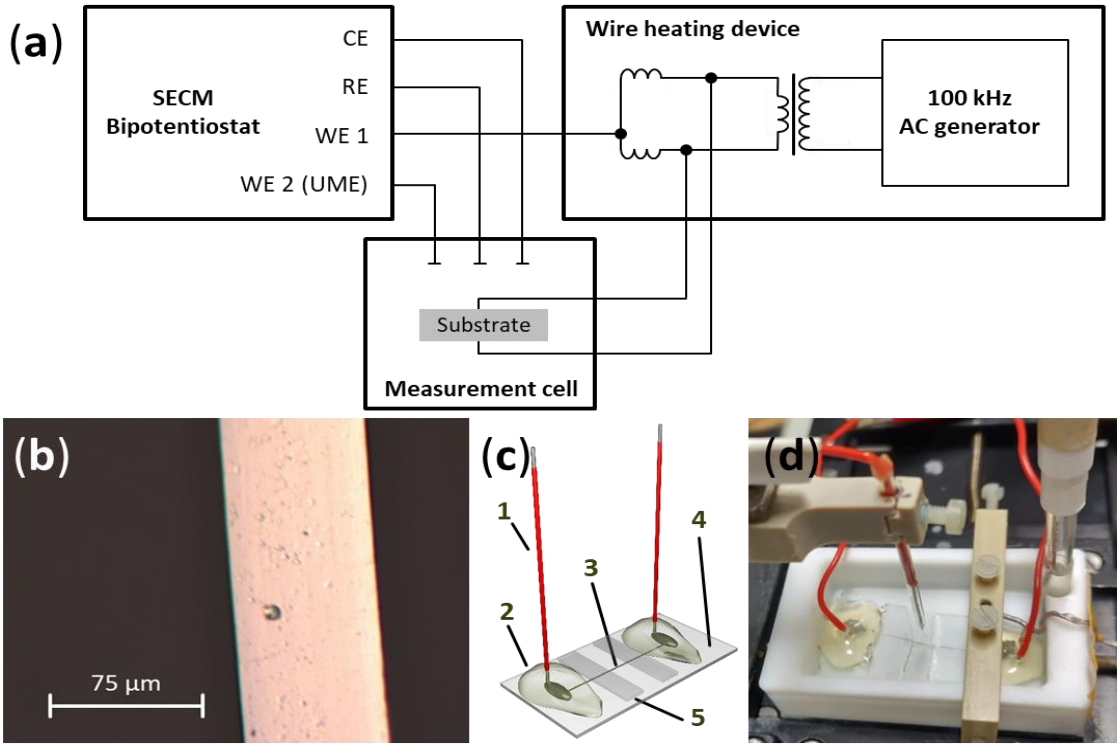

Figure 4.2.5 (**a**)**:** Schematic representation of the experimental setup, showing the electrical connections between the SECM bipotentiostat, AC generator, and measurement cell (scheme adapted from [13]). (**b**): Micrograph of a flattened Pt wire. (**c**): Scheme of a hot-wire substrate used in experiments. 1: Copper cables soldered to the Pt wire. 2: Hot glue for insulation of electrical contacts. 3: Flattened Pt wire. 4: Photoresist-covered glass sheet. 5: Glass sheets for wire stabilization. (**d**): Image of the measurement cell used for SECM measurements, containing electrodes and hot-wire substrate.

Experiments were performed in an electrochemical cell containing redox mediator solution, with a Pt wire as counter electrode and a Ag/AgCl/3M KCl reference electrode immersed into the solution. All potentials mentioned herein refer to this reference system.

Voltammetric studies of the substrate were conducted in a solution of ferro/ferricyanide. The heating current was varied to determine the limit where experiments could be performed. Three consecutive CVs were recorded for each AC current investigated. In addition, chrono-OCP measurements were performed while the heating was varied between 0 and 188 mA, to test the possibility of undergoing quick temperature changes. Substrates were cleaned with isopropanol and water before measurements. Temperature calibration was done in an electrochemical cell connected to Peltier elements (KIMILAR, TEC1-12706). An external current was applied to the Peltier elements to establish different temperatures, and three consecutive CVs were recorded. The corresponding temperatures, measured with a thermometer, could then be related to the respective half-wave potentials. The temperature calibration is given in **Figure 4.2.6**.

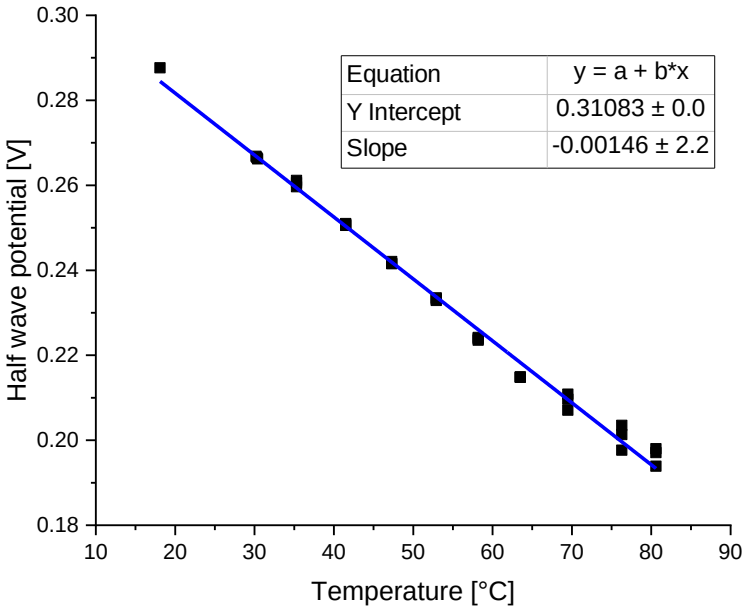

Figure 4.2.6: Temperature calibration obtained by recording CVs three times consecutively for each temperature investigated and plotting the respective half wave potentials. Measurements were performed after a constant temperature was established and conducted in an electrochemical cell connected to Peltier elements for temperature control. As working electrode, a 25 µm Pt disk electrode was utilized.

PACs were carried out using a UME with an electrode diameter of 25 µm and an RG value (ratio between total tip diameter and electroactive diameter) of 4. This value represents the ratio between the total probe tip diameter and the diameter of the electroactive area. Fabrication of probes was done according to a procedure described elsewhere [38]. The center of the flattened wire was approached in feedback mode in an unheated state until a current corresponding to 200% of the current measured in the bulk solution was obtained. The approach was then repeated as the wire was heated, travelling the same distance as was done in the PACs without heating. For approaches in feedback mode, a potential of 0.5 V was applied at the UME, while the substrate remained at OCP. In both SG/TC and competition mode, a substrate potential of 0.5 V was set, with a probe potential of 0.0 V and 0.5 V, respectively.

SECM images in feedback, SG/TC, and competition modes were recorded with and without heating. An area of 135×500 µm covering the wire was imaged at a tip-to-wire distance of 7 µm. Measurements were performed with 1.5 mM FcMeOH as redox mediator, with an E (Probe) and E (wire) of 0.5 V and OCP, respectively (feedback mode); and 0.0 V and 0.5 V, respectively (SG/TC mode); as well as 0.5 V for both tip and wire (competition mode). The pixel size was set to 10 µm with a probe velocity of 100 µm s^{-1}. Heating was applied 10 min prior to imaging, to ensure steady temperatures during measurements.

4.2.4. Conclusions

A new hot-wire electrochemistry setup suitable for SECM studies was developed and characterized. In contrast to cylindrical microwires used in conventional hot-wire electrochemistry, flattened microwires were implemented in a planar glass substrate, enabling a straightforward operation in SECM measurements.

The new setup was successfully characterized via CV and OCP measurements, as well as both PACs and images of the microwire substrate recorded in feedback, SG/TC, and competition modes of SECM. CVs revealed that mass transport between wires and bulk solution drastically increased with a higher wire temperature. In this context, the present hot-wire SECM configuration can be seen as a new option of hydrodynamic SECM. Fast changes of temperature could be carried out, shown by OCP monitoring. Finally, SECM images of the heated microwire exhibited higher contrast in comparison to images obtained at room temperature. The concept presented in this manuscript paves the way for a wide range of studies of temperature-dependent processes by means of SECM.

References

1. Flechsig G-U (2018) New electrode materials and devices for thermoelectrochemical studies and applications. Curr. Opin. Electrochem. 10:54–60
2. Cutress IJ, Marken F, Compton RG (2009) Microwave-Assisted Electroanalysis: A Review. Electroanalysis 21(2):113–123
3. Marken F, Sur UK, Coles BA, Compton RG (2006) Focused microwaves in electrochemical processes. Electrochim. Acta 51(11):2195–2203
4. Walter A, Langschwager F, Marken F, Flechsig G-U (2016) Nanostructured heated gold electrodes for DNA hybridization detection using enzyme labels. Sens. Actuator. B Chem. 233:502–509
5. Walter A, Surkus A-E, Flechsig G-U (2013) Hybridization detection of enzyme-labeled DNA at electrically heated electrodes. Anal. Bioanal. Chem. 405(11):3907–3911
6. Biala K, Sedova A, Flechsig G-U (2015) Sequence and Temperature Influence on Kinetics of DNA Strand Displacement at Gold Electrode Surfaces. ACS Appl. Mater. Interfaces 7(36):19948–19959
7. Pinyou P, Ruff A, Pöller S, Barwe S, Nebel M, Alburquerque NG, Wischerhoff E, Laschewsky A, Schmaderer S, Szeponik J, Plumeré N, Schuhmann W (2015) Thermoresponsive amperometric glucose biosensor. Biointerphases 11(1):11001

8. Lau C, Flechsig G-U, Gründler P, Wang J (2005) Electrochemistry of nicotinamide adenine dinucleotide (reduced) at heated platinum electrodes. Anal. Chim. Acta 554(1-2):74–78

9. Duwensee H, Vázquez-Alvarez T, Flechsig G-U, Wang J (2009) Thermally induced electrode protection against biofouling. Talanta 77(5):1757–1760

10. Ghanem MA, Thompson M, Compton RG, Coles BA, Harvey S, Parker KH, O'Hare D, Marken F (2006) Microwave induced jet boiling investigated via voltammetry at ring-disk microelectrodes. J. Phys. Chem. B 110(35):17589–17594

11. Boika A, Baranski AS (2011) Numerical simulations of phenomena observed at hot microelectrodes: Inlaid microdisk. Electrochim. Acta 56(21):7288–7297

12. Boika A, Baranski AS (2008) Dielectrophoretic and electrothermal effects at alternating current heated disk microelectrodes. Anal. Chem. 80(19):7392–7400

13. Gründler P, Kirbs A, Zerihun T (1996) Hot-wire electrodes: voltammetry above the boiling point. Analyst 121(12):1805–1810

14. Gründler P (2015) In-situ Thermoelectrochemistry. Springer Berlin Heidelberg, Berlin, Heidelberg, Germany

15. Gründler P, Flechsig G-U (1998) Deposition and stripping at heated microelectrodes. Arsenic(V) at a gold electrode. Electrochim. Acta 43(23):3451–3458

16. Flechsig G-U, Korbut O, Gründler P (2001) Investigation of Deposition and Stripping Phenomena at the Heated Gold Wire Electrode in Comparison to the Rotating Disk Electrode: Copper(II), Mercury(II), and Arsenic(III). Electroanalysis 13(8-9):786–788

17. Peter J, Reske T, Flechsig G-U (2007) Comparison of DNA Hybridization at Rotating and Heated Gold Disk Electrodes. Electroanalysis 19(13):1356–1361

18. Mathivanan J, Chang Z, Galagedera SKK, Flechsig G-U (2018) Thermoelectrochemistry of Paracetamol - Studied at Directly Heated Micro-wire and Rotating Disk Electrodes. Electroanalysis 30(7):1479–1486

19. Gründler P, Frank O, Kavan L, Dunsch L (2009) Carbon Nanotube Electrodes for Hot-Wire Electrochemistry. ChemPhysChem 10(3):559–563

20. Bard AJ, Mirkin MV (eds) (2012) Scanning electrochemical microscopy, 2. ed. CRC Press, Boca Raton, Fla

21. Polcari D, Dauphin-Ducharme P, Mauzeroll J (2016) Scanning Electrochemical Microscopy: A Comprehensive Review of Experimental Parameters from 1989 to 2015. Chem. Rev. 116(22):13234–13278

22. Bard AJ, Fan FRF, Kwak J, Lev O (1989) Scanning electrochemical microscopy. Introduction and principles. Anal. Chem. 61(2):132–138

23. Engstrom RC, Pharr CM (1989) Scanning electrochemical microscopy. Anal. Chem. 61(19):1099A-1104A

24. Jamali SS, Moulton SE, Tallman DE, Forsyth M, Weber J, Wallace GG (2014) Applications of scanning electrochemical microscopy (SECM) for local characterization of AZ31 surface during corrosion in a buffered media. Corros. Sci. 86:93–100

25. Nickchi T, Rostron P, Barsoum I, Alfantazi A (2019) Measurement of local galvanic surface corrosion using scanning electrochemical microscopy on ductile cast iron. J. Mater. Sci. 54(12):9213–9221

26. Payne NA, Stephens LI, Mauzeroll J (2017) The Application of SECM to Corrosion Research. Corrosion 73(12):759-780

27. Eckhard K, Chen X, Turcu F, Schuhmann W (2006) Redox competition mode of scanning electrochemical microscopy (RC-SECM) for visualisation of local catalytic activity. Phys. Chem. Chem. Phys. 8(45):5359

28. Iffelsberger C, Vatsyayan P, Matysik F-M (2017) Scanning Electrochemical Microscopy with Forced Convection Introduced by High-Precision Stirring. Anal. Chem. 89(3):1658–1664

29. Raith T, Wert S, Iffelsberger C, Matysik F-M (2018) Development and characterization of electrochemical flow cells for hydrodynamic scanning electrochemical microscopy. Monatsh. Chem. 149(9):1671–1677

30. Raith T, Iffelsberger C, Vatsyayan P, Matysik F-M (2019) Impacts of Forced Convection Generated via High Precision Stirring on Scanning Electrochemical Microscopy Experiments in Feedback Mode. Electroanalysis 31(2):273–281

31. Boika A, Zhao Z (2016) First principles of hot-tip scanning electrochemical microscopy: Differentiating substrates according to their thermal conductivities. Electrochem. Commun. 68:36–39

32. Zhao Z, Leonard KC, Boika A (2019) Hot-Tip Scanning Electrochemical Microscopy: Theory and Experiments Under Positive and Negative Feedback Conditions. Anal. Chem. 91(4):2970–2977

33. Clausmeyer J, Schäfer D, Nebel M, Schuhmann W (2015) Temperature-Induced Modulation of the Sample Position in Scanning Electrochemical Microscopy. ChemElectroChem 2(7):946–948

34. Schäfer D, Puschhof A, Schuhmann W (2013) Scanning electrochemical microscopy at variable temperatures. Phys. Chem. Chem. Phys. 15(14):5215–5223

35. Novev JK, Compton RG (2016) Convective heat transfer in a measurement cell for scanning electrochemical microscopy. Phys. Chem. Chem. Phys. 18(43):29836–29846

36. Sode A, Nebel M, Pinyou P, Schmaderer S, Szeponik J, Plumeré N, Schuhmann W (2013) Determination of Temperature Gradients with Micrometric Resolution by Local Open Circuit Potential Measurements at a Scanning Microelectrode. Electroanalysis 25(9):2084–2091

37. Zhang H, Xiao X, Su T, Gu X, Jin T, Du L, Tang J (2014) A novel thermocouple microelectrode for applications in SECM and variable temperature electrochemistry. Electrochem. Commun. 47:71–74

38. Vatsyayan P, Iffelsberger C, Mayorga-Martinez CC, Matysik F-M (2016) Imaging of localized enzymatic peroxidase activity over unbiased individual gold nanowires by scanning electrochemical microscopy. Anal. Methods 8(38):6847–6855

4.3. Development of a temperature-pulse enhanced electrochemical glucose biosensor and characterization of its stability via scanning electrochemical microscopy

Stefan Wert, Heiko Iken, Michael J. Schöning and Frank-Michael Matysik

Electroanalysis 33 (2021).

This chapter was published in the journal above and changed for reasons of uniformity. The changes herein consist of minor corrections, formatting, and the addition of the supporting information to the main text.

Abstract

Glucose oxidase (GOx) is an enzyme frequently used in glucose biosensors. As increased temperatures can enhance the performance of electrochemical sensors, we investigated the impact of temperature pulses on GOx that was drop-coated on flattened Pt microwires. The wires were heated by an alternating current. The sensitivity towards glucose and the temperature stability of GOx was investigated by amperometry. An up to 22-fold increase of sensitivity was observed. Spatially resolved enzyme activity changes were investigated via scanning electrochemical microscopy. The application of short (<100 ms) heat pulses was associated with less thermal inactivation of the immobilized GOx than long-term heating.

4.3.1. Introduction

Scanning electrochemical microscopy (SECM) is a scanning probe technique frequently used for the electrochemical characterization of surfaces and interfaces. Common application fields include corrosion research [1-3], biological studies with cells [4, 5], and enzymes [6, 7], as well as material characterization [8-10]. Among the various measuring modes of SECM, the generation/collection (G/C) mode suffers from limited reproducibility and contrast issues due to a growing diffusion layer at the generator electrode. Forced convection was introduced into the measurement cells by different means [11, 12], resulting in increased currents and reproducibility of images as stable diffusion layers can be established at the generator electrode. Furthermore, this also led to contrast improvement in feedback mode imaging of SECM due to an enhanced feedback cycle at conductive surfaces [13].

As elevated temperatures increase the molecular motion within solutions as well, another option to benefit from the effects of forced convection is employing heated substrates in SECM.

In a recent effort, our group presented a setup for the implementation of flattened Pt microwires as substrates that are heated by an alternating current (AC) according to the concept of “hot-wire electrochemistry” [14]. The latter originates from the work of Gründler and co-workers [15, 16], featuring a thin (<25 µm diameter) gold or platinum microwire employed as working electrode (WE), heated by an AC with a frequency ≥100 kHz. In addition to the AC heating circuit, voltammetric measurements can be performed simultaneously. So far, hot-wire electrochemistry was utilized in various studies, including the trace analysis of various elements [17, 18], or the behavior of DNA and RNA under temperature influence [19]. Moreover, it is the basis for techniques like temperature pulse voltammetry [20], enabling even the analysis of substances above the boiling point of the electrolyte, as short temperature pulses do not lead to boiling effects. Studies concerned with temperature and its effects on SECM have shown that higher temperatures increase the contrast between conductive and non-conductive surfaces [21]. To make use of this effect, Boika et al. have developed a setup termed “hot tip SECM”, integrating the technology behind hot-wire electrochemistry into the SECM probe resulting in increased thermal convection in the vicinity of the probe tip [22-24].

Electrochemistry in general is a useful tool for the analysis of enzymes, as their activity can be correlated to the electrochemical current originating from the consumption or generation of electroactive products. This principle led to the development of numerous biosensors [25], such as glucose biosensors using glucose dehydrogenase or glucose oxidase (GOx) to determine glucose concentrations. In order to enhance the performance characteristics of biosensors, efforts were made to increase enzyme stability and activity by immobilization techniques [26, 27], as they may affect optimal pH and temperature region of enzymes. In case of GOx, efforts were made to immobilize the enzyme and increase its stability at high temperatures. T.-F. Tseng et al. have immobilized GOx in a Nafion matrix [28], leading to increased stability and activity at high temperatures generated in the context of hot-wire electrochemistry. Especially, temperature pulses of 30 s duration showed a significant increase in GOx activity. Other groups have presented electrochemical GOx biosensors as well, e.g. using porous silica [29] or silica mesocellular foams [30] for immobilization.

For the in-depth analysis of enzymatic biosensors, SECM can be applied, especially as a tool in the development of miniaturized systems [31, 32]. Generally, the G/C modes and the redox competition mode enable the investigation of the kinetics at catalytically active sites of GOx substrates. In the G/C mode, a product from an enzymatic reaction can be collected at the SECM probe, while in the redox competition mode, the UME is set to a potential where it is competing with the enzyme in terms of educt consumption. Both modes have been applied for the characterization of GOx-based sensors [33-35]. A mediator-free technique measuring the impedance was reported as well [36].

In this work, the aim was to study the different impact of long-term vs. pulsed heating on the activity of GOx. We immobilized GOx on the surface of a flattened Pt microwire using a commercial enzyme spotter. The wire could be heated according to the hot-wire concept, leading to a temperature-adjustable glucose biosensor at which short temperature pulses were applied. The sensitivity of the sensor was studied for different glucose concentrations and pulse temperatures. A spatially resolved study of thermal deactivation of the enzyme caused by long-term heating and short temperature pulses was investigated using SECM. Images recorded in G/C mode before and after heating were used to reveal changes in GOx activity.

4.3.2. Experimental

4.3.2.1. Chemicals

All solutions were prepared using Milli-Q water (Milli-Q Advantage A10 system, Merck Millipore, Darmstadt, Germany). An aqueous 5/5 mM mixture of ferro/ferricyanide ($K_3Fe(CN)_6/K_4Fe(CN)_6$, Carl Roth GmbH + Co. KG, Karlsruhe, Germany) was used for temperature calibration and substrate characterization measurements. The following solutions were all prepared with phosphate buffer (pH 7) if not stated otherwise. The phosphate buffer was prepared using sodium dihydrogen phosphate monohydrate (Merck KGaA, Darmstadt, Germany) and di-sodium hydrogen phosphate dodecahydrate (Merck KGaA, Darmstadt, Germany). Feedback mode SECM imaging was carried out with 1.5 mM ferrocenemethanol (FcMeOH, 99%, ABCR, Karlsruhe, Germany). G/C mode SECM imaging was performed with 10 mM glucose (Merck KGaA, Darmstadt, Germany). A buffered (pH 7,4) GOx solution with 4 U mL^{-1} (Type X-S, 100,000-250,000 units/g, Merck KGaA, Darmstadt, Germany) was used for drop-coating.

4.3.2.2. Materials

A detailed description of the preparation of heated wire substrates for SECM studies is given elsewhere [14]. Pt wires of 25 µm diameter (Goodfellow GmbH, Hamburg, Germany) were used for the preparation of heatable electrodes used as the substrates and for the fabrication of UMEs for SECM imaging. For fixation of the flattened Pt wire, epoxy resin (Epoxydharz L, R&G Faserverbundstoffe GmbH, Waidenbuch, Germany) was employed. Microscope slides served as base for the substrates. Copper wires (0.5 mm inner diameter, 1.1 mm outer diameter, Pollin Electronic GmbH, Pförring, Germany) were soldered to the Pt wire to establish electrical contact to the substrates. Soldering joints were sealed by applying hot glue (Pattex, Henkel AG & Co. KGaA, Düsseldorf, Germany). The substrate used in this work had a resistance of 5.1 Ω.

For electrochemical measurements, a Pt wire of 0.5 mm diameter was used as counter electrode together with a Ag/AgCl/3 M KCl reference electrode. The potentials listed herein are referring to this system.

4.3.2.3. Instruments

All experiments were carried out with a SECM 920C (CH Instruments, Austin, Texas, USA) equipped with a 25 µm diameter Pt ultramicroelectrode (UME) with an RG value (ratio between total tip diameter and platinum disk diameter) of 2, which was fabricated according to a procedure described elsewhere [37]. Heating during temperature calibration was realized by applying an external current with a direct current power source (Voltcraft HPS-13015, Conrad Electronic AG, Wollerau, Switzerland) to Peltier elements (KIMILAR, TEC1-12706), which were attached to the measurement cell. Drop-coating of GOx was performed with a sciFlexArrayer S3 (Scienion, Berlin, Germany). Heating of substrates was achieved with a laboratory-built AC source already used in a previous study [14] and fabricated according to [38]. The AC source consisted of a radio frequency generator and a transformer, yielding a 100 kHz AC. The special electronic configuration [38] allowed the simultaneous recording of amperometric signals.

4.3.2.4. Temperature calibration

In order to apply heating of defined temperature, a temperature calibration was carried out with a 25 µm diameter UME as working electrode in a solution of 5/5 mM ferro/ferricyanide and 1 M KCl. The electrochemical cell was held at constant temperatures of 15.6, 20.7, 29.0, 35.3, 46.3, and 55.4 °C. When the temperature remained constant for 1 min, the open circuit potential (OCP) was measured for a duration of 200 s with a sampling rate of 0.1 s, and the values during the last 100 s were averaged. To prevent a temperature-induced potential shift of the reference electrode potential, the reference electrode was connected to the measurement cell via a capillary-based salt bridge. This method for temperature determination was previously applied in other studies and was found to be applicable for short temperature pulses [15, 20]. It has to be noted that temperature determinations based on OCP measurements show limited accuracy in case of very short heating pulses due to the kinetics of OCP equilibration. However, in the present case it is considered as an appropriate method for temperature determinations [15, 20]. Furthermore, only the temperature of the wire surface can be determined but not the temperature of the surroundings (within the enzyme layer), making overall temperature estimations in all relevant regions of the sensing device impossible.

4.3.2.5. Pulse characterization

All of the following experiments were executed with the setup illustrated in **Figure 4.3.1A**. The UME for localized activity investigations was connected to working electrode channel 1 (WE1). Working electrode channel 2 (WE2) was used to record the amperometric current at the substrate electrode. In addition, the substrate (separately shown in **Figure 4.3.1B**) was connected to the AC generator for in situ heating. The electrochemical setup was completed with counter and reference electrodes.

For the determination of the temperatures reached during heat pulses, the OCP was measured over time while applying 1/5/10/50/100 ms heat pulses with an idle time of 5 s after every pulse. Starting from 30 mA, the heating current was increased by 30 mA with every pulse, up to a magnitude of 600 mA. Data was acquired with a sampling rate of 1 ms. This procedure was performed three times for each pulse duration, and the shift of OCP was converted to temperature values according to the temperature calibration. A solution of 5/5 mM ferro/ferricyanide and 1 M KCl was used for this set of experiments.

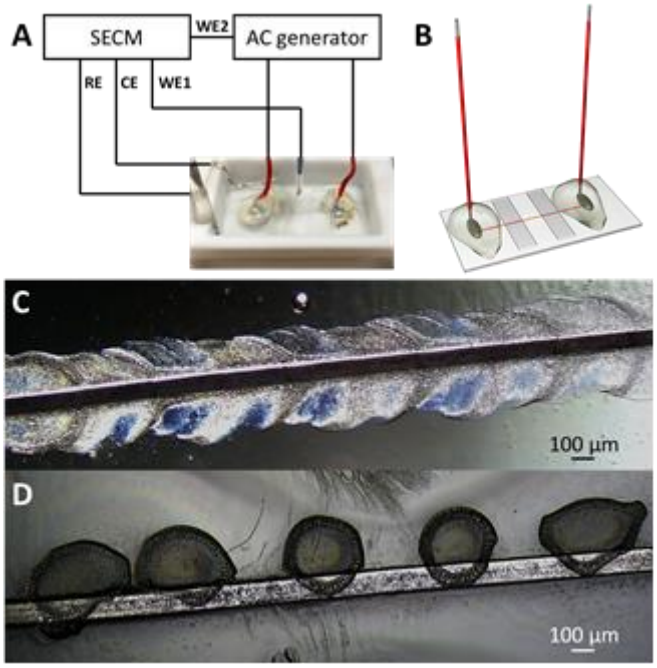

Figure 4.3.1A: Schematic experimental setup. Working electrode 1 channel (WE1) of the SECM was used for probe control. Working electrode 2 channel (WE2) was connected to the heatable substrate with an AC generator interconnected to enable AC heating. **B:** Illustration of the substrate with a flattened Pt wire as heatable electrode. Two additional glass slides were placed on top of the wire for means of mechanical stabilization (grey stripes). **C/D:** Micrographs of glucose oxidase covering the entire wire of the substrate (**C**) and applied as spots via drop-coating (**D**).

To optimize the idle time between pulses applied in later experiments, the impact of idle time on the amperometric response was investigated. The same pulse sequence as before was

applied to the substrate with idle times of 3, 5 and 8 s while performing chronoamperometry. A potential of 0.5 V was applied to induce mediator oxidation.

4.3.2.6. Temperature-pulsed GOx biosensor

As GOx is frequently used for sensing glucose in biosensors, we investigated the impact of pulsed heating on the electrochemical response and the stability of the enzyme. In a first set of experiments, 5 µL of GOx solution were dispersed over the substrate, ensuring that the entire wire is covered with solution as shown in **Figure 4.3.1C**. After the solution dried, the substrate was placed in the electrochemical cell filled with 5 mL of phosphate buffer (pH 7). Chronoamperometry with a substrate potential of 0.8 V was then conducted while the glucose concentration inside the cell was raised stepwise. The concentration was increased by steps of 0.1 mM by the addition of 50 µL of 1 M glucose, up to a final concentration of 1.0 mM to cover a concentration range suitable for fundamental studies. After each addition, the solution was mixed, and as soon as a steady-state current was observed, 7 heat pulses of 100 ms duration with 8 s idle time were applied to the substrate. The experiment was repeated with different pulse temperatures, applying pulses that led to wire temperatures of 24, 34, 53, 65, 72, 79, and 106 °C. For each temperature, the GOx coating was renewed by cleaning the substrate with isopropanol and water, followed by reapplication of GOx solution when the substrate had dried.

Furthermore, the impact of long-term heating vs. short temperature pulses on the local GOx activity was studied. For these experiments, GOx was applied to the wire by drop-coating, resulting in a pattern as shown in **Figure 4.3.1D**. For each GOx spot, 20 drops with a drop volume of 319 pL were applied. The localized activity at these GOx spots was investigated by recording SECM images in feedback and G/C modes. In an area containing both bare wire and enzyme spot, SECM images covering 400×500 µm with a pixel size of 10 µm and a scan rate of 50 µm s^{-1} were recorded. Feedback mode imaging in 1.5 mM FcMeOH was performed to locate the position of the Pt wire, while in G/C mode imaging, formed H_2O_2 in 10 mM Glucose indicated the position and activity of GOx spots. When switching measurement modes, the cell was flushed 3 times with phosphate buffer before adding the new solution. In G/C mode, the H_2O_2 generated by GOx during glucose conversion was oxidized at the SECM tip at a potential of 0.8 V as an indicator for GOx activity. Afterwards, the wire was either heated for 30 s at 42 °C or a short heat pulse (100 ms, 106 °C) was applied. To investigate localized activity changes, another G/C SECM image was recorded with the same parameters as before.

4.3.3. Results and discussion

4.3.3.1. Pulse characterization

The temperature reached during 100 ms heat pulses was investigated by measuring the OCP over time due to its temperature dependence. **Figure 4.3.2A** shows the OCP measured at an uncoated substrate for the application of 20 heat pulses of 30 to 600 mA heat current. The heat intensity increased by 30 mA with every pulse. When no heat was applied, an OCP of 0.285 V was measured. Heat pulses of 30 mA resulted in a negligible change in OCP. With elevating pulse intensity, higher OCP differences were observed, increasing exponentially up to a heating current of 300 mA. After that, a linear increase of the OCP shift was observed, as well as a slight baseline shift towards lower potentials. The latter was assumed to happen due to the glass around the wire being heated by the pulses, keeping the wire slightly above the initial temperature between the pulses.

In **Figure 4.3.2B**, the OCP differences from 3 measurements were averaged and converted to temperature values according to the temperature calibration given in **Figure 4.3.3**. The pulses led to reproducible temperatures when heating currents of up to 360 mA were applied. For stronger pulses, standard deviations of up to ±4 °C (n = 3) were obtained. For the highest heating intensity of 600 mA, a temperature of 106 °C could be reached. Temperatures beyond the boiling point are possible since the bubble formation associated with the boiling process is kinetically delayed. Even higher temperatures should be possible, as temperatures up to 250 °C were reported [39]. We also studied the temperatures reached with shorter heat pulses of 1, 5, 10, and 50 ms duration. The results are shown in **Figure 4.3.4**. A similar trend in temperature increase was observed, but shorter pulses resulted in lower temperatures. For very short pulses of 1 ms, the temperature determination was inaccurate as the sampling rate during OCP measurements was 1 ms. Nevertheless, we decided to apply 100 ms pulses in the forthcoming experiments in order to reach the highest possible temperature.

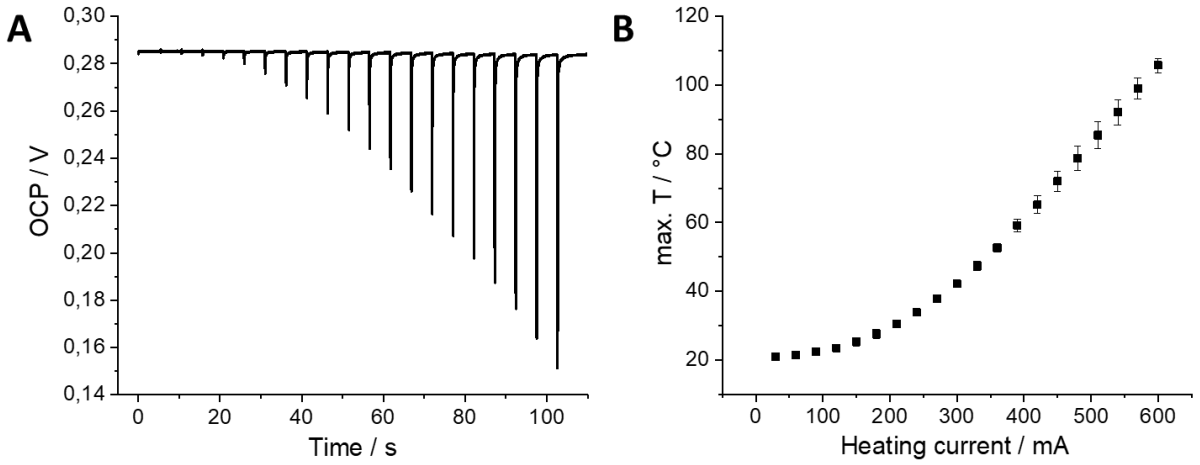

Figure 4.3.2A: Open circuit potential measurement over time while applying 100 ms heat pulses of increasing intensity to the substrate. Heating current increased by 30 mA steps from 30 to 600 mA. The time between each pulse was 5 s. **B:** Corresponding temperature for every heat pulse applied. The temperature was determined 3 times for all heating intensities.

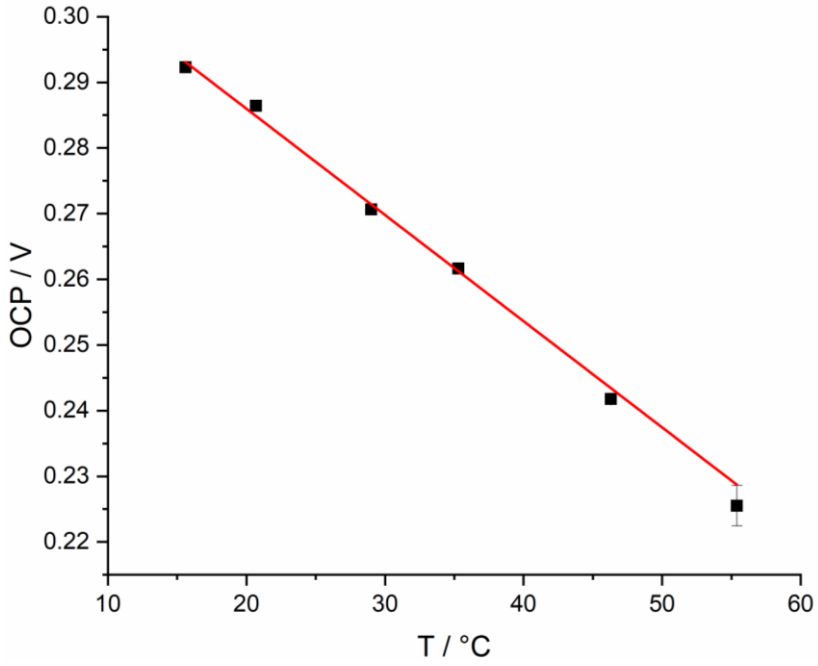

Figure 4.3.3: Temperature calibration correlating open circuit potential (OCP) with temperature (T). The potential at a 25 µm Pt disk UME was measured vs. a Ag/AgCl/3 M reference electrode. The measurements were performed in a solution of 5/5 mM ferro/ferricyanide in 1 M KCl. The OCP at a fixed temperature was measured over 200 s, and the values during the last 100 s were averaged.

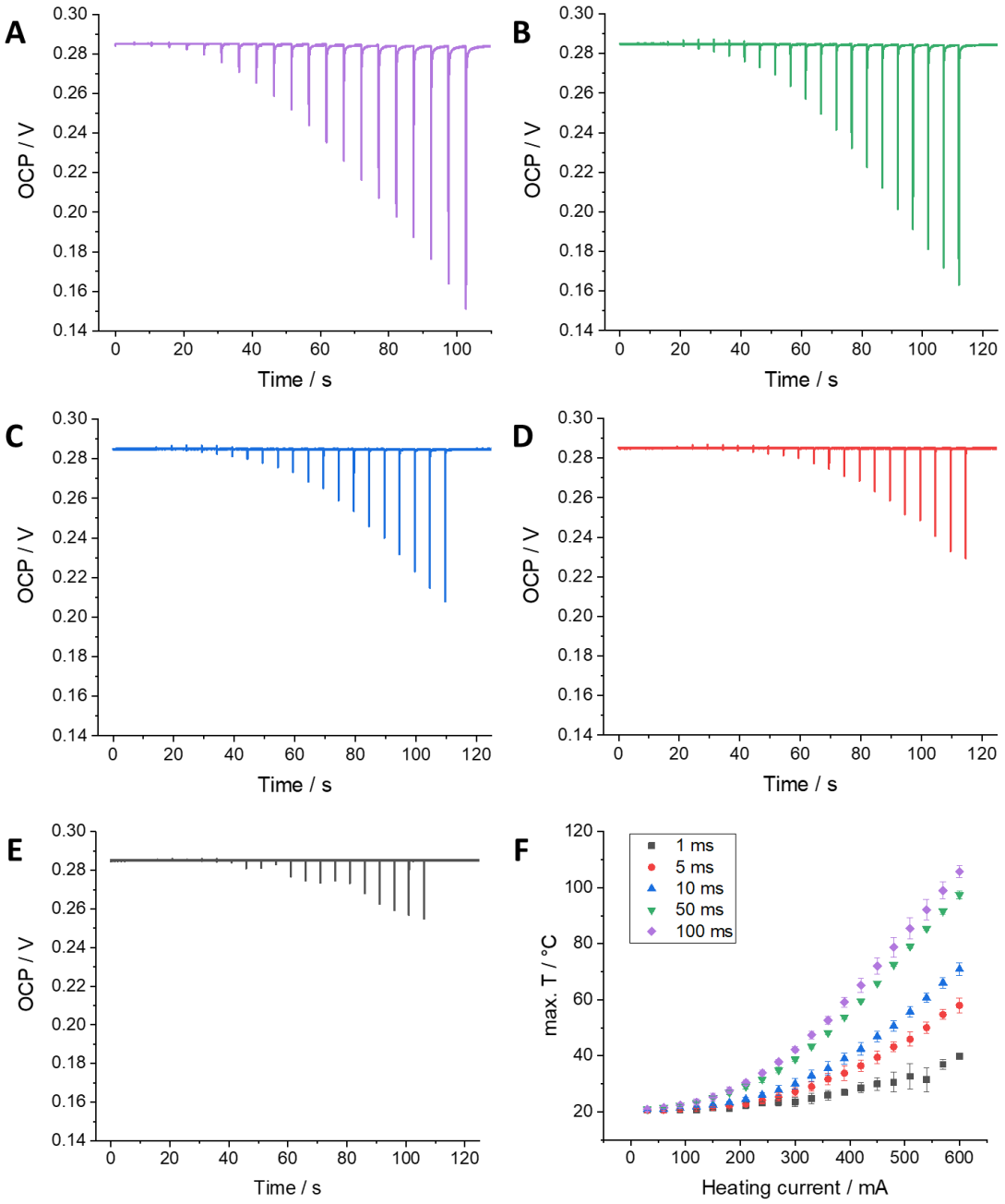

Figure 4.3.4: Open circuit potential measurement over time in a solution of 5/5 mM ferro/ferricyanide and 1 M KCl while applying 100/50/10/5/1 ms (**A-E**) heat pulses of increasing intensity to the substrate. Heating current increased by 30 mA steps from 30 to 600 mA. The time between each pulse was 5 s. **F:** Corresponding temperature for every heat pulse applied. The temperature was determined 3 times for every heating intensity.

Furthermore, to optimize the idle time for the upcoming amperometric experiments, pulses of increasing intensity with idle times of 3, 5 and 8 s were applied while performing chronoamperometry. Short idle times led to an increased current between pulses, as shown in **Figure 4.3.5**. Therefore, an idle time of 8 s was chosen for the next measurements.

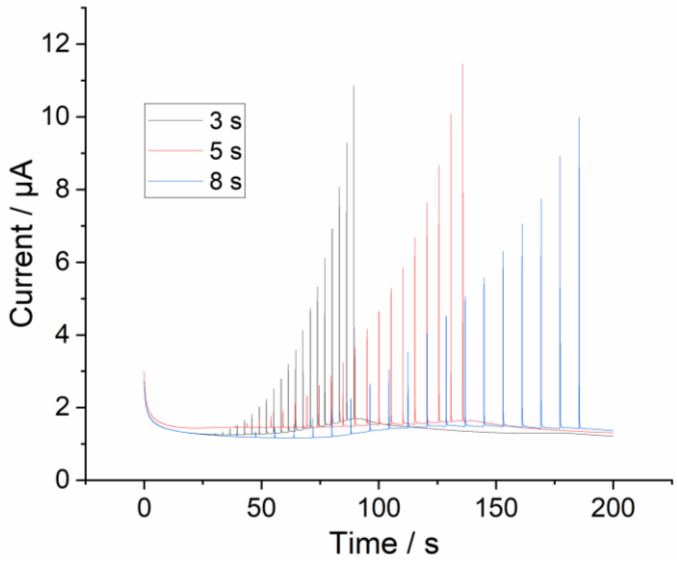

Figure 4.3.5: Chronoamperometry measurements while applying 100 ms heat pulses of increasing intensity to the substrate. Heating current increased by 30 mA steps from 30 to 600 mA. The time between each pulse was 3/5/8 s (black/red/blue). E = 0.5 V. Experiments were performed using 5/5 mM ferro/ferricyanide in 1 M KCl.

4.3.3.2. Temperature-pulsed biosensor

The impact of temperature pulses on the activity of GOx used in a biosensor was investigated. The amperometric current from the oxidation of H_2O_2 was measured at different glucose concentrations in addition to temperature pulses applied for every glucose concentration. **Figure 4.3.6A-C** show chronoamperometric experiments where the glucose concentration was increased by increments of 0.1 mM from 0.1 to 1.0 mM and heat pulses were applied to the substrate leading to short increases of the wire temperature to 24, 65 and 106 °C. After each glucose addition, the solution was mixed (visible as a noisy current increase) and 7 heat pulses were applied when a constant current had established.

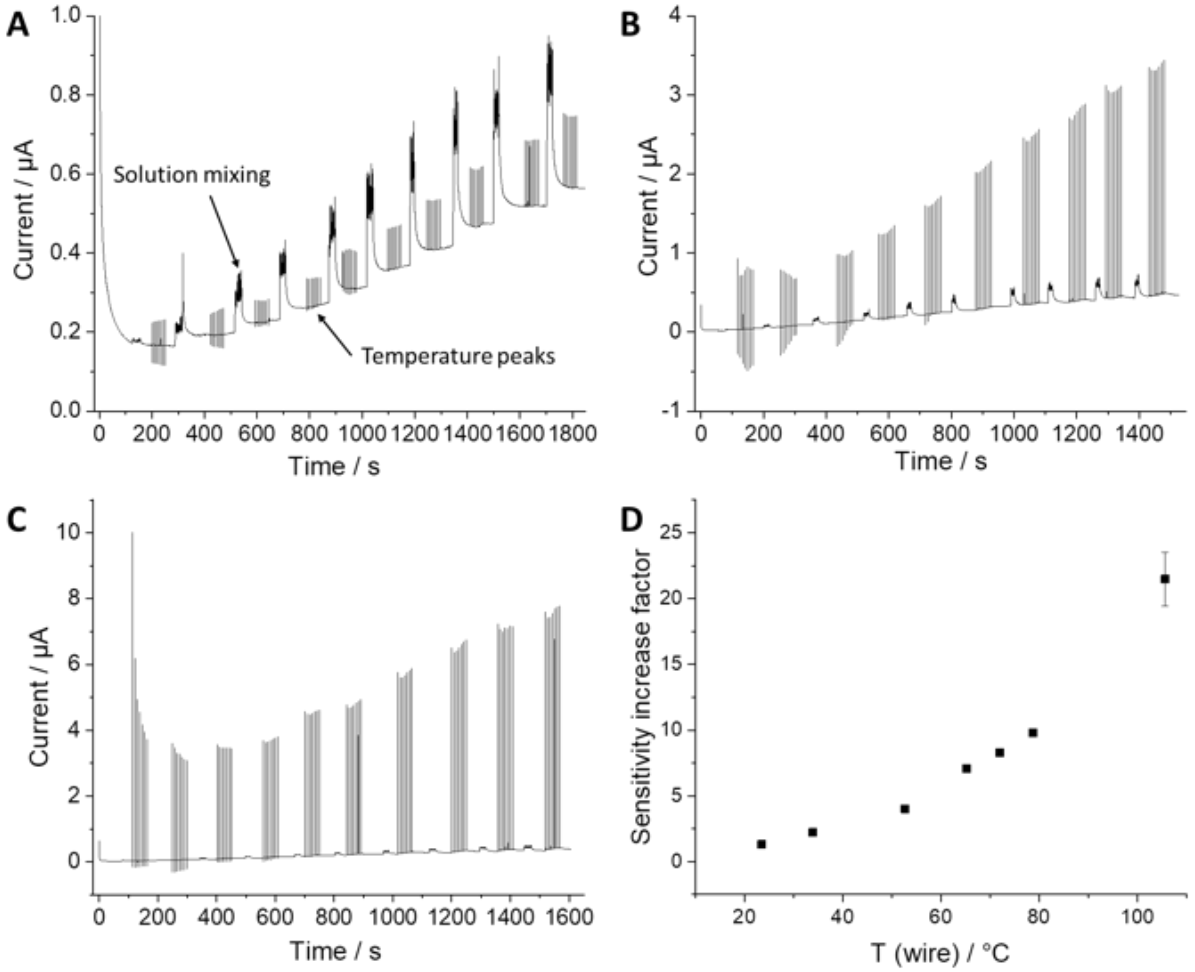

Figure 4.3.6A-C: Chronoamperometric measurements with a GOx-coated substrate. The wire of the substrate was coated entirely by application of 5 µL of GOx solution. Glucose concentration was increased stepwise (0.1 mM steps) from 0.1 to 1.0 mM. When a steady-state current was measured, 7 heat pulses of 100 ms duration and 8 s pulse pause were applied to the substrate. This was conducted for every concentration step with pulses leading to wire temperatures of 24 (**A**), 65 (**B**) and 106 °C (**C**). **D:** Sensitivity increase factor determined for different wire temperatures. The factor is given by the ratio of peak currents vs. currents measured 0.5 s prior to heat application.

In the first 4-5 sets of peaks, artifacts frequently occurred, leading to the current peaking in both positive and negative direction. The origin of this effect is unknown but happens to disappear at concentrations higher than 0.5 mM. At glucose concentrations ≥0.5 mM, the increase of current appeared to be linear for all temperatures investigated as shown in **Figure 4.3.7**. In **Figure 4.3.6A**, the temperature pulses led to a temperature increase from 20 °C to 24 °C. This resulted in small current increases ranging from 50 to 200 nA, with stronger increases observable at higher glucose concentrations. At 65 °C in **Figure 4.3.6B**, the current increase was significantly higher compared to **Figure 4.3.6A**, with a current increase between 0.5 to 3 µA, proportional to the glucose concentration. With peak temperatures of 106 °C, the current during the very first pulse was initially very high at 10 µA but continued to decrease down to 3 µA for the last pulse at 0.2 mM glucose concentration. Afterwards, the peak current

increased with glucose concentration up to a value of 7.5 µA. The initial decrease might be caused by enzyme degradation in close vicinity to the heated wire due to the very high temperature, but a certain amount of GOx remained active since the current kept increasing over time with the glucose additions. It should be noted that the increased currents measured are the result of both increased GOx activity and enhanced conversion of H_2O_2 at the electrode, both resulting from higher temperatures. The single effects were previously investigated in a study carried out by T.-F. Tseng et al. [28], where a similar set of experiments was conducted, but an additional chronoamperometric measurement in H_2O_2 solution was performed to separately study the effect of temperature on the H_2O_2 conversion at the electrode.

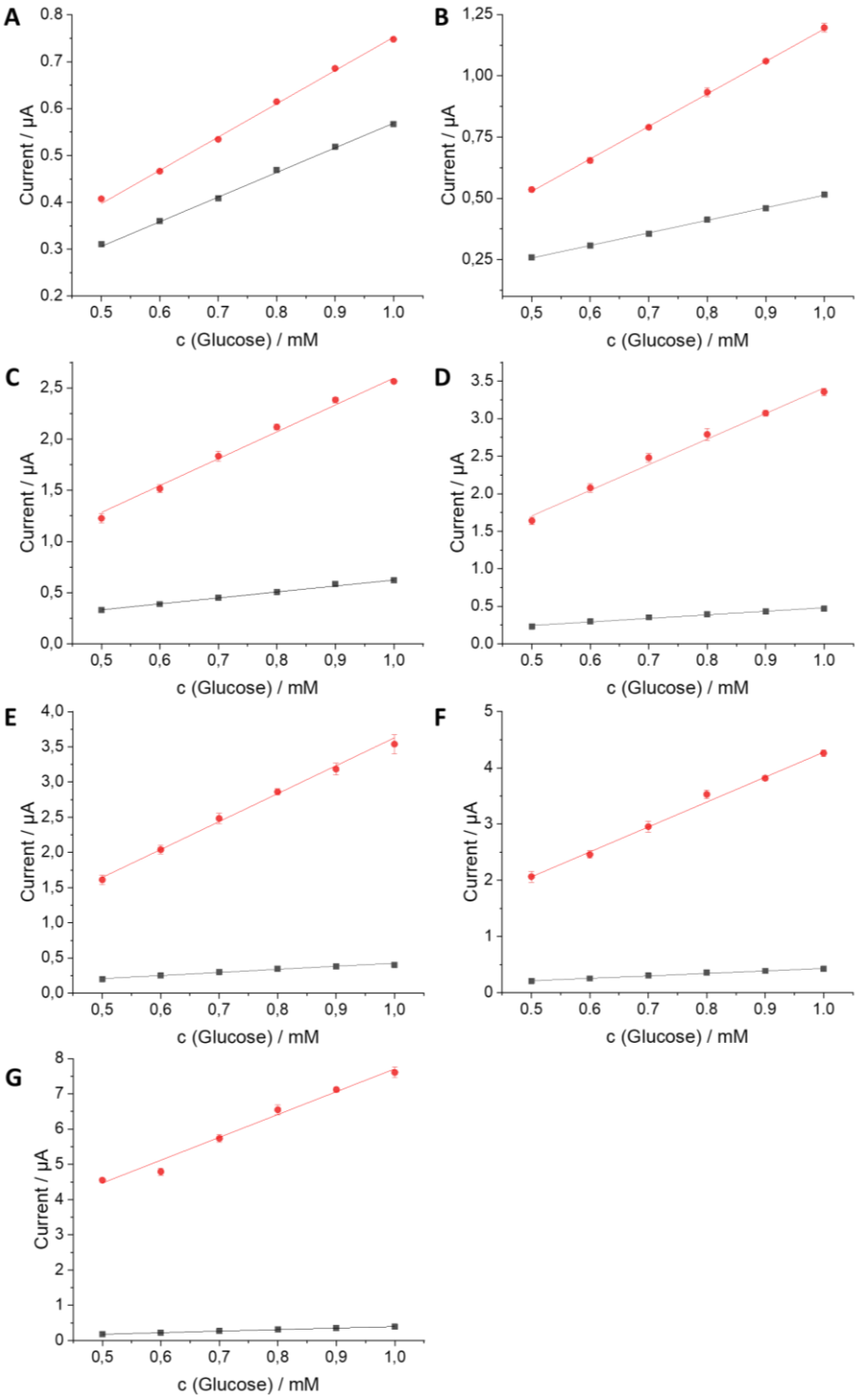

Figure 4.3.7: Peak currents (red) and currents measured between pulses (black) for different glucose concentrations and pulse temperatures of 24 (**A**), 34 (**B**), 53 (**C**), 65 (**D**), 72 (**E**), 79 (**F**), and 106 °C (**G**).

To determine the increase of sensitivity, the ratio between peak current and the current measured 0.5 s prior to the heat pulse was used. Due to the linear increase of response, pulses applied at glucose concentrations between 0.5 and 1.0 mM were considered for the sensitivity determination. The ratios, termed “sensitivity increase factor” herein, for all investigated temperatures are given in **Figure 4.3.6D**. The remaining chronoamperometric measurements for temperatures, which are not included in **Figure 4.3.6A-C** (34, 53, 72, and 79 °C), are

depicted in **Figure 4.3.8**. Generally, with stronger heat pulses, a higher sensitivity could be achieved. Up to temperatures of 79 °C, the sensitivity remained highly reproducible with an increase factor of up to 10. For 106 °C, the current response increased 22-fold but with a high uncertainty of ±2. The reason for this error can be seen in **Figure 4.3.9**, where the signal increase factors are given for every glucose concentration and temperature. It is shown that for 106 °C, the sensitivity decreased with higher glucose concentrations. This could be attributed to thermal inactivation of the enzyme due to the high intensity and increasing number of heat pulses applied to the substrate, as together with the stepwise concentration increase, more pulses were applied to the substrate in total. This observation is also in line with the decrease of currents during the first pulses in **Figure 4.3.6C**. In summary, temperature pulses of up to 79 °C were applicable to the substrate without noticeably damaging the GOx coating. In a similar study, T.-F. Tseng et al. [28] achieved a 24-fold increase of sensitivity when applying 68 °C for 30 s. This might be attributed to different immobilization protocols for GOx. In ref. [28], GOx was embedded in a Nafion membrane. However, our results show that higher temperatures can be applied when the pulse duration is decreased.

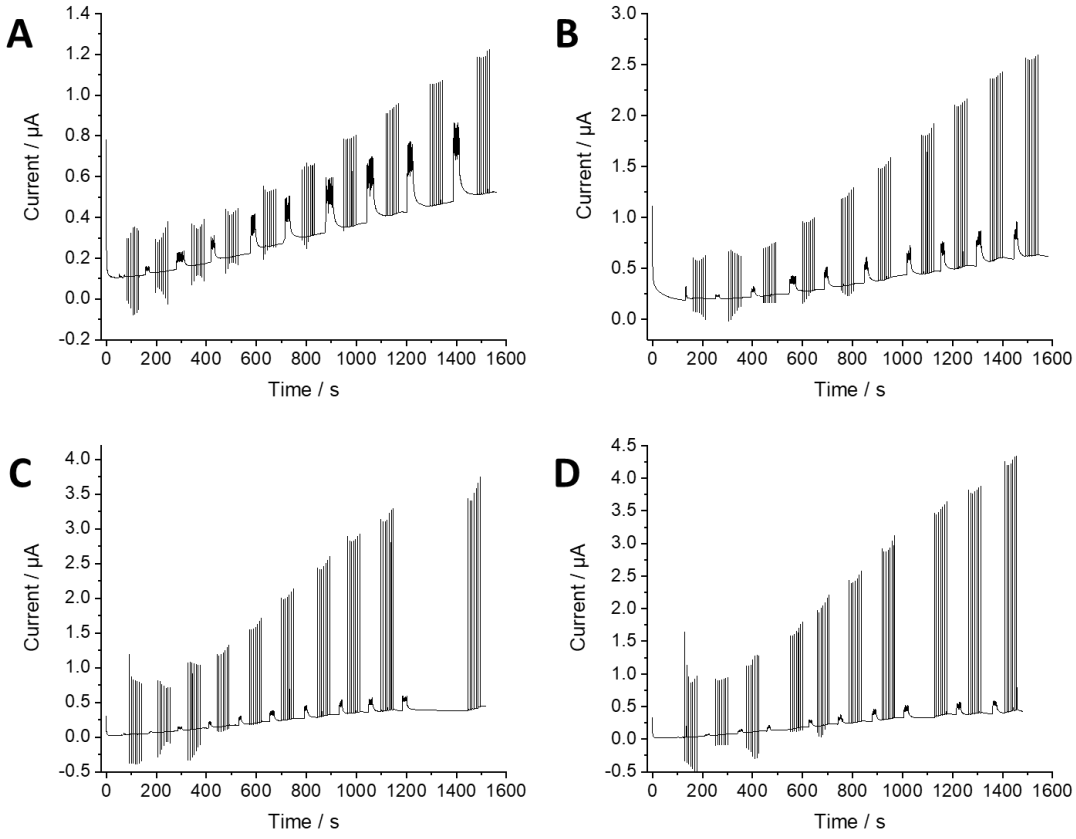

Figure 4.3.8: Chronoamperometric measurement with a GOx-coated substrate. Glucose concentration was increased stepwise (0.1 mM steps) from 0.1 to 1.0 mM. When a steady-state current was measured, 7 heat pulses of 100 ms duration and 8 s pulse pause were applied to the substrate. This was conducted for every concentration step with pulses leading to peak wire temperatures of 34 (**A**), 53 (**B**), 72 (**C**) and 79 °C (**D**).

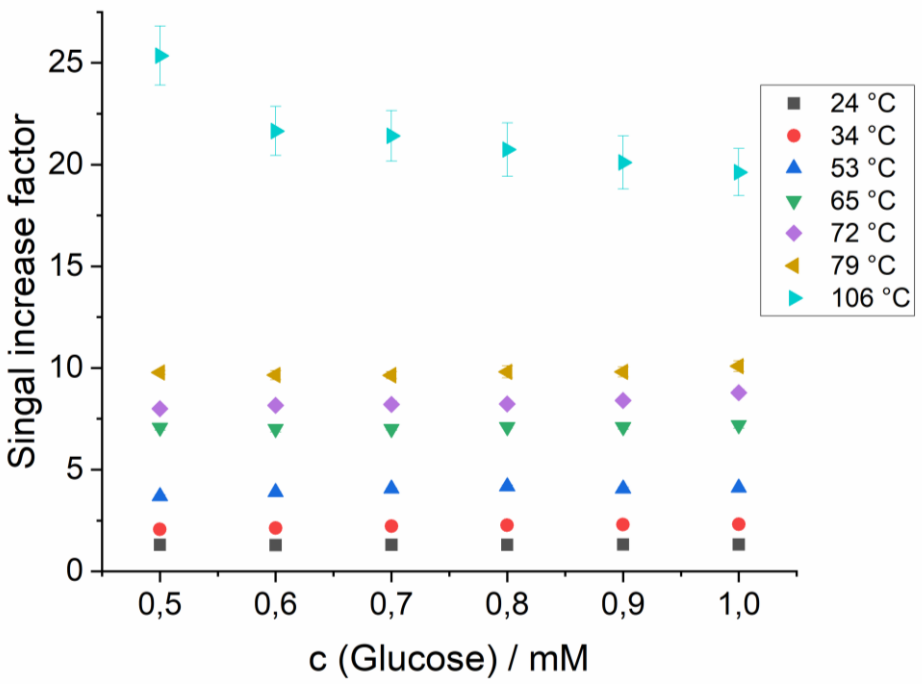

Figure 4.3.9: Sensitivity increase factor obtained for different glucose concentrations and heating peaks of various temperatures. Each point was derived from n = 7 heat pulses.

The localized activity changes of GOx spots upon heat application was studied by means of SECM. Moreover, the impact of long-term heating for 30 s was compared to the application of a single 100 ms heat pulse. First, a spot on the wire was located by using both feedback mode imaging in FcMeOH and G/C mode imaging in glucose solution. The feedback mode allowed distinguishing the wire from the surrounding substrate due to conductivity differences. The G/C mode showed the location of the GOx since it produced H_2O_2 as electroactive species that was collected at the probe. **Figure 4.3.10A** and **B** show the feedback and G/C mode SECM images of the wire and the enzyme spot, respectively. In the feedback image, the wire is visible as a band of elevated current with a width of 100 µm as its high conductivity results in an elevated response. The G/C image shows an increased current at the location of the wire. The current to the right of the wire is higher than to its left, indicating that most of the enzyme is located on the right side. GOx is also immobilized directly on the wire, shown by higher currents measured in its middle part. At the edge of the wire, lower currents were measured, probably due to an inhomogeneous enzyme distribution within the drop-coated spot. Overall, the shape and size of the enzyme spot correlates well with the microscopic image in **Figure 4.3.1D**. In **Figure 4.3.10C**, another G/C image is depicted, which was recorded after applying a wire temperature of 42 °C for a period of 30 s to visualize the consequences of long-term heat application. Compared to the previous G/C image, the orange area corresponding to high currents considerably decreased in size. Most notably, no increased currents were measured directly at the wire, indicating that most of the GOx activity was lost close to the wire due to a

temperature gradient within the entire substrate, with the highest temperature at the wire surface.

Figure 4.3.10D shows extracted lines from both G/C images for better visualization of the consequences of continuous heating. Line B shows a current plateau corresponding to the high GOx activity directly on the wire. Further to the right, another current peak occurred which is in the center of the enzyme spot. After heat application, the current decreased along most of the extracted line as shown in line C. The most significant drop in the collector current signal occurred directly at the wire, which was most likely caused by a temperature gradient, as the highest temperatures were present directly at the wire. In addition, the thermal convection that resulted from heating possibly had a stirring effect inside the measurement cell. As a result, the H_2O_2, previously accumulated close to the GOx where it was generated, was spread throughout the solution. Afterwards, less H_2O_2 was produced by the GOx due to the damage from heating, and lower currents were measured.

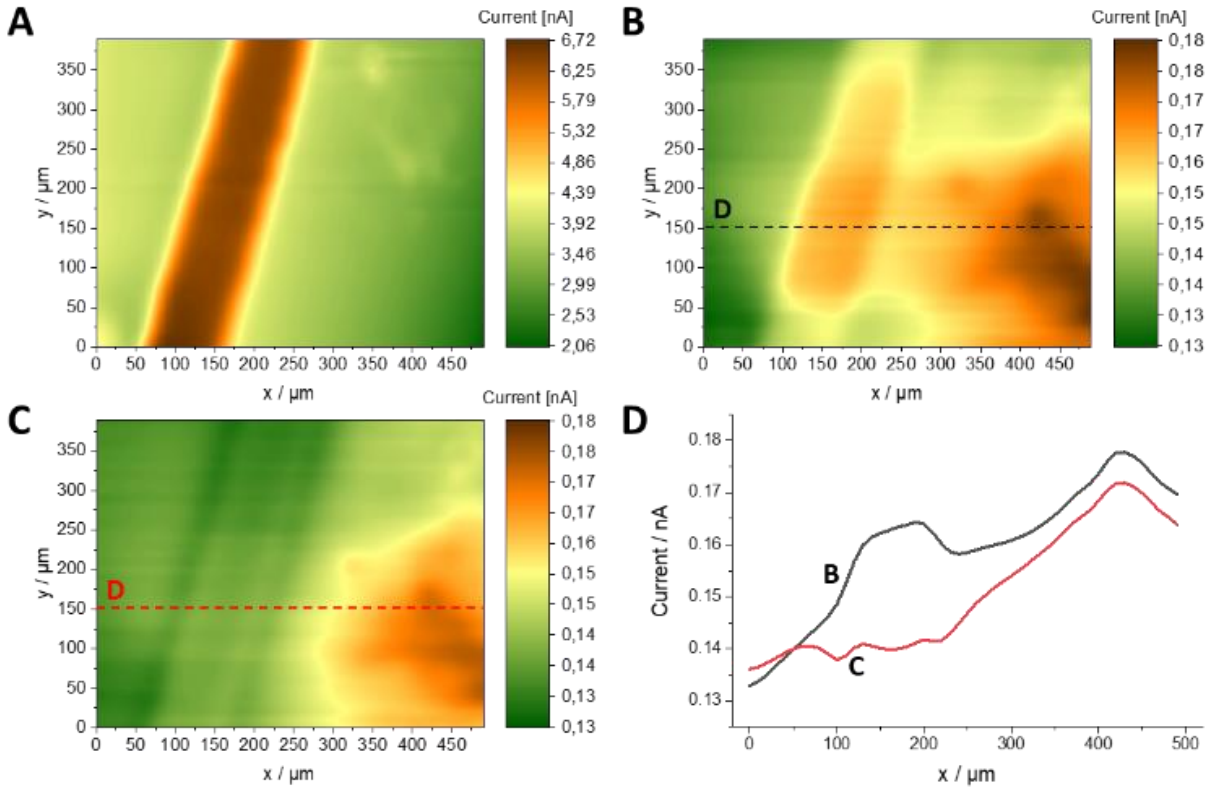

Figure 4.3.10: SECM images at the Pt wire of the substrate where a spot of GOx was applied. **A:** Feedback mode image in 1.5 mM FcMeOH. **B/C:** G/C images recorded in 10 mM glucose prior to heating (**B**) and after applying 42 °C for 30 s at the substrate (**C**). Lines within both images have been extracted and are compared in **D**. An area covering 400×500 µm was investigated. Pixel size: 10 µm. Wire-to-tip distance: 14 µm. E (Probe) = 0.5 V (**A**), 0.8 V (**B-D**).

For comparison, the impact of pulsed heating on GOx activity was studied as well. **Figure 4.3.11** shows SECM images of another enzyme spot on a newly prepared substrate. This time however, a single 100 ms heat pulse with a maximum temperature of 106 °C was applied to

the substrate. **Figure 4.3.11A** and **B** show the feedback and G/C images obtained at a GOx spot on the Pt wire. Similar to **Figure 4.3.10B**, elevated currents recorded above and to the right of the wire indicate the presence of a GOx spot. After application of the heat pulse, overall higher currents were measured as shown in **Figure 4.3.11C**. Therefore, the entire GOx spot was still active in terms of producing H_2O_2 to a certain degree. The extracted lines from both G/C images given in **Figure 4.3.11D** confirm that observation. However, the comparison of the lines shows that the current increase was lower above the wire in contrast to the remaining substrate. This indicates that the enzyme in close contact with the wire showed reduced activity, but to a less severe extent compared to the case of continuous heating. We assume that this is a result of different temperature gradients for the respective cases. In the works of Gründler [38], it was simulated that 20 ms pulses with a heating current of 725 mA led to a temperature gradient of a thickness of more than 100 µm. Under the present experimental conditions, the area around the wire that seemed affected by the heat pulse (600 mA, 100 ms) was of similar size. Therefore, we expect the temperature gradient to be of comparable size in our case.

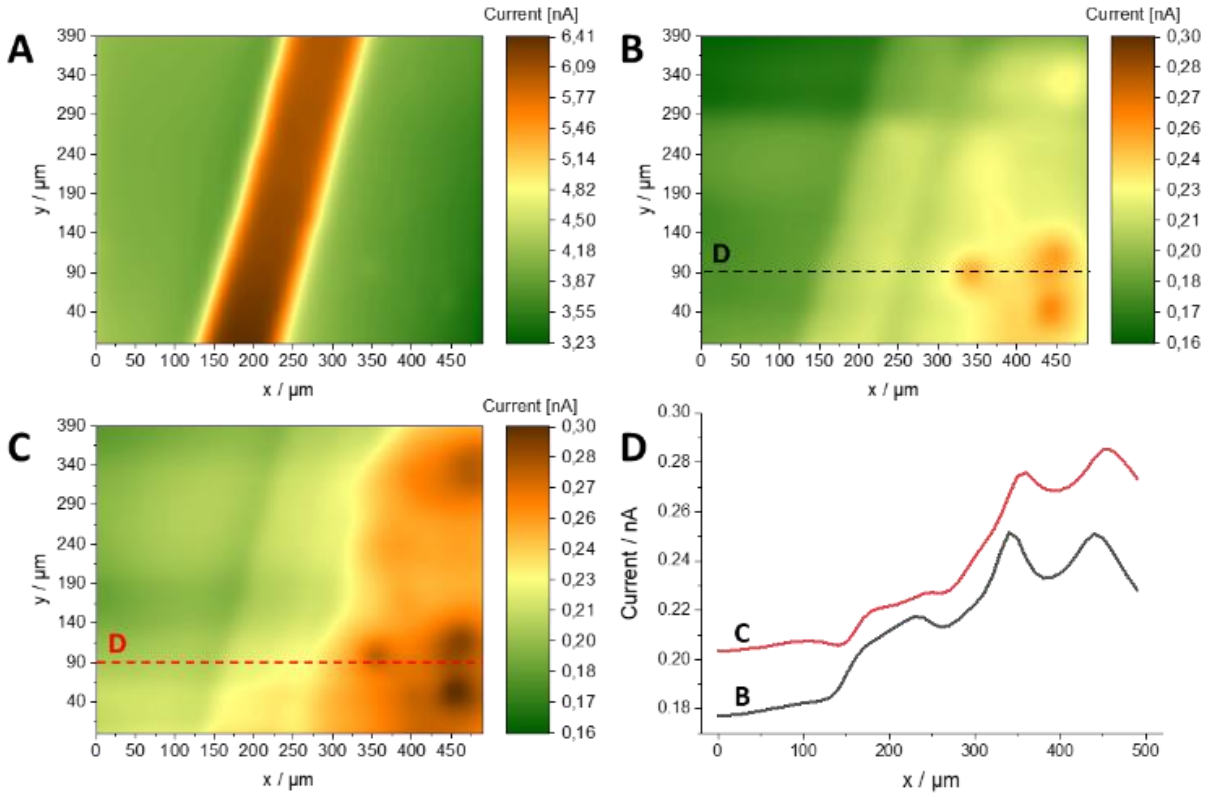

Figure 4.3.11: SECM images at the Pt wire of the substrate where a spot of GOx was applied. **A:** Feedback mode image in 1.5 mM FcMeOH. **B/C:** G/C images recorded in 10 mM glucose prior to heating (**B**) and after applying a heat pulse of 100 ms duration with a peak temperature of 106 °C to the substrate (**C**). Lines within both images have been extracted and are compared in **D**. An area covering 400×500 µm was investigated. Pixel size: 10 µm. Wire-to-tip distance: 14 µm. E (Probe) = 0.5 V (**A**), 0.8 V (**B-D**).

4.3.4. Conclusion

We investigated the sensitivity towards glucose and the extent of thermal deactivation of GOx under the influence of temperature pulses. Pulses of 106 °C led to an up to 22-fold increase of sensitivity towards glucose, however decreasing with the number of repeated pulses applied indicating effects of thermal deactivation. With a pulse temperature of 79 °C, signals were enhanced by a factor of 10 without a decrease of GOx activity. Furthermore, the spatially resolved thermal deactivation was investigated using SECM. G/C mode images of the enzyme immobilized on the wire showed that 106 °C applied for 100 ms led to a lower degree of thermal deactivation compared to 42 °C applied for 30 s. Overall, these results show that the sensitivity of glucose biosensors can be further increased by the application of very short temperature pulses and decreasing the pulse duration allows to apply higher temperatures as the extent of enzyme degradation decreases.

References

1. Payne NA, Stephens LI, Mauzeroll J (2017) The Application of Scanning Electrochemical Microscopy to Corrosion Research. Corrosion 73(7):759–780
2. Nickchi T, Rostron P, Barsoum I, Alfantazi A (2019) Measurement of local galvanic surface corrosion using scanning electrochemical microscopy on ductile cast iron. J. Mater. Sci. 54(12):9213–9221
3. Asserghine A, Medvidović-Kosanović M, Stanković A, Nagy L, Souto RM, Nagy G (2020) A scanning electrochemical microscopy characterization of the localized corrosion reactions occurring on nitinol in saline solution after anodic polarization. Sens. Actuators B Chem. 321:128610
4. Bergner S, Vatsyayan P, Matysik F-M (2013) Recent advances in high resolution scanning electrochemical microscopy of living cells – A review. Anal. Chim. Acta 775:1–13
6. Wittstock G (2001) Modification and characterization of artificially patterned enzymatically active surfaces by scanning electrochemical microscopy. Fresenius J. Anal. Chem. 370(4):303–315
7. Walter A, Surkus A-E, Flechsig G-U (2013) Hybridization detection of enzyme-labeled DNA at electrically heated electrodes. Anal. Bioanal. Chem. 405(11):3907–3911

8. Ryl J, Burczyk L, Zielinski A, Ficek M, Franczak A, Bogdanowicz R, Darowicki K (2019) Heterogeneous oxidation of highly boron-doped diamond electrodes and its influence on the surface distribution of electrochemical activity. Electrochim. Acta 297:1018–1027

9. Kim J, Renault C, Nioradze N, Arroyo-Currás N, Leonard KC, Bard AJ (2016) Electrocatalytic Activity of Individual Pt Nanoparticles Studied by Nanoscale Scanning Electrochemical Microscopy. J. Am. Chem. Soc. 138(27):8560–8568

10. Filotás D, Fernández-Pérez BM, Nagy L, Nagy G, Souto RM (2020) A novel scanning electrochemical microscopy strategy for the investigation of anomalous hydrogen evolution from AZ63 magnesium alloy. Sens. Actuators B Chem. 308:127691

11. Iffelsberger C, Vatsyayan P, Matysik F-M (2017) Scanning Electrochemical Microscopy with Forced Convection Introduced by High-Precision Stirring. Anal. Chem. 89(3):1658–1664

12. Raith T, Wert S, Iffelsberger C, Matysik F-M (2018) Development and characterization of electrochemical flow cells for hydrodynamic scanning electrochemical microscopy. Monatsh. Chem. 149(9):1671–1677

13. Raith T, Iffelsberger C, Vatsyayan P, Matysik F-M (2019) Impacts of Forced Convection Generated via High Precision Stirring on Scanning Electrochemical Microscopy Experiments in Feedback Mode. Electroanalysis 31(2):273–281

14. Wert S, Fußstetter A, Iffelsberger C, Matysik F-M (2020) Scanning Electrochemical Microscopy of Electrically Heated Wire Substrates. Molecules 25(5):1169

15. Gründler P, Kirbs A, Zerihun T (1996) Hot-wire electrodes: voltammetry above the boiling point. Analyst 121(12):1805–1810

16. Gründler P, Dunsch L (2015) Thermal switching of redox reactions at gold electrodes. J. Solid State Electrochem. 19(1):23–29

17. Gründler P, Flechsig G-U (1998) Deposition and stripping at heated microelectrodes. Arsenic(V) at a gold electrode. Electrochim. Acta 43(23):3451–3458

18. Flechsig G-U, Korbut O, Gründler P (2001) Investigation of Deposition and Stripping Phenomena at the Heated Gold Wire Electrode in Comparison to the Rotating Disk Electrode: Copper(II), Mercury(II), and Arsenic(III). Electroanalysis 13(8-9):786–788

19. Biala K, Sedova A, Flechsig G-U (2015) Sequence and Temperature Influence on Kinetics of DNA Strand Displacement at Gold Electrode Surfaces. ACS Appl. Mater. Interfaces 7(36):19948–19959

20. Voß T, Gründler P, Kirbs A, Flechsig G-U (1999) Temperature pulse voltammetry: hot layer electrodes made by LTCC technology. Electrochem. Commun. 1(9), 383-388

21. Clausmeyer J, Schäfer D, Nebel M, Schuhmann W (2015) Temperature-Induced Modulation of the Sample Position in Scanning Electrochemical Microscopy. ChemElectroChem 2(7):946–948

22. Boika A, Zhao Z (2016) First principles of hot-tip scanning electrochemical microscopy: Differentiating substrates according to their thermal conductivities. Electrochem. Commun. 68:36–39

23. Zhao Z, Leonard KC, Boika A (2019) Hot-Tip Scanning Electrochemical Microscopy: Theory and Experiments Under Positive and Negative Feedback Conditions. Anal. Chem. 91(4):2970–2977

24. Frkonja-Kuczin A, Alicea-Salas JY, Arroyo-Currás N, Boika A (2020) Hot-SWV: Square Wave Voltammetry with Hot Microelectrodes. Anal. Chem. 92(13):8852–8858

25. Wang J (2008) Electrochemical Glucose Biosensors. Chem. Rev. 108(2):814–825

26. Mateo C, Palomo JM, Fernandez-Lorente G, Guisan JM, Fernandez-Lafuente R (2007) Improvement of enzyme activity, stability and selectivity via immobilization techniques. Enzyme Microb. Technol. 40(6):1451–1463

27. Chen L, Wu Z-Q, Wang C, Ouyang J, Xia X-H (2012) Exploring the temperature-dependent kinetics and thermodynamics of immobilized glucose oxidase in microchip. Anal. Methods 4(9):2831

28. Tseng T-F, Yang Y-L, Chuang M-C, Lou S-L, Galik M, Flechsig G-U, Wang J (2009) Thermally Stable Improved First-Generation Glucose Biosensors based on Nafion/Glucose-Oxidase Modified Heated Electrodes. Electrochem. Commun. 11(9):1819–1822

29. Khan AY, Noronha SB, Bandyopadhyaya R (2014) Glucose oxidase enzyme immobilized porous silica for improved performance of a glucose biosensor. Biochem. Eng. J. 91:78–85

30. Y. Li, Y. Yuan, D. Gong, W. Hu, M. Yang (2018) A SPR Glucose Sensor Based on Immobilized Glucose Oxidases and Silica Mesocellular Foams. IEEE Sens. J. 18(6):2229–2235

31. Wittstock G, Burchardt M, Pust SE, Shen Y, Zhao C (2007) Scanning Electrochemical Microscopy for Direct Imaging of Reaction Rates. Angew. Chem. Int. Ed. 46(10):1584–1617

32. Inga Morkvenaite-Vilkonciene, Almira Ramanaviciene, Aura Kisieliute, Vytautas Bucinskas, Arunas Ramanavicius (2019) Scanning electrochemical microscopy in the

development of enzymatic sensors and immunosensors. Biosens. Bioelectron. 141:111411

33. Morkvenaite-Vilkonciene I, Ramanaviciene A, Genys P, Ramanavicius A (2017) Evaluation of Enzymatic Kinetics of GOx-based Electrodes by Scanning Electrochemical Microscopy at Redox Competition Mode. Electroanalysis 29(6):1532–1542
34. Morkvenaite-Vilkonciene I, Ramanaviciene A, Ramanavicius A (2014) Redox competition and generation-collection modes based scanning electrochemical microscopy for the evaluation of immobilised glucose oxidase-catalysed reactions. RSC Adv. 4(91):50064–50069
35. Ivanauskas F, Morkvenaite-Vilkonciene I, Astrauskas R, Ramanavicius A (2016) Modelling of Scanning Electrochemical Microscopy at Redox Competition Mode Using Diffusion and Reaction Equations. Electrochim. Acta 222:347–354
36. Morkvenaite-Vilkonciene I, Genys P, Ramanaviciene A, Ramanavicius A (2015) Scanning electrochemical impedance microscopy for investigation of glucose oxidase catalyzed reaction. Colloids and Surf. B: Biointerfaces 126:598–602
37. Zoski CG (2002) Ultramicroelectrodes: Design, Fabrication, and Characterization. Electroanalysis 14(15-16):1041–1051
38. Gründler P (2015) In-situ Thermoelectrochemistry. Springer Berlin Heidelberg, Berlin, Heidelberg
39. Gründler P, Degenring D (2001) The Limits of Aqueous Hot-Wire Electrochemistry: Near-Critical and Supercritical Fluids in Electrochemical Sensors. Electroanalysis 13(8-9):755–759

4.4. Flow reactor: highly spatially resolved catalyst formation and in operando monitoring of the catalytic activity

Christian Iffelsberger, Stefan Wert, Frank-Michael Matysik and Martin Pumera

Submitted for publication

This chapter was submitted for publication and was changed for reasons of uniformity. The changes herein consist of minor corrections, formatting, and the addition of the supporting information to the main text.

Abstract

Flow reactors are of increasing importance and became crucial devices due to their wide application in chemical synthesis, electrochemical hydrogen evolution reaction (HER) or electrochemical wastewater treatment. In many of these applications, catalyst materials such as transition metal chalcogenides (TMC) for HER are providing the desired electrochemical reactivity. Generally, the flow electrolyzers' performance is evaluated as overall output, but the decrease in activity of the electrolyzer is due to localized failure of the catalyst. Herein, we present a method for the highly spatially resolved (tens of micrometers) in-situ analysis of the catalytic activity under real operation conditions as well as the localized deposition of the catalyst in an operating model flow reactor. For these purposes, scanning electrochemical microscopy was applied for MoS_x catalyst deposition as well as for localized tracking of the TMC activity with a resolution of 25 µm. This approach offers detailed information about the catalytic performance and should find broad application for the characterization and optimization of flow reactor catalysis under real operation conditions.

4.4.1. Introduction

Flow reactors possess several processing advantages like improved thermal management, mixing control, increased safety, and scalability [1]. Especially in combination with electrochemistry, which uses only electrons for chemical conversion, they are considered as "green" technology [2]. Flow reactors are of rapidly increasing importance for industrial applications like the electrochemical hydrogen evolution reaction HER, wastewater treatment and as alternative to the batch reactor technology for chemical synthesis [3,4]. The fabrication of flow reactors with additive manufacturing, also known as 3D printing, has attracted enormous interest [5,6]. The simplicity of 3D printing revolutionizes the manufacturing of electrochemical devices since it allows the fast, low-cost, and customized fabrication of nearly

any imaginable design at any place [7–9]. Furthermore, it allows the delocalized duplication of any generated design for the systematic improvement throughout different researchers around the world by simple sending the digital file and printing it. The most common and simplest type of 3D printing is the fused filament modeling (FFM) [9]. Here, a molten thermoplastic filament is extruded through a heated nozzle to form the desired part layer by layer. The FFM technique is widely used for the fabrication of chemical resistant flow reactors applicable for electrolysis, synthesis and sensing application [10–12].

Since the report by Chorkendorff et al. [13], transition metal chalcogenides (TMC), attracted great interest as potent catalyst materials for HER to replace less abundant and expensive platinum-based catalysts [14,15]. Common strategies for the bottom-up synthesis of TMCs are wet chemical synthesis, chemical vapor deposition, or atomic layer deposition [16–19]. The main drawbacks of these techniques are the requirement of complex equipment and the harsh experimental conditions such as high temperature or pressure, as well as multiple time-consuming work steps. In contrast, the electrochemical synthesis is a simple bottom-up alternative with multiple advantages. The process is fast and easily scalable with good control of the deposition over templates and offers a high diversity in the choice of substrates and precursors [20–25]. Most importantly, the electrochemical deposition requires only simple instrumentation and gives great flexibility in the experimental conditions to deposit catalyst materials. For their analysis, scanning electrochemical microscopy (SECM) is a powerful and versatile electrochemical technique [26]. It is generally employed for the investigation of electrochemical surface properties and phenomena providing detailed information of the (electro)chemical activity [27–30]. Additionally, SECM allows for the localized modification of surfaces and the electrodeposition of metals and catalyst materials with the same advantages as the common electrodeposition [31–33]. The general applicability of the SECM in hydrodynamic systems for the study of the electrochemical activity in dependence on morphological features of the substrate due to the formation of steady-state diffusion layers was recently demonstrated [34–37]. Further improvements led to the development of a flow cell powered by a high-performance liquid chromatography (HPLC) pump for SECM experiments [38]. On the one hand, utilizing an HPLC pump allows a continuous operation of the flow reactor but comes with the restriction of using nonaggressive solutions to prevent damage to the interior parts of the pump. Syringe pumps, on the other hand, are widely used for flow reactor applications because they are cost-efficient and applicable to aggressive media. As both processes, catalyst deposition and the HER, require corrosive chemicals, using a syringe pump allows the electrodeposition and the monitoring of the local activity during flow reactor operation. Combined with the ability of the SECM to locally deposit fresh catalyst, this information can be used for the targeted replacement or refreshment of catalyst. This can lead to prolongation of electrode lifetime and possibly avoid the need of electrode replacement due

to decreasing effectivity. Therefore, costs can be reduced, and valuable resources can be saved.

In this work, for the first time the direct formation of catalyst material by localized electrochemical deposition inside an operating flow cell directly followed by the continuous monitoring of the catalyst's activity under operation conditions is presented. For demonstration, MoS_x is deposited as catalyst material during flow in conjunction with in-situ imaging of its local activity. The latter is executed by measuring the amount of hydrogen evolved during HER using SECM in substrate generation/tip collection (SG/TC) mode. The general possibility of 3D printing of flow reactors is demonstrated by working with a 3D printed flow cell consisting of only two parts (excluding the electrodes and tube connectors). It will be shown that the presented method is versatile and can find broad application in the characterization of flow reactor-based systems for catalysis under real operation conditions.

4.4.2. Materials and methods

4.4.2.1. Chemicals

For flow cell characterization measurements and feedback mode imaging, a 1.5 mM solution of ferrocene methanol (FcMeOH, 99%, ABCR, Germany) with 0.2 M KNO_3 (analytical grade, Merck KGaA, Germany) as supporting electrolyte was used as redox mediator. As MoS_x precursor solution, an aqueous solution of 10 mM NH_4MoS_4 (99.97%, Sigma-Aldrich) with 0.1 M KCl (analytical grade, Merck KGaA, Germany) was used. Other chemicals were H_2SO_4 (ROTIPURAN®Supra 95%, Carl Roth GmbH + Co. KG, Germany) and 96% ethanol (analytical grade, Merck KGaA, Germany). All aqueous solutions were prepared with deionized water with a resistance >18 MΩ cm^{-1} (Milli-Q Advantage A10 system, Merck Millipore, Germany).

4.4.2.2. 3D printing of the SECM flow cell

For 3D printing of the SECM flow cell, a Prusa i3 MK3 printer (Prusa Research, Czech Republic) with poly lactic acid (PLA) filament (Galaxy Silver, Prusa Research, Czech Republic) was used. The flow cell was designed using COMSOL Multiphysics 5.2 and converted into Standard Triangle Language (STL)-file format. The schematics of both the bottom and top part of the 3D printed flow cell are provided in **Figure 4.4.1**. Slicing of the STL-file was done in Slic3r Prusa software (Prusa Research, Czech Republic) with 20% infill.

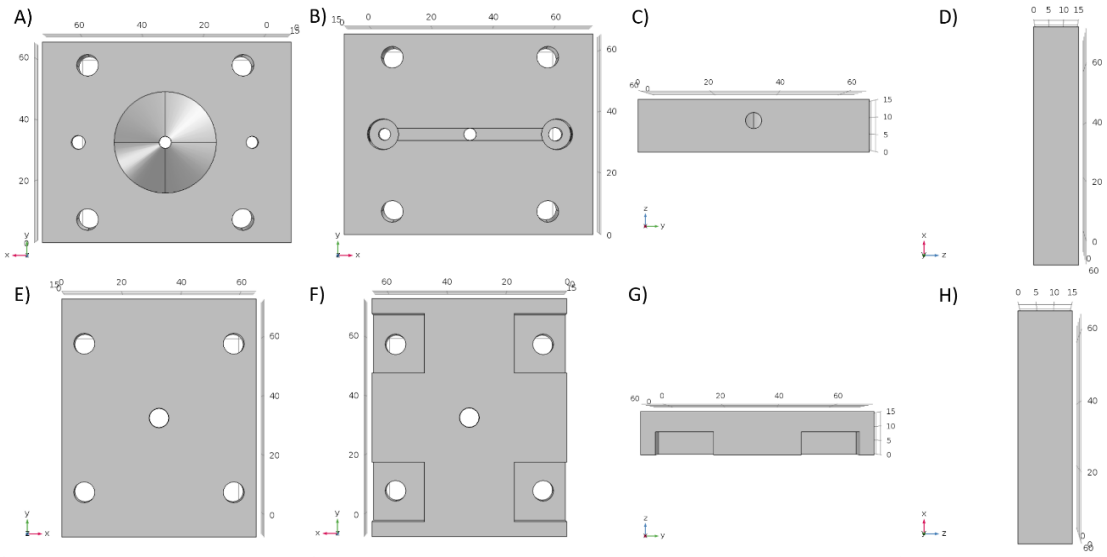

Figure 4.4.1: Schematic representation of the 3D printed flow cell for scanning electrochemical microscopy measurements. **A** – **D**) Top, down, front/back and side view of the Top part of the 3D printed flow cell, respectively. **E**) – **H**) Top, down, side and front/back view of the bottom part of the 3D printed flow cell, respectively. The scales in the figures are in mm.

4.4.2.3. Experimental setup

All electrochemical measurements were carried out using a commercially available SECM 920C (CH Instruments, USA). Experiments were performed using an Ag/AgCl/1 M KCl reference electrode. If not stated different, all reported potentials refer to this reference system. In characterization experiments, a 1 mm diameter Pt wire served as counter electrode. **Figure 4.4.2A** shows the schematic representation of the experimental setup. As electrochemical cells for hydrodynamic SECM experiments, two semi closed flow cell designs, either made of Polytetrafluoroethylene (PTFE) or 3D printed PLA, were used. The design and dimensions of the PTFE based flow cell were previously reported [38]. The assembled flow cell is shown in **Figure 4.4.2B** and consisted of two parts. The body part (**Figure 4.4.2C**) exhibited the inlet, flow channel, substrate electrode, outlet and a reservoir. The top part, shown in **Figure 4.4.2D**, was used to close the channel and provided holes for the ultra-microelectrode (UME), a counter and a reference electrode. The assembled 3D printed flow cell is shown in **Figure 4.4.2E**. It also consisted of two parts and featured a flow channel of 4.0 mm width and 0.5 mm height. The bottom part (**Figure 4.4.2F**) provided space for the substrate electrode and the top part included the flow channel, in- and outlet, and the openings for the UME, counter and reference electrodes. Additional holes were included in the corners of both pieces for the assembling and the fixation of the 3D printed flow cell at the SECM sample stage via screws. After assembling, addition hot glue (Pattex, Henkel AG & Co. KGaA, Germany) ensured the complete sealing of the 3D printed flow cell. For establishing reproducible flow conditions, a

laminar flow of the electrolyte solution from the outlet into a reservoir had to be ensured. Forced convection was generated with a syringe pump (New Era Pump Systems Inc., USA) equipped with a 100 mL bladder syringe (BD Plastipak). The bladder syringe was connected to the 3D printed SECM flow cell via silicone tubing (inner diameter: 3 mm) and to the PTFE flow cell with polyether ether ketone tubing. The electrochemical characterization of the hydrodynamic system was carried out by performing chronoamperometry and probe approach curves (PACs) at a 2 mm diameter Pt disk electrode. The detailed description of the used methods as well as the results and its discussion are provided in the supporting information.

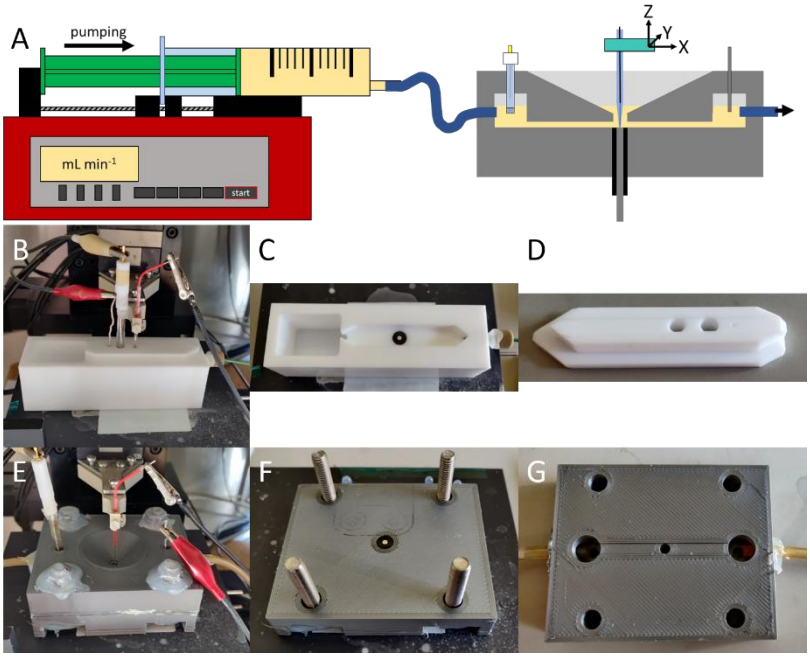

Figure 4.4.2: Schematic representation of the experimental setup (**A**) and photographs of the used electrochemical flow cells. (**B**) Assembled Teflon flow cell with electrodes inserted. (**C**) Bottom piece of the PTFE cell with Pt disk substrate electrode placed in the channel. (**D**) Top piece of the PTFE flow cell. (**E**) Assembled 3D printed flow cell with electrodes inserted. (**F**) Bottom piece of the 3D printed cell with Pt disk substrate electrode. (**G**) Top piece of the 3D printed cell with electrode placeholders and tube connections.

4.4.2.4. Characterization of the hydrodynamic system

The electrochemical characterization of the hydrodynamic system was carried out by performing chronoamperometry at a 2 mm diameter Pt disk electrode. Before assembling the flow cells, the Pt disk electrode was polished using Al_2O_3 slurry (0.3 µm particle size) and polishing cloth. Chronoamperometric measurements were carried out in the 3D printed cell at different flow rates (v = 0.0, 0.5, 0.8, 1.2, and 2.1 mL min^{-1}) for 200 s with $E_{substrate}$ = 0.5 V. For the monitoring of the generated diffusion layers, PACs towards the substrate electrode were recorded with a 25 µm diameter UME (RG ≈ 2, fabricated according to [39]) in SG/TC and

competition mode at different flow rates of v = 0, 0.5, 1.2, 2.1 mL min^{-1}. The applied potentials were E_{UME} = 0.0 V, and $E_{Substrate}$ = 0.5 V in SG/TC mode and E_{UME} = $E_{Substrate}$ = 0.5 V in competition mode. Prior to the PACs, the UME was approached to a substrate-to-tip distance of 10.5 µm using feedback mode and retracted to a total distance of 500 µm. The approach towards the surface was done at 20 µm s^{-1} after a quiet time of 20 s. For the investigation of the convective effects in SECM, the 2 mm diameter Pt disk electrode was imaged with a 25 µm diameter UME in quiescent solution and with flow in feedback mode (E_{UME} = 0.4 V, v = 1.7 mL min^{-1}), SG/TC ($E_{substrate}$ = 0.5 V, E_{UME} = 0.0 V, v = 2.1 mL min^{-1}) and competition mode ($E_{substrate}$ = E_{UME} = 0.5 V, v = 2.1 mL min^{-1}). Imaging in feedback mode was done at a tip-to-substrate separation of ~ 23 µm with a pixel size of 5 µm at a scan speed of 125 µm s^{-1}. Imaging in SG/TC and competition mode was done at a tip-to-substrate separation of ~ 6 µm, a pixel size of 6 µm and a scan speed of 60 µm s^{-1}.

4.4.2.5. Localized electrochemical deposition of MoSx

The high resolution electrochemical additive manufacturing (EAM) of MoS_x and the subsequent characterization *via* SECM was done in the PTFE SECM flow cell. For subsequent experiments, the mediator, precursor and 0.5 M sulfuric acid solution were exchanged by flushing the flow cell with deionized water and required solution, switching the solution inside the syringe, and priming the flow cell for ~ 1 min with the new solution. The EAM was done using direct mode SECM with a three-electrode setup [40]. In this configuration, the substrate electrode is employed as working electrode and the UME as counter electrode. For the EAM of the MoS_x, the PTFE flow cell was modified to enable the use of the glassy carbon (GC) plate (5 x 12 mm Sigradur G, Hochtemperatur-Werkstoff GmbH, Germany). The GC plates were connected to the potentiostat via a Cu cable adhered with Ag epoxy resin (Silver Epoxy 8331, MG Chemicals, Canada). Before assembling the PTFE flow cell, the GC plates were polished with Al_2O_3 slurry and polishing cloth, rinsed with deionized water, sonicated for 5 min in 96% Ethanol, again rinsed with water, and dried with N_2. Before the EAM, the tilt of the GC substrate was adjusted below 1 µm mm^{-1} in X and Y direction with a 10 µm diameter Pt disk UME (RG > 10, Sensolytics, Germany). For the deposition, the UME was positioned at a substrate-to-tip distance of ~5 µm via feedback mode PAC in FcMeOH solution. After switching to precursor solution, the EAM was performed by scanning the UME in lines (900 µm length) across the substrate, with $E_{substrate}$ = 0.47 V and a scan velocity of 10 µm s^{-1} in constant height. The deposited pattern is given in **Figure 4.4.3**. In Total 4 lines, two sets of two lines per set were deposited. The first two lines were deposited in quiescent solution and the following lines were deposited with a flow of v = 1.4 mL s^{-1} using a 60 mL bladder syringe. The distance between the two sets was 600 µm and the distance between the single lines was 300 µm.

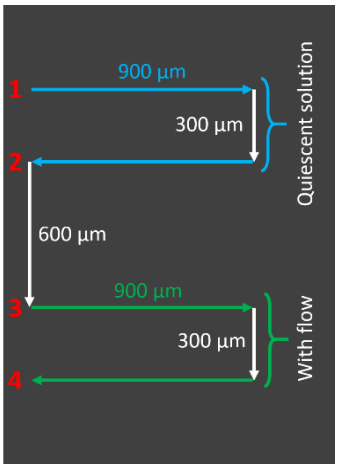

Figure 4.4.3: Deposition pattern for MoS_x catalyst using direct mode SECM.

4.4.2.6. Scanning electrochemical microscopy characterization of locally deposited MoS_x

For the subsequent characterization of the fabricated MoS_x with SECM, a 25 µm diameter Pt disk UME (RG > 10, Sensolytics, Germany) was used in constant height at an initial tip-to-substrate distance of ~16 µm. The HER activity of the fabricated EAM was imaged after switching from precursor solution to 0.5 M H_2SO_4 in SG/TC mode. The H_2 detection potential was E_{UME} = 0.1 V. Hydrogen was generated subsequent at varying potentials $E_{substrate}$ = –0.9 V, –1 V. The characterization in feedback mode was performed after switching back to FcMeOH mediator solution with E_{UME} = 0.4 V at a constant height of ~15 µm. SECM imaging of the fabricated MoS_x was done with a scan speed of 416.6 µm s^{-1}, a pixel size of 25 µm and 10 s quiet time.

4.4.2.7. Material characterization

The characterization of the fabricated MoS_x with scanning electron microscopy (SEM) and energy dispersive X-ray spectroscopy (EDS) was done with a LYRA 3 SEM (Tescan, Czech Republic) equipped with an XFlash 5010 EDS (Bruker, USA) with an accelerating voltage of 20 kV. Optical imaging of the MoS_x deposit was done with a confocal laser scanning microscope (CLSM, Lext OLS4100, Olympus, Japan).

4.4.3. Results & discussion

The schematic illustration of the workflow for depositing and analyzing the catalyst under flow conditions is presented in **Figure 4.4.4**. The high resolution EAM of MoS_x by the localized electrochemical synthesis inside the operating flow reactor was done via direct mode-SECM

from precursor solution, which is depicted in **Figure 4.4.11A**. Afterwards, the catalysts activity for HER was investigated in flow conditions by SECM in SG/TC mode as shown in **Figure 4.4.11B**. In SG/TC mode, the UME was used to detect (detection electrode, DE) the H_2 produced at the substrate. In both modes, a reference electrode (RE) completed the electrical circuit. The switching between both modes enabled on one hand the continuous monitoring of the activity of the catalyst material, and on the other hand its activation or replacement in case of decreasing activity or catalyst detachment.

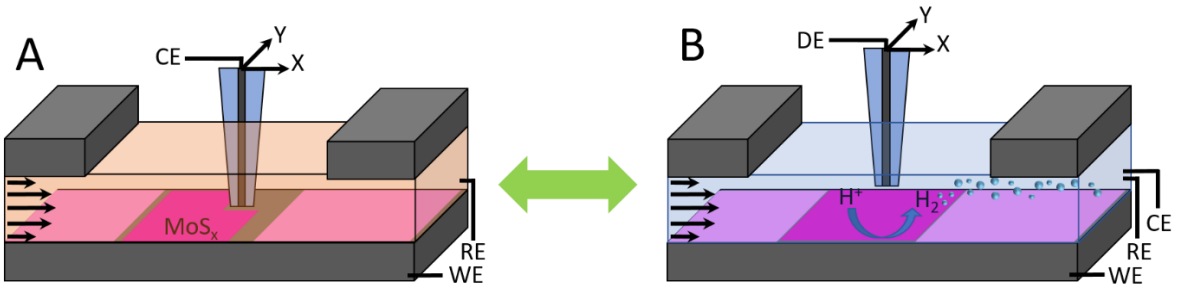

Figure 4.4.4: Schematic illustration of the implementation of scanning electrochemical microelectrode system to localized and controllable electrodeposition of the catalyst (**A**) and to in-situ in-flow monitoring of the catalyst behavior (**B**). More specifically, **A:** High resolution electrochemical additive manufacturing of the MoS_x electrocatalyst from precursor solution under flow conditions by SECM in direct mode. **B:** SECM operated in SG/TC mode to scan for the hydrogen evolution reaction activity of the catalyst during flow reactor operation. The abbreviations are used for working electrode (WE), counter electrode (CE), detection electrode (DE), and reference electrode (RE).

4.4.3.1. Characterization of the hydrodynamic system.

Prior to the demonstration of the feasibility of the before mentioned approach, the hydrodynamic system consisting of a syringe pump and the flow cell was characterized regarding its applicability to hydrodynamic SECM experiments. Compared to commonly used pumps for high performance liquid chromatography like reciprocating pumps or membrane pumps, the utilization of a syringe pump is cheap and offers the advantage to use reactive and corrosive media like the precursor solution and sulfuric acid. Since a laminar flow in electrochemical experiments leads to an enhanced mass transport and a well-defined steady-state current at large electrodes, the flow generated with the syringe pump was characterized using chronoamperometry for the oxidation of FcMeOH at the 2 mm Pt disk electrode. **Figure 4.4.5** shows the chronoamperograms recorded in absence and presence of convection at different flow rates using the 3D printed flow cell. In case of quiescent conditions, the typical current decay according to the Cottrell equation was observed over the entire 200 s measurement period due to the growing diffusion layer. Under flow conditions, steady-state currents were developed in less than 5 s, indicating the formation of stable diffusion layers.

The magnitude of the current was proportional to the flow rate with steady-state currents of 3.35 ± 0.05 µA, 4.80 ± 0.05 µA, 4.74 ± 0.08 µA and 5.82 ± 0.09 µA for flow rates of 0.5, 0.8, 1.2 and 2.1 mL min^{-1}, respectively. The minor oscillations in the measured current occurred with frequencies corresponding to the flow rate selection, indicating slight variations of the syringe pump speed.

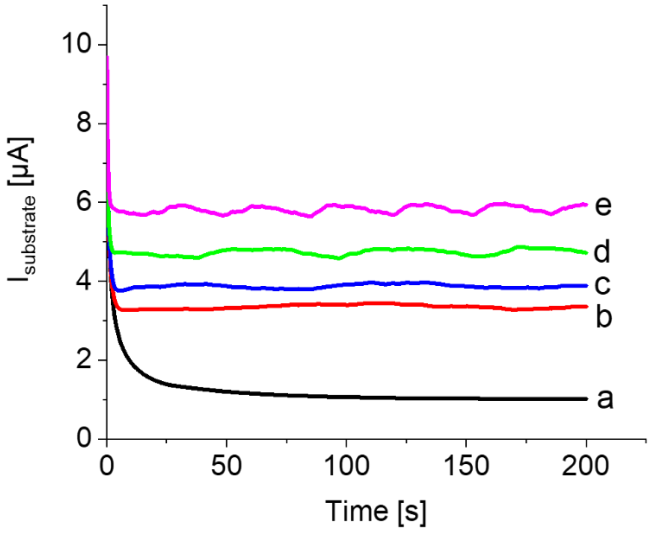

Figure 4.4.5: Chronoamperometric recordings for the oxidation of FcMeOH at a Pt disk electrode (diameter = 2 mm) in the 3D-printed SECM flow cell at different mediator flow rates, (**a**) without flow, (**b**) 0.5 mL min^{-1}, (**c**) 0.8 mL min^{-1}, (**d**) 1.2 mL min^{-1}, (**e**) 2.1 mL min^{-1}. The electrode potential was set to $E_{substrate}$ = 0.45 V.

The applicability of the 3D printed flow cell for hydrodynamic SECM was characterized by the investigation of the diffusion layers of FcMeOH and its oxidized species $FcMeOH^+$ in the vicinity of a 2 mm Pt disk electrode at varying flow rates. The diffusion layers of FcMeOH and $FeMeOH^+$ were recorded with probe approach curves (PACs) in competition and SG/TC mode, respectively and are depicted in **Figure 4.4.6**. The PTFE flow cell was developed initially and its characterization as shown in **Figure 4.4.6A**, **B** served as reference for the characterization of the 3D printed flow cell (**Figure 4.4.6C**, **D**). The reproducibility of the diffusion layers was characterized by the repetitive recording (three times) of the PACs. The approach curves recorded in SG/TC mode for the PTFE (**Figure 4.4.6A**) and the 3D printed flow cell (**Figure 4.4.6C**) show steady and reproducible diffusion layers when convection is introduced. The diffusion layers became smaller with increasing flow rate. Under quiescent conditions, the diffusion layers kept growing, resulting in poor reproducibility. Similar observations can be made in the competition mode measurements shown in **Figure 4.4.6B** and **D** for the PTFE and the 3D printed flow cell, respectively. The thickness of the diffusion layers decreased with increasing flow rate and the laminar flow enhanced the reproducibility of their formation. In contrast to the PACs in SG/TC mode, the detected signals in the bulk phase are drastically

increased with higher flow rates. While approaching the surface, the current is decreasing, showing the effect of the convection on the current measured at the UME. Additionally, small disturbances of the signal in bulk solution were visible in **Figure 4.4.6D**, which indicate small distortions of the laminar flow. Nevertheless, at small substrate-to-tip distances the diffusion layer was stable and reproducible. These results confirm the applicability of the syringe pump and the 3D printed flow cell for hydrodynamic SECM. The fast and cheap and prototyping by the 3D printing enables unique, novel and sophisticated cell designs widening the general applicability of the SECM. Since Raith et al. reported optimized SECM imaging results using the high flow rates, a flow rate of 2.1 mL min^{-1} was chosen for the following SECM imaging experiments [38].

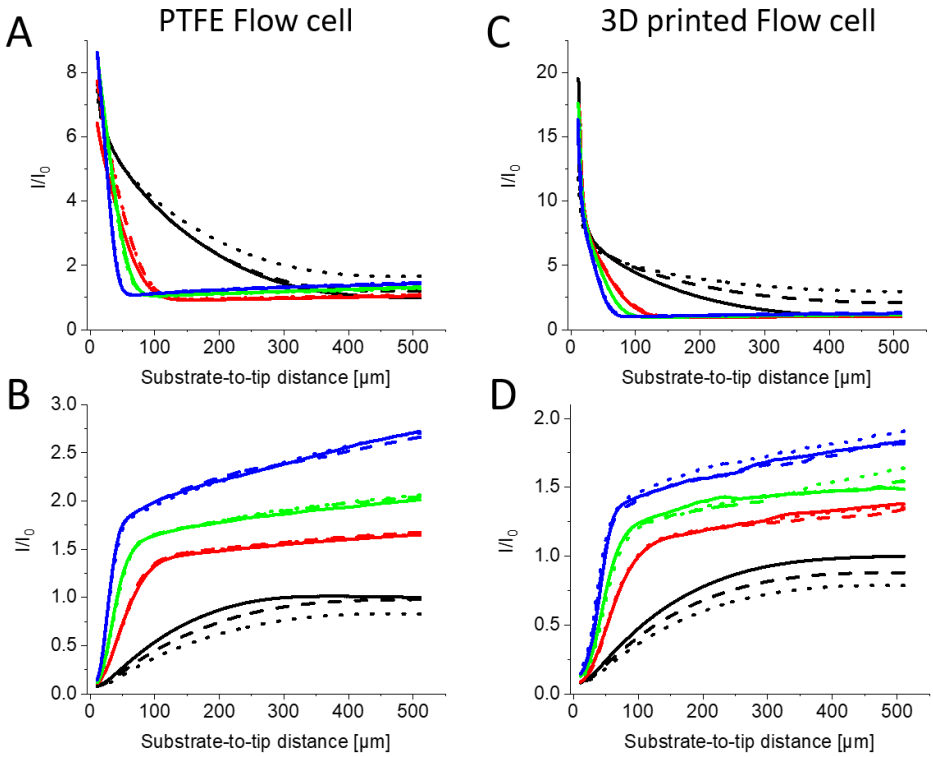

Figure 4.4.6: Comparison study of the diffusion layers in the vicinity of a 2 mm Pt disk electrode applying various flow rates (black: without flow; red: 0.5 mL min^{-1}; blue: 1.2 mL min^{-1}; green: 2.1 mL min^{-1}) in the PTFE flow cell (**A**, **B**) and the 3D printed flow cell (**C**, **D**). PACs were recorded in SG/TC mode (**A**, **C**) with electrode potentials of $E_{substrate}$ = 0.5 V, E_{UME} = 0.0 V and in competition mode (**B**, **D**) with $E_{substrate}$ = E_{UME} = 0.5 V. The PACs were recorded three times for each flow rate (1^{st}/2^{nd}/3^{rd} measurement: solid/dashed/dotted line).

As the utilization of the SECM for the monitoring of the catalytic activity during operating flow reactor conditions is one of the main goals, the applicability of the syringe pump for this purpose was demonstrated by the comparison of SECM images recorded in stationary and flow conditions using common SG/TC and competition mode. In **Figure 4.4.7**, subsequently recorded images of a 2 mm Pt disk electrode with a rough surface recorded in quiescent

solution and with flow (v = 2.1 mL min^{-1}) are shown. The images were recorded in SG/TC (**Figure 4.4.7A** and **B**) and competition mode (**Figure 4.4.7C** and **D**) and show for both modes under stationary conditions a gradient of the signal from the bottom to the top. This distortion was a result of the growing diffusion layer and made the interpretation of images more difficult. In contrast, forced convection enabled the distortion-free imaging in SG/TC mode as shown in **Figure 4.4.7B**. In the competition mode (**Figure 4.4.7D**), the flow of mediator enhanced the detected signal resulting in a strongly enhanced (~320%) electrochemical contrast compared to quiescent solution. Regardless of the minor distortions visible in **Figure 4.4.7D**, the results show that syringe pumps are a suitable alternative for hydrodynamic SECM studies in flow reactor applications.

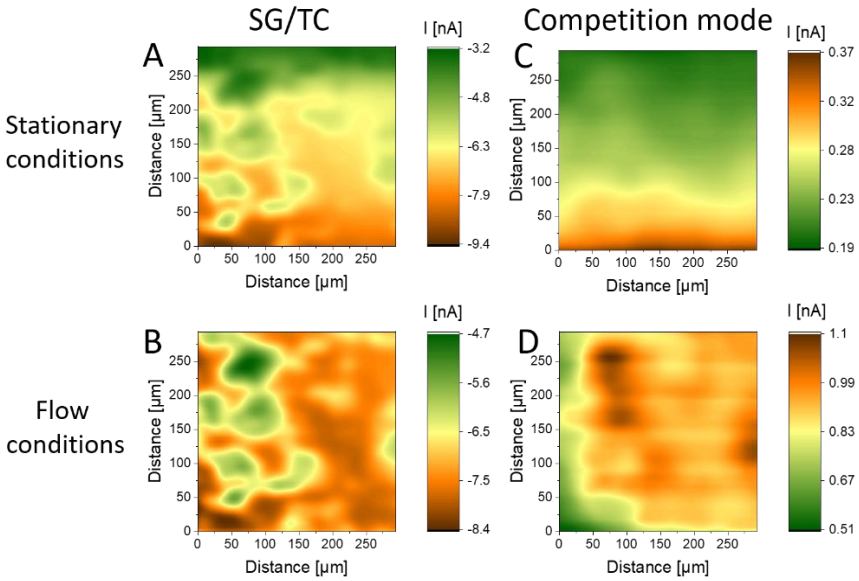

Figure 4.4.7: Comparison of scanning electrochemical micrographs of a 2 mm Pt disk electrode record in SG/TC mode (**A**, **B**) and competition mode (**C**, **D**) in stationary conditions and with a flow of v = 2.1 mL min^{-1}. The images were recorded in the PTFE flow cell with $E_{substrate}$ = 0.5 V, E_{UME} = 0.0 V for SG/TC and $E_{substrate}$ = E_{UME} = 0.5 V in competition mode. The mediator solution was 1.5 mM FcMeOH in 0.2 M KNO_3.

4.4.3.2. Localized electrochemical additive manufacturing of the catalyst and subsequent monitoring of the catalyst activity

For the demonstration of the high resolution EAM of MoS_x and the subsequent monitoring of its catalytic activity in a flow reactor, the PTFE flow cell was used as electrochemical cell. For the EAM, direct mode-SECM (see **Figure 4.4.4A**) was utilized and $(NH_4)_2MoS_4$ precursor solution was loaded in the syringe and pumped through the flow cell. The deposition of the MoS_x HER catalyst was done by performing line scans with $E_{substrate}$ = 0.47 V as shown in **Figure 4.4.3**, according to the chemical equation (1) [41].

$$MoS_4^{2-} + 2e^- + 4H^+ \rightarrow MoS_2 + 2H_2S \; MoS_4^{2-} + 2e^- + 4H^+ \rightarrow MoS_2 + 2H_2S \quad (1)$$

The first two lines (line 1 and 2) were deposited in quiescent solution and the last two lines (line 3 and 4) under flow conditions (v = 1.4 mL s^{-1}). The corresponding probe scan curves (**Figure 4.4.8**), as an indicator for the amount of deposited MoS_x, show that in the first line the current was reaching the highest values of more than 50 µA while for the lines 2-4, currents between 2-10 µA were recorded.

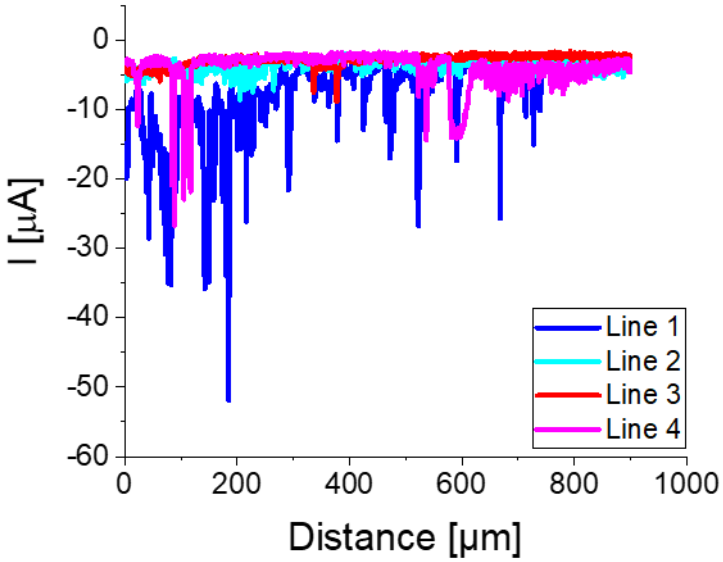

Figure 4.4.8: Probe scan curves of additive manufactured MoS_x using direct mode SECM. The potential of the working electrode was set to $E_{substrate}$ = 0.47 V.

The scanning electron micrograph of the deposited MoS_x is shown in **Figure 4.4.9A**. The highest amount of deposited catalyst was found to be in the beginning of the first line. The amount of deposited catalyst decreased quickly, resulting in a barely visible deposition in line 2. The application of forced convection in line 3 and 4 resulted in a successful and uniform localized deposition of MoS_x. The EDS elemental maps depicted in **Figure 4.4.9B**, **C** for Mo, and S, respectively, prove the presence of Mo and S in the deposit at the GC surface and show that the deposition was following the predefined pattern. Within the MoS_x, a homogeneous distribution of Mo and S is visible. The analysis of the EDS spectrum shown in **Figure 4.4.10** indicates an atomic surface coverage of 0.69% for Mo and 1.35% for S, resulting in a Mo to S ratio of 1.96. These observations show that the localized deposition in operating flow cells can possibly be used for the targeted replacement of partially deactivated catalyst material without the need to replace the whole electrode.

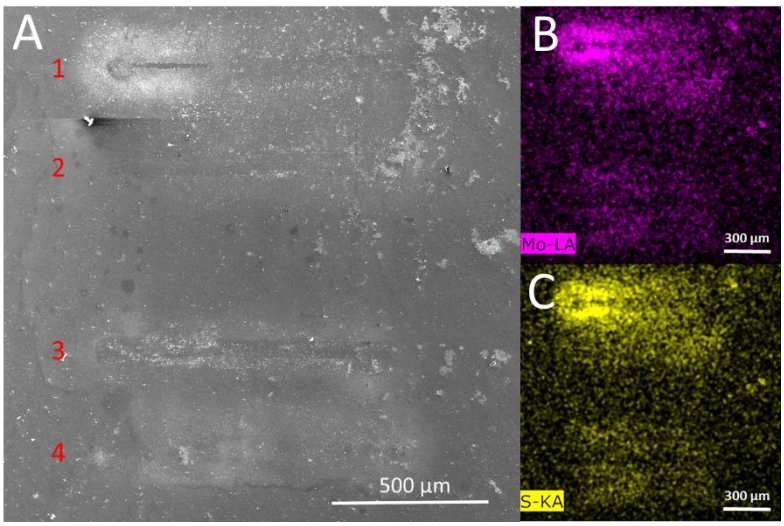

Figure 4.4.9A: Scanning electron micrograph of the localized electrochemical additive manufactured catalyst material together with energy dispersive X-ray elemental maps of the element distribution of Mo (**B**), and S (**C**).

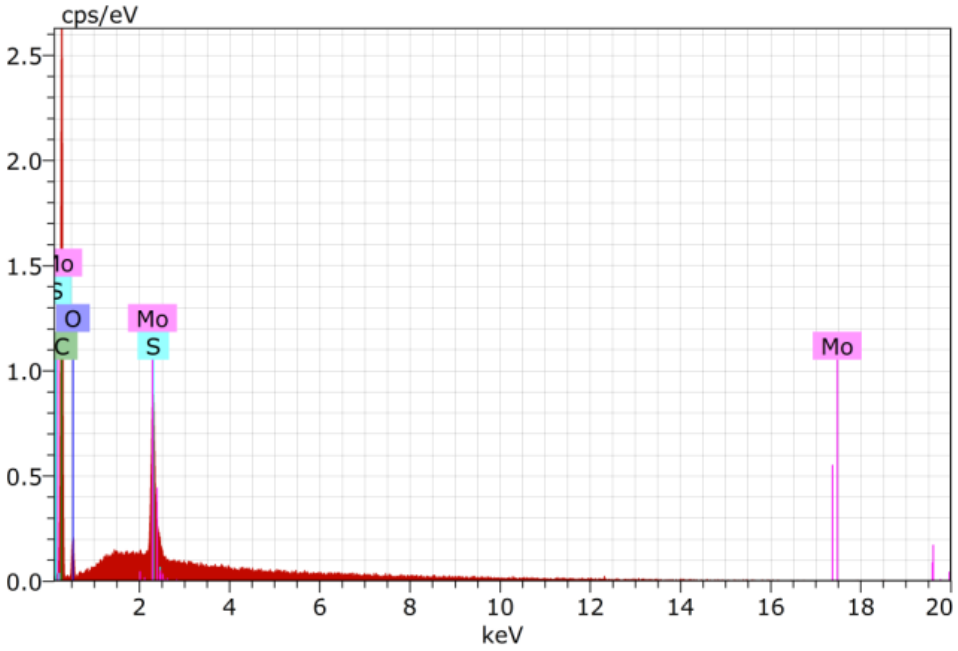

Figure 4.4.10: Energy dispersive X-ray spectra and of the local deposited catalyst.

The electrochemical characterization of the additive manufactured MoS_x was done by SECM imaging in SG/TC mode with a flow of 2.1 mL min^{-1} as well as in feedback mode (in stationary conditions). The feedback mode image of the deposit is presented in **Figure 4.4.11A** and shows good conductivity of the deposited material; thus, the image is reflecting the surface morphology. The depositions in line 1 and 2 resulted in a clearly visible coverage of the surface whereas lines 3 and 4 are barely visible, indicating a thin coverage with catalyst. The SG/TC mode image with forced convection, presented in **Figure 4.4.11B**, shows the HER activity in

0.5 M H_2SO_4 electrolyte as H_2 was generated at $E_{substrate}$ = –0.75 V. In general, the HER activity follows the predefined pattern which proves the localized deposition. The majority of the HER activity was located at the deposited MoS_x structure, with the highest activity detected at the first two lines. The beginning of the first line showed the highest detection current, where currents of up to 15.9 nA were recorded. Even though the SEM and the feedback mode images suggested only a minor deposition with flow conditions in the lines 3 and 4, the SG/TC mode image clearly shows HER activity with currents of up to 5.4 nA at this region. This proved a successful localized deposition of active catalyst material under flow conditions. The optical image given in **Figure 4.4.11C** additionally shows the metallic, bluish color of the deposit which is comparable to the color of pure MoS_2.

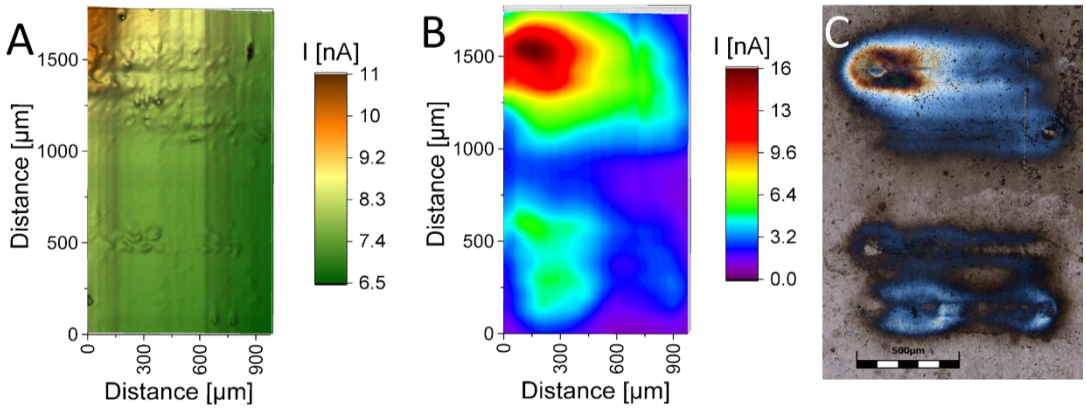

Figure 4.4.11: Electrochemical characterization of the locally deposited MoS_x catalyst with SECM. **A:** SECM micrograph recorded in quiescent solution using the feedback mode in 1.5 mM FcMeOH with 0.2 M KNO_3 with E_{UME} = 0.4 V. **B:** SECM micrograph of the hydrogen evolution reaction in 0.5 M H_2SO_4 with detection potential of E_{UME} = 0 V and $E_{substrate}$ = –0.75 V recorded in SG/TC mode with a flow of 2.1 mL min^{-1}. **C:** Optical image of the MoS_x deposit recorded with confocal laser scanning microscopy. SECM images were recorded in constant height with a pixel size of 25 µm, a max. scan speed of 416.6 µm s^{-1}.

To demonstrate the possibility of continuous monitoring of the catalyst activity during the operation of the flow reactor, the local H_2 evolution was consecutively imaged with increasing substrate potential. Imaging in 0.5 M H_2SO_4 under stationary conditions solution and at a flow rate of 2.1 mL min^{-1} allowed the comparison of both conditions, which is presented in **Figure 4.4.12**. In general, the application of flow resulted in an increased H_2 detection. For the substrate potential of $E_{substrate}$ = –0.9 V, a maximum 21.4 nA at line 1 and 8.4 nA at line 3 was found in contrast to 19.9 nA and 6.9 nA measured under stationary conditions at the same potential. The difference in the recorded signal was even more pronounced with $E_{substrate}$ = -1 V. With flow, maximum currents of 35.3 nA and 13.6 nA were recorded in lines 1 and 3, respectively, compared to 27.8 and 8.4 nA in stationary solution for the same lines. These results show that, in addition to local catalyst preparation in operating flow reactors, SECM can be applied for the continuous monitoring of catalyst activity.

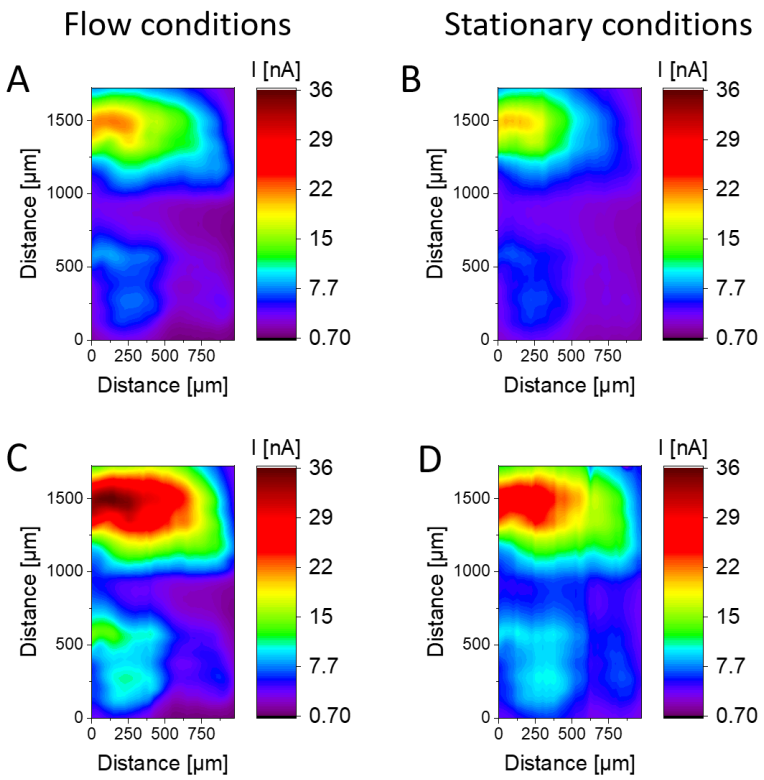

Figure 4.4.12: Monitoring of the HER activity of the fabricated MoS_x catalyst by applying different substrate potentials for SECM imaging in SG/TC mode. The monitoring was done in a flow reactor operated under flow (v = 2.1 mL s^{-1}) and in quiescent conditions. The H_2 generation potentials applied to the substrate electrode were $E_{substrate}$ = –0.9 V (**A**, **B**), –1 V (**C**, **D**). The collection potential at the UME was E_{UME} = 0 V. SECM images were recorded in constant height with a pixel size of 25 µm and a max. scan speed of 416.6 µm s^{-1}.

4.4.4. Conclusion

In this work, a 3D printed electrochemical flow cell was manufactured with the fused filament modeling technique to serve as a model flow reactor and successfully employed in hydrodynamic SECM experiments. The localized formation and direct characterization of the MoS_x catalyst inside the operating flow reactor was successfully demonstrated *via* local monitoring of the hydrogen evolution reaction. Using SECM under flow conditions proved that catalytic activity tracking is possible in operating flow reactors. As a positive side effect of the forced convection, an increased reproducibility and electrochemical contrast for SECM images was observed. Therefore, SECM can be applied for electrochemical flow reactor monitoring and maintenance without shutting down the reactor. Together with flow reactor models fabricated by 3D printing, many different types of flow reactors may be investigated in detail. This method should find broad applications in characterization of flow reactors.

References

1. Wiles C, Watts P (2012) Continuous flow reactors: a perspective. Green. Chem. 14(1):38–54
2. Nicholls TP, Schotten C, Willans CE (2020) Electrochemistry in continuous systems. Curr. Opin. Green. Sustain. Chem. 26:100355
3. Pletcher D, Green RA, Brown RCD (2018) Flow Electrolysis Cells for the Synthetic Organic Chemistry Laboratory. Chem. Rev. 118(9):4573–4591
4. Baumann M, Moody TS, Smyth M, Wharry S (2020) A Perspective on Continuous Flow Chemistry in the Pharmaceutical Industry. Org. Process Res. Dev. 24(10):1802–1813
5. Rossi S, Puglisi A, Benaglia M (2018) Additive Manufacturing Technologies: 3D Printing in Organic Synthesis. ChemCatChem 10(7):1512–1525
6. Parra-Cabrera C, Achille C, Kuhn S, Ameloot R (2018) 3D printing in chemical engineering and catalytic technology: structured catalysts, mixers and reactors. Chem. Soc. Rev. 47(1):209–230
7. Capel AJ, Rimington RP, Lewis MP, Christie SDR (2018) 3D printing for chemical, pharmaceutical and biological applications. Nat. Rev. Chem. 2(12):422–436
8. Au AK, Huynh W, Horowitz LF, Folch A (2016) 3D-Printed Microfluidics. Angew. Chem. Int. Ed. 55(12):3862–3881
9. Ambrosi A, Pumera M (2016) 3D-printing technologies for electrochemical applications. Chem. Soc. Rev. 45(10):2740–2755
10. Neumaier JM, Madani A, Klein T, Ziegler T (2019) Low-budget 3D-printed equipment for continuous flow reactions. Beilstein J. Org. Chem. 15:558–566
11. Ambrosi A, Shi RRS, Webster RD (2020) 3D-printing for electrolytic processes and electrochemical flow systems. J. Mater. Chem. A 8(42):21902–21929
12. Giorgini Escobar J, Vaněčková E, Nováková Lachmanová Š, Vivaldi F, Heyda J, Kubišta J, Shestivska V, Španěl P, Schwarzová-Pecková K, Rathouský J, Sebechlebská T, Kolivoška V (2020) The development of a fully integrated 3D printed electrochemical platform and its application to investigate the chemical reaction between carbon dioxide and hydrazine. Electrochim. Acta 360:136984
13. Jaramillo TF, Jørgensen KP, Bonde J, Nielsen JH, Horch S, Chorkendorff I (2007) Identification of active edge sites for electrochemical H_2 evolution from MoS_2 nanocatalysts. Science (New York, N.Y.) 317(5834):100–102

14. Chia X, Eng AYS, Ambrosi A, Tan SM, Pumera M (2015) Electrochemistry of Nanostructured Layered Transition-Metal Dichalcogenides. Chem. Rev. 115(21):11941–11966

15. Chia X, Pumera M (2018) Layered transition metal dichalcogenide electrochemistry: journey across the periodic table. Chem. Soc. Rev. 7(15):5602–5613

16. Wong SL, Liu H, Chi D (2016) Recent progress in chemical vapor deposition growth of two-dimensional transition metal dichalcogenides. Prog. Cryst. Growth Charact. Mater. 62(3):9–28

17. Bosi M (2015) Growth and synthesis of mono and few-layers transition metal dichalcogenides by vapour techniques: a review. RSC Adv. 5(92):75500–75518

18. Zhang Z, Zhao Y, Zhao Z, Huang G, Mei Y (2020) Atomic Layer Deposition-Derived Nanomaterials: Oxides, Transition Metal Dichalcogenides, and Metal–Organic Frameworks. Chem. Mater. 32(21):9056–9077

19. Tan C, Zhang H (2015) Wet-chemical synthesis and applications of non-layer structured two-dimensional nanomaterials. Nat. Commun. 6:7873

20. Ambrosi A, Pumera M (2016) Templated Electrochemical Fabrication of Hollow Molybdenum Sulfide Microstructures and Nanostructures with Catalytic Properties for Hydrogen Production. ACS Catal. 6(6):3985–3993

21. Chia X, Pumera M (2018) Inverse Opal-like Porous MoSex Films for Hydrogen Evolution Catalysis: Overpotential-Pore Size Dependence. ACS Appl. Mater. Interfaces 10(5):4937–4945

22. Chia X, Sutrisnoh NAA, Pumera M (2018) Tunable Pt-MoS_x Hybrid Catalysts for Hydrogen Evolution. ACS Appl. Mater. Interfaces 10(10):8702–8711

23. Ng S, Iffelsberger C, Sofer Z, Pumera M (2020) Tunable Room-Temperature Synthesis of ReS_2 Bicatalyst on 3D- and 2D-Printed Electrodes for Photo- and Electrochemical Energy Applications. Adv. Funct. Mater. 30(19):1910193

24. Tan SM, Pumera M (2017) Composition-Graded $MoWS_x$ Hybrids with Tailored Catalytic Activity by Bipolar Electrochemistry. ACS Appl. Mater. Interfaces 9(48):41955–41964

25. Mabayoje O, Liu Y, Wang M, Shoola A, Ebrahim AM, Frenkel AI, Mullins CB (2019) Electrodeposition of MoS_x Hydrogen Evolution Catalysts from Sulfur-Rich Precursors. ACS Appl. Mater. Interfaces 11(36):32879–32886

26. Bard AJ, Mirkin MV (eds) (2012) Scanning electrochemical microscopy, 2nd ed. CRC Press, Boca Raton, Fla.

27. Polcari D, Dauphin-Ducharme P, Mauzeroll J (2016) Scanning Electrochemical Microscopy: A Comprehensive Review of Experimental Parameters from 1989 to 2015. Chem. Rev. 116(22):13234–13278

28. Sun T, Wang D, Mirkin MV, Cheng H, Zheng J-C, Richards RM, Lin F, Xin HL (2019) Direct high-resolution mapping of electrocatalytic activity of semi-two-dimensional catalysts with single-edge sensitivity. Proc. Natl. Acad. Sci. U. S. A. 116(24):11618–11623

29. Bertoncello P (2010) Advances on scanning electrochemical microscopy (SECM) for energy. Energy Environ. Sci. 3(11):1620

30. Jaouen K, Henrotte O, Campidelli S, Jousselme B, Derycke V, Cornut R (2017) Localized electrochemistry for the investigation and the modification of 2D materials. Appl. Mater. Today 8:116–124

31. Sauter S, Wittstock G (2001) Local deposition and characterisation of $K_2Co[Fe(CN)_6]$ and $K_2Ni[Fe(CN)_6]$ by scanning electrochemical microscopy. J. Solid State Electrochem. 5(3):205–211

32. Fedorov RG, Mandler D (2013) Local deposition of anisotropic nanoparticles using scanning electrochemical microscopy (SECM). Phys. Chem. Chem. Phys. 15(8):2725–2732

33. Liberman I, He W, Shimoni R, Ifraemov R, Hod I (2020) Spatially confined electrochemical conversion of metal-organic frameworks into metal-sulfides and their in situ electrocatalytic investigation via scanning electrochemical microscopy. Chem. Sci. 11(1):180–185

34. Iffelsberger C, Vatsyayan P, Matysik F-M (2017) Scanning Electrochemical Microscopy with Forced Convection Introduced by High-Precision Stirring. Anal. Chem. 89(3):1658–1664

35. Kai T, Chen S, Monterroso E, Zhou F (2015) Continuous nanoflow-scanning electrochemical microscopy: voltammetric characterization and application for accurate and reproducible imaging of enzyme-labeled protein microarrays. Anal. Chem. 87(8):4523–4529

36. Iffelsberger C, Raith T, Vatsyayan P, Vyskočil V, Matysik F-M (2018) Detection and imaging of reactive oxygen species associated with the electrochemical oxygen evolution by hydrodynamic scanning electrochemical microscopy. Electrochim. Acta 281:494–501

37. Momotenko D, Cortes-Salazar F, Lesch A, Wittstock G, Girault HH (2011) Microfluidic push-pull probe for scanning electrochemical microscopy. Anal. Chem. 83(13):5275–5282

38. Raith T, Wert S, Iffelsberger C, Matysik F-M (2018) Development and characterization of electrochemical flow cells for hydrodynamic scanning electrochemical microscopy. Monatsh. Chem. 149(9):1671–1677

39. Lee C, Miller CJ, Bard AJ (1991) Scanning electrochemical microscopy: preparation of submicrometer electrodes. Anal. Chem. 63(1):78–83

40. Stratmann L, Clausmeyer J, Schuhmann W (2015) Non-destructive Patterning of Carbon Electrodes by Using the Direct Mode of Scanning Electrochemical Microscopy. ChemPhysChem 16(16):3477–3482

41. Morales-Guio CG, Hu X (2014) Amorphous molybdenum sulfides as hydrogen evolution catalysts. Acc. Chem. Res. 47(8):2671–2681

4.5. Edges more electroactive than basal planes in crystalline TiS_2 and $TiSe_2$

Stefan Wert, Christian Iffelsberger, Katarina A. Novčić, Frank-Michael Matysik and Martin Pumera

Submitted for publication

This chapter was submitted for publication and was changed for reasons of uniformity. The changes herein consist of minor corrections, formatting, and the addition of the supporting information to the main text.

Abstract

Layered materials and derived 2D material couples such as graphite/graphene, layered and single layer pnictogens (i.e., black phosphorus and phosphorene) and transition metal dichalcogenides (TMDs) have gained a lot of attention due to their electrocatalytic properties and as potential materials for energy storage. Previous studies have shown that graphite, MoS_2 and pnictogens exhibit faster electron transfer at the edges of crystals and defects than on the basal plane. The persisting question is if this is a general trend in nature. To come closer to the answer of this question, we studied TiS_2 and $TiSe_2$ regarding their local catalytic activity via scanning electrochemical microscopy. Both TMDs have shown increased catalytic activity near edges and defects. For correlation, optical and topographical analysis was performed via scanning electron microscopy and atomic force microscopy. We show that the increased electrochemical activity at edges and defects is persistent across the layered materials. This is of huge industrial and scientific importance and there are very important implications for applications of layered materials.

4.5.1. Introduction

In the search for earth-abundant and environmental-friendly materials for energy storage and water splitting for the generation of hydrogen, 2D materials such as graphite [1–4] and layered pnictogens [5] (e.g. black phosphorous [6]) were found to be powerful candidates. Layered transition metal dichalcogenides (TMDs) are another large group of potential materials [7–11]. With the chemical composition MX_2, where M is a transition metal from groups IV to VII B (like Mo, W, Ti) and X is a chalcogenide (S, Se, Te), numerous elemental combinations can be realized. Due to their layered structure and strong covalent bonding within single layers, but weak interaction between layers because of van der Waals forces, these materials show anisotropy with respect to their electrical, mechanical and electrochemical properties. Single

or few layers can be prepared easily via exfoliation [12, 13] and the resulting 2D materials show a wide range of potential applications such as for energy storage [14, 15], sensing [16], and solar cells [17]. Most prominently, they are potent electrocatalysts for the hydrogen evolution reaction [18]. Among TMDs, group VI members have been studied extensively so far, with MoS_2 being the most popular as it is competitive with platinum as catalyst for hydrogen evolution reaction [19].

Most notably, graphite/graphene [1, 3, 4, 20], layered pnictogens [5] (e.g. black phosphorous [6]), and group VI TMDs [7–10, 21–24] show increased electron transfer rates and increased electrocatalytic activity at the edges and defects compared to basal planes (illustrated in **Figure 4.5.1**). This arises the question whether this is a phenomenon generally occurring in 2D materials. Therefore, we decided to study TiS_2 and $TiSe_2$ as representatives of group IV TMDs, which have not been investigated in this regard so far.

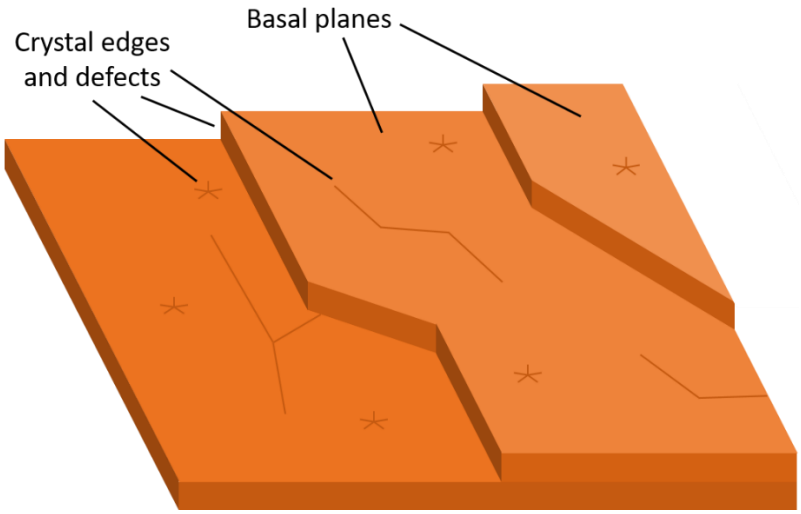

Figure 4.5.1: Schematic view of the surface structure of layered 2D-materials like graphite, layered pnictogens and TMDs.

Generally, due to different coordination in the individual layers, group IV (octahedral 1T-phase) and VI TMDs (prismatic 2H phase) show different properties [25, 26]. Group IV TMDs have attracted attention as they provide advantages over group VI TMDs like enhanced thermoelectric performance [27], high room-temperature mobility [28], ability to exhibit charge density wave [29], and high conductivity and theoretical capacity [30]. Furthermore, they are considered as storage material in sodium and potassium ion batteries as alternatives to lithium ion batteries [31, 32].

To investigate if group IV TMDs exhibit differences between basal plane and edge electrochemical activity, we used scanning electrochemical microscopy (SECM) over pristine TiS_2 and $TiSe_2$ surfaces for the localized imaging of the electrochemical activity. The obtained recordings were compared to scanning electron microscope (SEM), energy dispersive X-ray

spectroscopy (EDS), and atomic force microscopy (AFM) images for correlating the electrochemical response with surface morphology and elemental composition.

4.5.2. Experimental

4.5.2.1. Materials and methods

TMD crystals (TiS_2, $TiSe_2$) were obtained from 2d-age.com. Two-component epoxy resin was purchased from Struers Aps, Denmark. Graphite powder (<20 µm, synthetic) was bought from Sigma-Aldrich, Germany. Carbon SEM stubs were purchased from Micro to Nano, Netherlands. Polydimethylsiloxane (PDMS, SYLGARD™ 184) was obtained from Dow Inc., Michigan, USA. Potassium ferricyanide ($K_3Fe(CN)_6$) and potassium chloride (KCl) were purchased from Merck, Germany. Solutions were prepared with deionized water with a resistance >18 MΩ cm^{-1} (Milli-Q Advantage A10 system, Merck Millipore, Germany). All chemicals were of analytical grade and used as bought.

4.5.2.2. Crystal preparation

The sample preparation process is schematically shown in **Figure 4.5.2**. For the fabrication of flat samples, the TMD crystals were embedded in an electrically conductive blend of graphite powder and epoxy resin with a mass ratio of 1:1 on carbon SEM stubs. About 250 mg of the mixture were spread on the stub surface and pressed on a TMD crystal placed on a flat PDMS layer in a petri dish. After 24 h, the graphite/epoxy blend hardened, and the sample was carefully removed from the PDMS. Afterwards, a clean sample with a pristine crystal surface was ensured by removal of the upper crystal layers according to the “scotch tape” method [33].

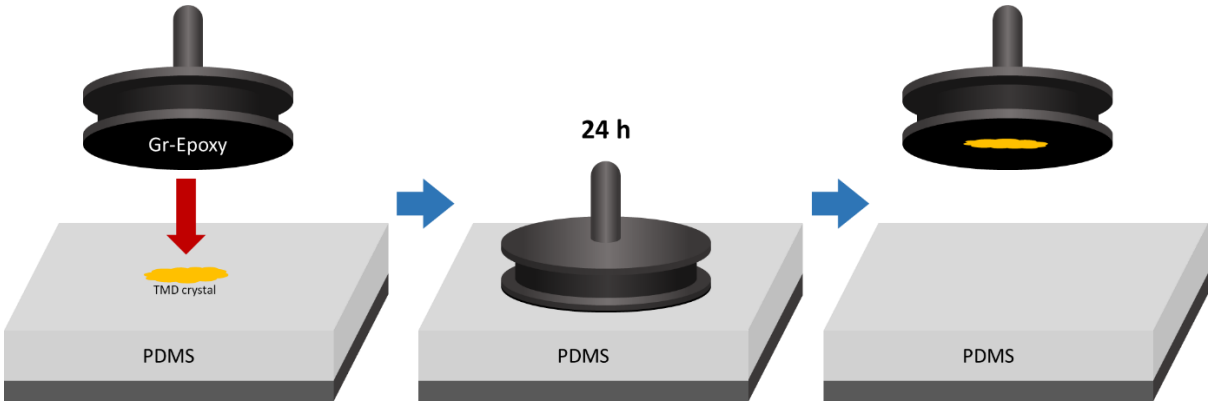

Figure 4.5.2: Preparation of crystal samples. A sample holder covered with graphite epoxy mixture (Gr-Epoxy) was pressed onto a crystal placed on a thin layer of PDMS. After 24 h, the sample holder with the crystal was removed as the epoxy resin had hardened.

4.5.2.3. Characterization

Electrochemical experiments were carried out with a commercial SECM (Sensolytics, Germany) and connected to a bipotentiostat (PGSTAT302N, Autolab, Netherlands). All potentials refer to a Ag/AgCl/3M reference electrode. A Pt wire served as counter electrode. Electrical contact to crystal samples was established with conductive copper tape. The electrochemical cell consisted of two parts screwed together, with the sample placed in between. Images of the assembly are shown in **Figure 4.5.3**.

SECM imaging was conducted with 10 and 25 µm diameter Pt disk ultramicroelectrodes (UMEs, RG > 10, Sensolytics, Germany) in a solution of $K_3Fe(CN)_6$. Prior to imaging, the probe was positioned at the respective substrate-to-tip distance as follows: A probe approach curve towards the sample surface was performed until surface contact and the approach was stopped manually. Afterwards the probe was retracted from the surface by 10 µm (TiS_2) or 15 µm ($TiSe_2$). At these substrate-to-tip distances, SECM images were recorded with a pixel size of 10 µm and a maximum probe velocity of 300 µm s^{-1}. Feedback mode images were obtained with a probe potential of E_{UME} = –0.2 V applied and the substrate remaining at open circuit potential, while substrate generation/tip collection (SG/TC) images were recorded with substrate and probe potentials of $E_{Substrate}$ = –0.5 and E_{UME} = 0.4 V, respectively. Data processing of SECM images was done with Gwyddion 2.55 and Origin 2020 software.

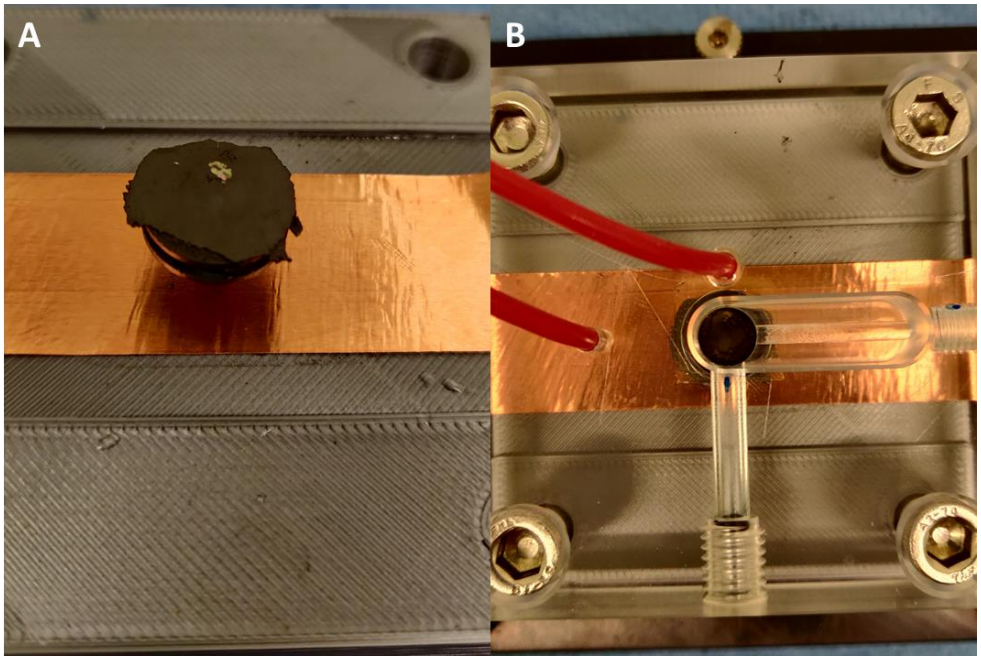

Figure 4.5.3A: TMD Crystal sample on the bottom piece of the measurement cell with copper tape for electrical contact. **B:** Assembled measurement cell with placeholders for counter and reference electrodes.

Correlation of the AFM positions was achieved via optical images recorded prior to performing AFM (Dimension Icon with Airasyst cantilever, Bruker, USA). SEM and EDS were conducted

with a MIRA 3 SEM (Tescan, Czech Republic) and an XFlash 5010 EDS (Bruker, USA) with an accelerating voltage of 20 kV used.

4.5.3. Results and discussion

Images of TiS_2 obtained via SEM (**Figure 4.5.4A**) revealed a flat crystal structure surrounded by highly conductive graphite epoxy resin. Multiple edges and cracks within the crystal were visible. EDS (**Figure 4.5.5**) showed the presence of mainly Ti and S in the crystal surface. A homogeneous oxygen distribution was indicated with slight deviations at the cracks in the surface. The electrochemical activity was analyzed locally (yellow box in **Figure 4.5.4A**) via SECM performed in feedback and SG/TC mode (**Figure 4.5.4B** and **C**, respectively). The feedback mode imaging, where the mediator species is converted at the probe in dependence of the sample conductivity, revealed generally uniform conductivity over the entire crystal area. The orange-colored area corresponds to the highly conductive carbon surface of the graphite-epoxy mixture, which was surrounding the crystal. On the crystal itself, small deviations correlate with topographic defects visible in the SEM image. In contrast, the SG/TC mode indicated differences in the local electrochemical activity as the mediator is reduced at the sample and the generated species is subsequently collected at the probe. The current scale in the images was adjusted to highlight the activity on the crystal surface. The original SG/TC image is given in **Figure 4.5.6**. The comparison with SEM shows that some of the poorly visible edges exhibit a high activity, while other more visible edges did not appear to be considerably electrochemically active. To further analyze size and morphology of the edges, AFM was conducted at two different locations of the crystal to cover edges of high and low electrochemical activity. Their positions relative to SEM and SECM images are indicated in **Figure 4.5.4A-C**. In **Figure 4.5.4D**, an AFM image of a highly catalytic edge is shown. It appeared as a sharp step of 200 nm height difference. The extracted line in **Figure 4.5.4E** confirmed that observation. For comparison, another AFM image of an edge exhibiting no noticeable increase of activity was obtained at position F (**Figure 4.5.4F**). The edge appeared convoluted and considerably rougher than the edge investigated in **Figure 4.5.4D**. Furthermore, it incorporated multiple smaller cracks. The extracted line in **Figure 4.5.4G** shows that the edge consisted of a convolution of about 1 µm thickness followed by another step of 800 nm height. Despite its relatively large height difference, no considerable increase of electrochemical activity occurred. In contrast, at the 200 nm edge in **Figure 4.5.4D**, a current increase of about 2 nA was detected. Since previous localized studies with MoS_2 and WS_2 have shown increased catalytic activity at edges compared to basal planes [21, 23, 24], we conclude that the same occurs in case of TiS_2. However, edge size did not correlate with activity in this case.

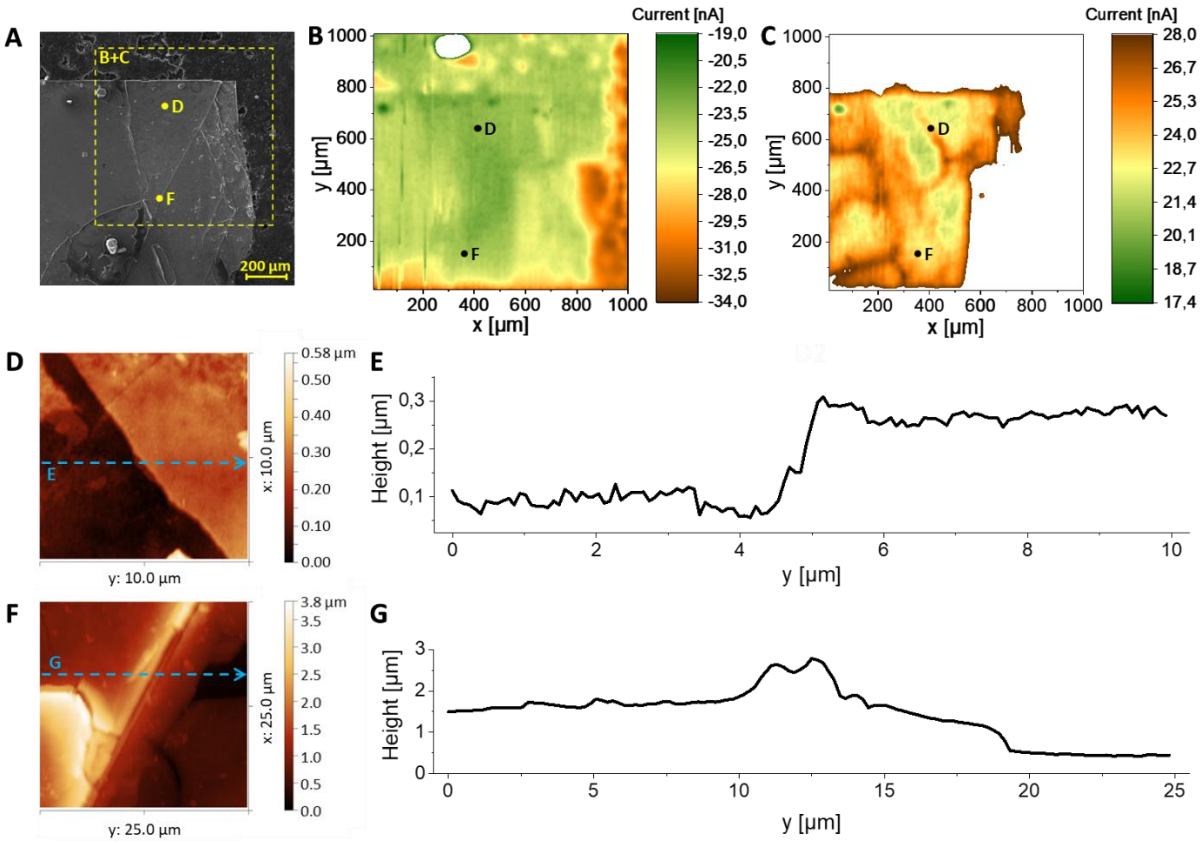

Figure 4.5.4: Characterization of the TiS_2 crystal. **A:** Scanning electron micrograph including indicators for the imaging locations of SECM recordings **B/C** (dashed box) and AFM images **D/F** (dots). **B/C:** SECM images of the crystal recorded in feedback (**B**) and SG/TC (**C**) mode in 10 mM $K_3Fe(CN)_6$ as mediator. Probe diameter: 25 µm; Pixel size: 10 µm; Substrate-to-tip distance: 10 µm. E_{UME} = –0.2 V (**B**), 0.4 V (**C**). $E_{Substrate}$ = –0.5 V (**C**) **D/F:** AFM images of crystal edges at the positions indicated in **A-C**. **E/G:** Line profiles extracted from **D/F**, respectively.

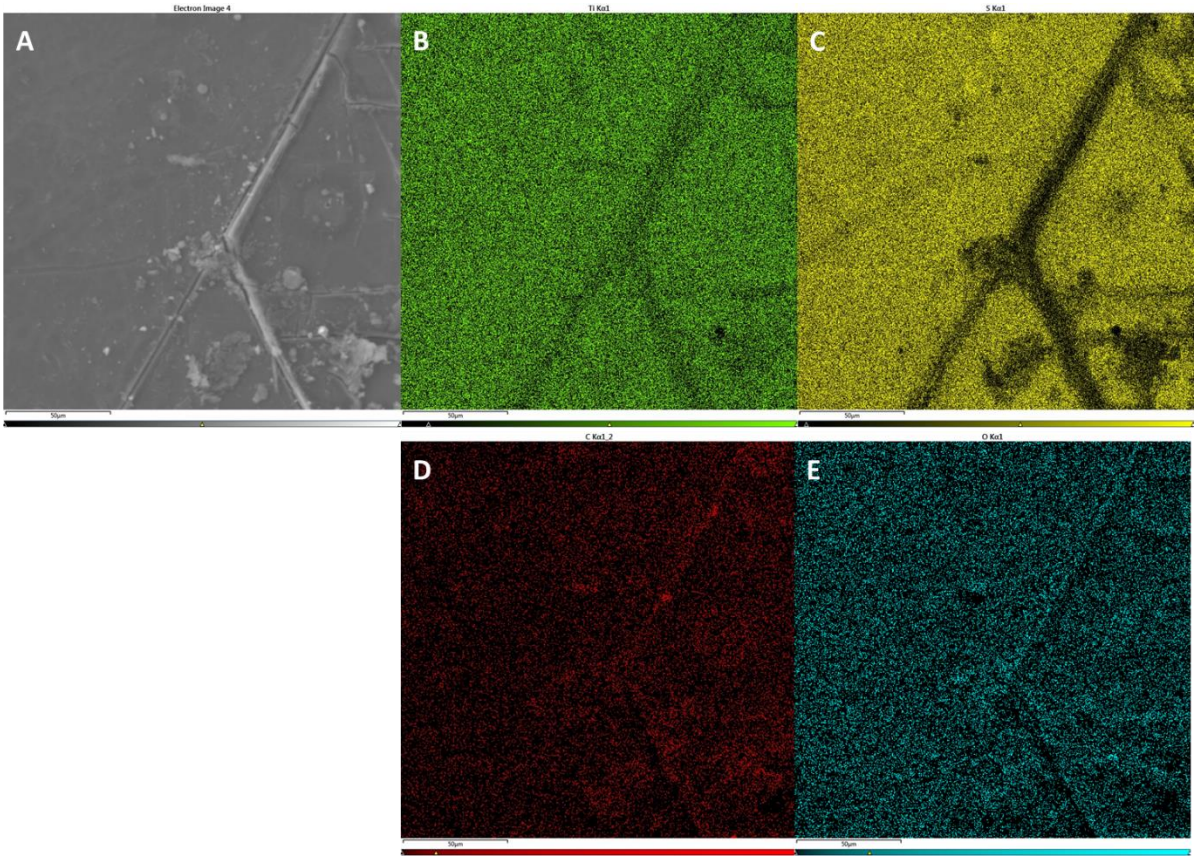

Figure 4.5.5: Scanning electron micrograph (**A**) and EDS elemental maps of TiS_2 for Ti (**B**), S (**C**), C (**D**), and O (**E**).

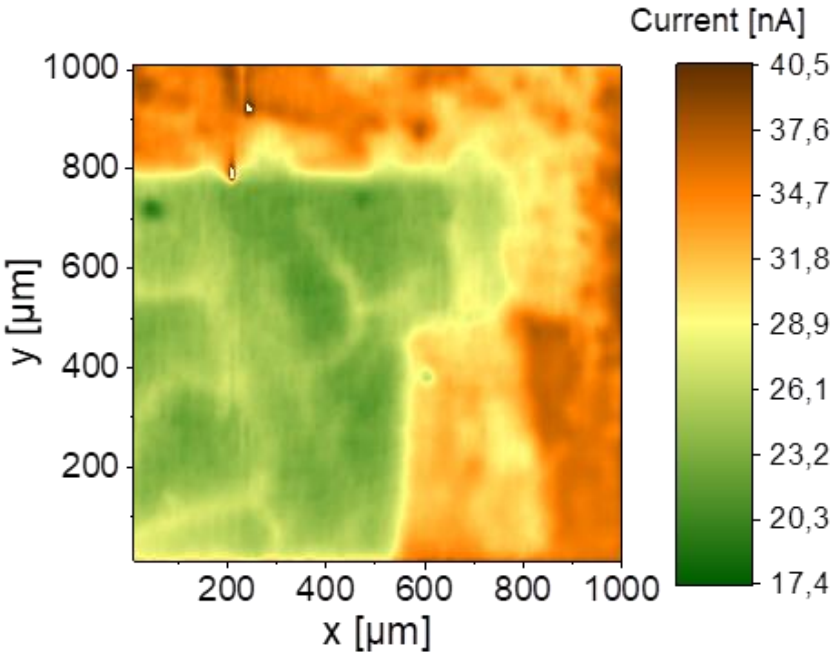

Figure 4.5.6: SG/TC SECM image of the TiS_2 sample from **Figure 4.5.3C** with expanded current range.

The SEM micrograph of the $TiSe_2$ crystal (**Figure 4.5.7A**) indicated a very rough surface at the crystal borders and in the top left region. Nevertheless, the crystal appears predominantly flat, especially in the top right region. Notably, a slightly brighter appearing area can be seen in the

bulk crystal (red boxes), where a lower amount of oxygen compared to the other parts of the crystal was determined via EDS (**Figure 4.5.7B**) which might indicate a local difference in surface composition. EDS maps of other elements are presented in **Figure 4.5.8**, showing a homogeneous distribution along the crystal surface. Afterwards, the area highlighted by the yellow box was studied via SECM in feedback and SG/TC mode (**Figure 4.5.7C** and **D**). The feedback image shows a low but uniform conductivity in the flat parts of the crystal. The orange areas in **Figure 4.5.7C** correlate with the rough and dark areas visible in the SEM image that show the graphite-epoxy resin. In SG/TC mode, the crystal surface shows apparent differences in the electrochemical activity. Especially the regions of the crystal with a rough topography (dark green in **Figure 4.5.7C**) became remarkably active in the shape of multiple small spots of exceedingly high activity located near the edge of the crystal in the bottom right of the image. According to the SEM image, this region contained many cracks in the surface that possibly exposed a large number of active edges. Most notably, the region corresponding to a decreased oxygen content exhibited an increased electrochemical activity, which could also be due to a different grade of oxygen content on the surface, as suggested by the EDS elemental map of oxygen. This observation is in line with activity differences occurring at group VI TMDs due to the formation of surface oxides [34].

In this region, the electrochemical activity transition between high and low oxygen content was further investigated via AFM imaging, together with another spot for comparison in the low oxygen area incorporating an edge. The exact locations are indicated in **Figure 4.5.7A**, **C**, and **D**. **Figure 4.5.7E** shows the AFM image obtained at the transition from low to high oxygen content showing a straight and clear edge. The bright part below the edge corresponds to the area of high oxygen content, while low amounts of oxygen were determined to be on the other side. The extracted line in **Figure 4.5.7F** shows a sharp edge with a height difference of 300 nm and a higher surface roughness in the low oxygen area. The increased roughness (and thus surface area) and the decreased oxygen content, both might contribute to the increased electrochemical activity [34]. However, we assume that the oxygen content only has a minor effect on electrochemical activity since no conductivity difference was observed in the feedback mode SECM image. Furthermore, topography near an edge within the low oxygen content region was investigated via AFM as shown in **Figure 4.5.7G**. Similar to the first AFM image, the surface exhibited a considerable roughness. The line profile in **Figure 4.5.7H** going from left to right across the edge shows that the latter consists of an increase in height of 200 nm, followed by a decrease of about 400 nm. However, this edge is not visible in the SG/TC image in **Figure 4.5.7D**, which indicated that edges do not necessarily affect the electrochemical activity of the crystal. Nevertheless, the small areas of high activity in the very rough part of the crystal show that microscopic surface defects and edges can induce increased electrochemical activity. Nevertheless, basal planes did not appear completely

electrochemically inactive. This observation is in line with localized hydrogen evolution studies performed with group VI TMDs [21–23]. Furthermore, local differences in oxygen content on the surface contributed to inhomogeneities in activity, as higher oxygen concentration resulted in a reduced electrochemical activity of $TiSe_2$.

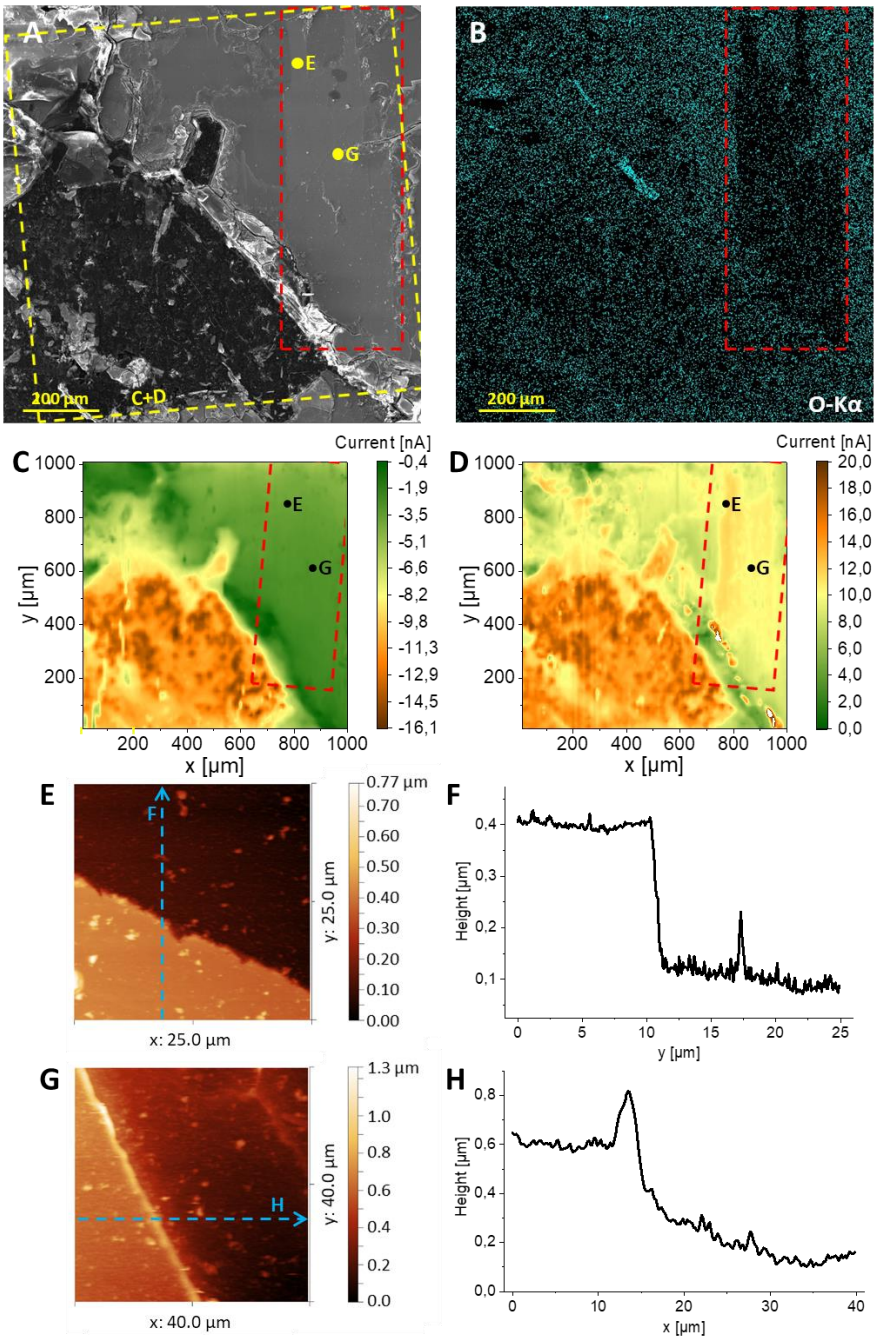

Figure 4.5.7: Characterization of the $TiSe_2$ crystal. **A:** Scanning electron micrograph of the $TiSe_2$ crystal. Imaging locations of SECM recordings **C/D** (yellow box) and AFM images **E/G** (dots) are highlighted. **B:** EDS map showing the oxygen distribution in the area covered by **A**. The red boxes in **A-D** highlight the location of low oxygen content. **C/D:** SECM images of the crystal recorded in feedback (**C**) and SG/TC (**D**) mode recorded in 10 mM $K_3Fe(CN)_6$. Probe diameter: 10 µm. Pixel size: 10 µm. Substrate-to-tip distance: 15 µm. E_{UME} = –0.2 V (**C**), 0.4 V (**D**). $E_{Substrate}$ = –0.5 V (**D**) **E/G:** AFM images of different crystal edges. **F/H:** Line profiles extracted from **E/G**.

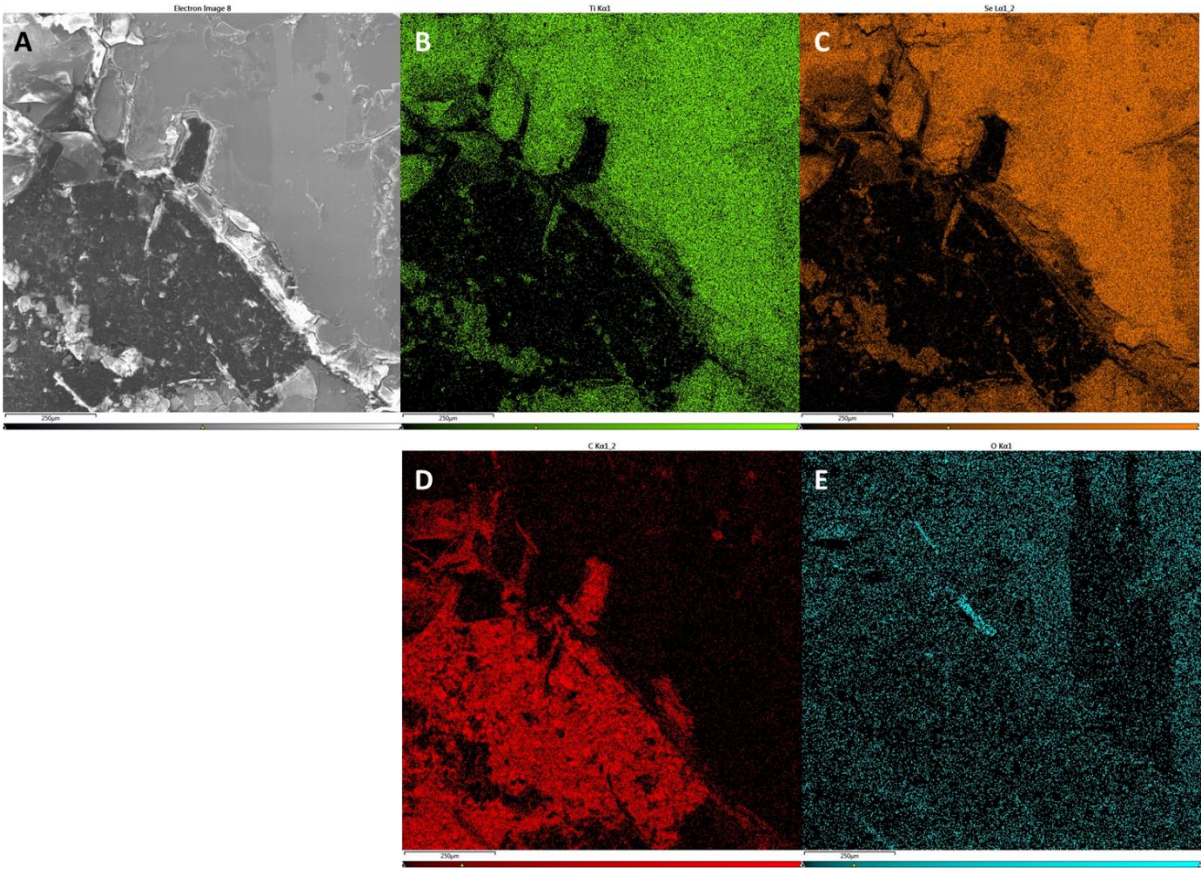

Figure 4.5.8: Scanning electron micrograph (**A**) and EDS elemental maps of $TiSe_2$ for Ti (**B**), Se (**C**), C (**D**), and O (**E**).

4.5.4. Conclusion

In this work, we tackled the persisting question if a higher electrochemical activity at the edges of crystals and defects is a general trend in nature. We showed that differences in electrochemical activity between basal planes and crystal edges and defects exist within the group IV TMDs TiS_2 and $TiSe_2$ shows analogies to other 2D materials like graphite, layered pnictogens and group VI TMDs. Localized electrochemical investigations performed via SECM over crystalline TiS_2 and $TiSe_2$ have shown an increased electrochemical activity at crystal edges and microscopic surface defects compared to basal planes. Further analyses utilizing SEM, EDS and AFM were employed to support these findings. Nevertheless, basal planes did not appear completely electrochemically inactive. Despite we could not answer the big question to the full extent, these results are important for the future development of alternative energy storage materials and electrocatalysts based on group IV TMDs.

References

1. Banks CE, Davies TJ, Wildgoose GG, Compton RG (2005) Electrocatalysis at graphite and carbon nanotube modified electrodes: edge-plane sites and tube ends are the reactive sites. Chem. Commun. (7):829–841
2. Davies TJ, Hyde ME, Compton RG (2005) Nanotrench arrays reveal insight into graphite electrochemistry. Angew. Chem. Int. Ed. 44(32):5121–5126
3. Neumann CCM, Batchelor-McAuley C, Downing C, Compton RG (2011) Anthraquinone monosulfonate adsorbed on graphite shows two very different rates of electron transfer: surface heterogeneity due to basal and edge plane sites. Chem. Eur. J. 17(26):7320–7326
4. Yuan W, Zhou Y, Li Y, Li C, Peng H, Zhang J, Liu Z, Dai L, Shi G (2013) The edge- and basal-plane-specific electrochemistry of a single-layer graphene sheet. Sci. Rep. 3:2248
5. Marvan P, Huber Š, Luxa J, Mazánek V, Sedmidubský D, Sofer Z, Pumera M (2019) Edge vs. basal plane electrochemistry of layered pnictogens (As, Sb, Bi): Does edge always offer faster electron transfer? Appl. Mat. Today 16:179–184
6. Sofer Z, Sedmidubský D, Huber Š, Luxa J, Bouša D, Boothroyd C, Pumera M (2016) Layered Black Phosphorus: Strongly Anisotropic Magnetic, Electronic, and Electron-Transfer Properties. Angew. Chem. Int. Ed. 55(10):3382–3386
7. Tan SM, Ambrosi A, Sofer Z, Huber Š, Sedmidubský D, Pumera M (2015) Pristine Basal- and Edge-Plane-Oriented Molybdenite MoS_2 Exhibiting Highly Anisotropic Properties. Chem. Eur. J. 21(19):7170–7178
8. Tsai C, Chan K, Abild-Pedersen F, Nørskov JK (2014) Active edge sites in $MoSe_2$ and WSe_2 catalysts for the hydrogen evolution reaction: a density functional study. Phys. Chem. Chem. Phys. 16(26):13156–13164
9. Tuxen A, Kibsgaard J, Gøbel H, Laegsgaard E, Topsøe H, Lauritsen JV, Besenbacher F (2010) Size threshold in the dibenzothiophene adsorption on MoS_2 nanoclusters. ACS Nano 4(8):4677–4682
10. Jaramillo TF, Jørgensen KP, Bonde J, Nielsen JH, Horch S, Chorkendorff I (2007) Identification of Active Edge Sites for Electrochemical H_2 Evolution from MoS_2 Nanocatalysts. Science 317(5834):100–102
11. Chia X, Eng AYS, Ambrosi A, Tan SM, Pumera M (2015) Electrochemistry of Nanostructured Layered Transition-Metal Dichalcogenides. Chem. Rev. 115(21):11941–11966

12. Novoselov KS, Jiang D, Schedin F, Booth TJ, Khotkevich VV, Morozov SV, Geim AK (2005) Two-dimensional atomic crystals. Proc. Natl. Acad. Sci. U. S. A. 102(30):10451–10453

13. Nicolosi V, Chhowalla M, Kanatzidis MG, Strano MS, Coleman JN (2013) Liquid Exfoliation of Layered Materials. Science 340(6139):1226419

14. Muller GA, Cook JB, Kim H-S, Tolbert SH, Dunn B (2015) High performance pseudocapacitor based on 2D layered metal chalcogenide nanocrystals. Nano Lett. 15(3):1911–1917

15. Chen D, Ji G, Ding B, Ma Y, Qu B, Chen W, Lee JY (2013) In situ nitrogenated graphene-few-layer WS_2 composites for fast and reversible Li^+ storage. Nanoscale 5(17):7890–7896

16. Wu S, Zeng Z, He Q, Wang Z, Wang SJ, Du Y, Yin Z, Sun X, Chen W, Zhang H (2012) Electrochemically reduced single-layer MoS_2 nanosheets: characterization, properties, and sensing applications. Small 8(14):2264–2270

17. Yu X, Sivula K (2016) Toward Large-Area Solar Energy Conversion with Semiconducting 2D Transition Metal Dichalcogenides. ACS Energy Lett. 1(1):315–322

18. Voiry D, Salehi M, Silva R, Fujita T, Chen M, Asefa T, Shenoy VB, Eda G, Chhowalla M (2013) Conducting MoS_2 nanosheets as catalysts for hydrogen evolution reaction. Nano Lett. 13(12):6222–6227

19. Pumera M, Sofer Z, Ambrosi A (2014) Layered transition metal dichalcogenides for electrochemical energy generation and storage. J. Mater. Chem. A 2(24):8981–8987

20. Güell AG, Cuharuc AS, Kim Y-R, Zhang G, Tan S-y, Ebejer N, Unwin PR (2015) Redox-dependent spatially resolved electrochemistry at graphene and graphite step edges. ACS Nano 9(4):3558–3571

21. Bentley CL, Kang M, Maddar FM, Li F, Walker M, Zhang J, Unwin PR (2017) Electrochemical maps and movies of the hydrogen evolution reaction on natural crystals of molybdenite (MoS_2): basal vs. edge plane activity. Chem. Sci. 8(9):6583–6593

22. Takahashi Y, Kobayashi Y, Wang Z, Ito Y, Ota M, Ida H, Kumatani A, Miyazawa K, Fujita T, Shiku H, Korchev YE, Miyata Y, Fukuma T, Chen M, Matsue T (2020) High-Resolution Electrochemical Mapping of the Hydrogen Evolution Reaction on Transition-Metal Dichalcogenide Nanosheets. Angew. Chem. Int. Ed. 59(9):3601–3608

23. Tao B, Unwin PR, Bentley CL (2020) Nanoscale Variations in the Electrocatalytic Activity of Layered Transition-Metal Dichalcogenides. J. Phys. Chem. C 124(1):789–798

24. Bentley CL, Kang M, Unwin PR (2019) Nanoscale Surface Structure-Activity in Electrochemistry and Electrocatalysis. J. Am. Chem. Soc. 141(6):2179–2193

25. Yan C, Gong C, Wangyang P, Chu J, Hu K, Li C, Wang X, Du X, Zhai T, Li Y, Xiong J (2018) 2D Group IVB Transition Metal Dichalcogenides. Adv. Funct. Mater. 28(39):1803305

26. Toh RJ, Sofer Z, Pumera M (2016) Catalytic properties of group 4 transition metal dichalcogenides (MX_2 ; M = Ti, Zr, Hf; X = S, Se, Te). J. Mater. Chem. A 4(47):18322–18334

27. Wan C, Gu X, Dang F, Itoh T, Wang Y, Sasaki H, Kondo M, Koga K, Yabuki K, Snyder GJ, Yang R, Koumoto K (2015) Flexible n-type thermoelectric materials by organic intercalation of layered transition metal dichalcogenide TiS_2. Nature Mater. 14(6):622–627

28. Zhang W, Huang Z, Zhang W, Li Y (2014) Two-dimensional semiconductors with possible high room temperature mobility. Nano Res. 7(12):1731–1737

29. Sun L, Chen C, Zhang Q, Sohrt C, Zhao T, Xu G, Wang J, Wang D, Rossnagel K, Gu L, Tao C, Jiao L (2017) Suppression of the Charge Density Wave State in Two-Dimensional 1T-$TiSe_2$ by Atmospheric Oxidation. Angew. Chem. Int. Ed. 56(31):8981–8985

30. Tao H, Zhou M, Wang R, Wang K, Cheng S, Jiang K (2018) TiS_2 as an Advanced Conversion Electrode for Sodium-Ion Batteries with Ultra-High Capacity and Long-Cycle Life. Adv. Sci. 5(11):1801021

31. Tang J, Huang X, Lin T, Qiu T, Huang H, Zhu X, Gu Q, Luo B, Wang L (2020) MXene derived TiS_2 nanosheets for high-rate and long-life sodium-ion capacitors. Energy Storage Mater. 26:550–559

32. Li P, Zheng X, Yu H, Zhao G, Shu J, Xu X, Sun W, Dou SX (2019) Electrochemical potassium/lithium-ion intercalation into $TiSe_2$: Kinetics and mechanism. Energy Storage Mater. 16:512–518

33. Novoselov KS, Geim AK, Morozov SV, Jiang D, Zhang Y, Dubonos SV, Grigorieva IV, Firsov AA (2004) Electric field effect in atomically thin carbon films. Science (New York, N.Y.) 306(5696):666–669

34. Eng AYS, Ambrosi A, Sofer Z, Šimek P, Pumera M (2014) Electrochemistry of transition metal dichalcogenides: strong dependence on the metal-to-chalcogen composition and exfoliation method. ACS Nano 8(12):12185–12198

5. Summary

In this thesis, multiple instrumental additions to the SECM were successfully implemented into the setup that led to the general enhancement of the instruments' performance. When imaging samples with complex topography and electrochemical behavior, conventional amperometric SECM imaging cannot be used to distinguish topography and electrochemical activity as both contribute to the overall response. To distinguish these two characteristics, SICM can be employed since it delivers purely topographical information. Therefore, a simple and cost-efficient method for the fabrication of probes usable for simultaneous SECM and SICM was developed. Probes fabricated according to this concept were applied for the localized electrochemical characterization of porous BDD samples, showing that the material exhibited differences in electrochemical activity, which were presumably based on local differences in boron doping level.

As temperature differences introduce hydrothermal convection and elevated temperatures generally increase the reaction rate, the concept of "hot-wire electrochemistry" as a method of non-isothermal heating was introduced into the SECM setup since a positive impact on SECM imaging was expected. This project involved the design and fabrication of substrates that featured a flattened platinum microwire as substrate electrode that could be heated by the application of a high-frequency alternating current. Heating of the substrate resulted in a highly increased mass transport at the wire, which in turn led to SECM images of the wire exhibiting a higher contrast compared to room temperature imaging.

In a follow-up project, the previously developed heat-adjustable substrates in combination with SECM were used for the localized characterization of the activity of the enzyme glucose oxidase under the impact of long-term (30 s) or short-term (100 ms) heating. The enzyme, immobilized on the platinum wire of the substrate, showed that long-term application of 42 °C already led to a significant loss of enzyme activity, while short pulses of up to 79 °C could be applied without damaging the enzyme. Furthermore, SECM imaging revealed the localized consequences of heating. Long-term heat application caused enzyme degradation in a larger area of the substrate, while short pulses even at 106 °C mainly caused a loss of enzyme activity close to the wire. In addition, pulsed heating has shown to yield up to a 22-fold increase of glucose oxidase sensitivity towards glucose.

One side project included in this thesis involved the introduction of forced convection into SECM measurements. This concept was already established by previous work of our group and was proven to yield higher reproducibility and contrast of SECM images in feedback and SG/TC modes. The work in this field was expanded during this thesis as a 3D-printed electrochemical flow cell combined with a syringe pump was utilized for the generation of forced convection. The setup was characterized and compared to a previously developed

electrochemical flow cell based on PTFE, showing comparable and reproducible electrochemical response in generation/collection modes of SECM. Furthermore, this 3D-printed cell served as miniaturized prototype for an electrochemical flow reactor in which it is possible to (re)place electrocatalyst using SECM.

In a final side project, the highly spatially resolved analysis of the electrocatalytic activity of crystalline TiS_2 and $TiSe_2$ as representatives for layered group IV TMDs was conducted. Since other layered materials such as graphite, layered pnictogens and group VI TMDs exhibit a higher electrochemical activity at crystal edges compared to basal planes, it was investigated if the same is true for group IV TMDs. This trend could be confirmed as higher electrochemical currents were measured at edges of TiS_2 and $TiSe_2$ in SG/TC mode SECM. For correlation of the results, SEM, EDS, and AFM were utilized.

In summary, the following SECM configurations with different advantages and fields of application were developed:

- Cost-efficient, combined SECM and SICM for distinguishing electrochemical and topographical information
- Easily accessible flow cell setup containing of a 3D-printed flow cell and a syringe pump for the generation of forced convection, yielding increased contrast and reproducibility
- Heatable substrates for higher contrast and reproducibility of SECM measurements, in addition to the possibility to carry out localized studies of temperature-dependent electrochemical processes

6. Zusammenfassung in deutscher Sprache

In dieser Arbeit wurden mehrere instrumentelle Erweiterungen für das SECM implementiert, welche allgemein zu einer besseren Performance des Instruments führten. Bei Aufnahmen von Proben mit komplexer Topografie und elektrochemischen Verhalten können mittels konventionellem amperometrischen SECM Unterschiede zwischen Topografie und elektrochemischer Aktivität nur bedingt festgestellt werden, da beide Eigenschaften den gemessenen Strom beeinflussen. Um diese beiden Charakteristika zu unterscheiden, kann SICM angewandt werden, da diese Technik ausschließlich topografische Information liefert. Deshalb wurde eine simple und kostengünstige Methode zur Herstellung von Sonden entwickelt, welche für die gleichzeitige Durchführung von SICM- und SECM-Messungen geeignet sind. Sonden, die nach diesem Prinzip hergestellt wurden, wurden für die lokale elektrochemische Charakterisierung von porösen BDD-Proben verwendet. Auf diese Weise konnte gezeigt werden, dass das Material lokale Unterschiede bezüglich elektrochemischer Aktivität aufweist, die vermutlich durch lokale Unterschiede im Bordotierungsgrad bedingt sind.

Da Temperaturunterschiede hydrothermale Konvektion erzeugen, erhöhte Temperaturen im Allgemeinen die Reaktionsrate steigern und beide Effekte als vorteilhaft für SECM-Aufnahmen angenommen wurden, wurde das nicht-isotherme Heizverfahren namens „Heißdraht-Elektrochemie“ mit dem SECM kombiniert. Dieses Projekt beinhaltete das Design und die Fertigung von Substraten, welche unter anderem aus einem abgeflachten Platinmikrodraht als heizbarer Substratelektrode bestanden, der durch das Anlegen einer hochfrequenten Wechselspannung geheizt werden konnte. Das Heizen des Substrats führte zu einem stark erhöhten Massentransport am Draht. Infolgedessen zeigten SECM-Bildaufnahmen des Drahts einen höheren Kontrast im Vergleich zu Aufnahmen, die bei Raumtemperatur entstanden sind.

In einem Nachfolgeprojekt wurden die zuvor entwickelten, heizbaren Substrate in Kombination mit SECM verwendet, um die Enzymaktivität von Glucoseoxidase unter sowohl langfristigem (30 s) als auch kurzfristigem (100 ms) Heizen zu untersuchen. Das Enzym wurde auch dem Platindraht eines Substrats immobilisiert und zeigte nach langfristigem Anlegen von bereits 42 °C einen signifikanten Verlust der Enzymaktivität. Im Vergleich dazu konnten kurzzeitige Heizpulse von bis zu 79 °C ohne Aktivitätsverlust appliziert werden. Des Weiteren zeigten SECM-Bildaufnahmen die lokalen Änderungen der Enzymaktivität infolge des Heizens. Langfristiges Heizen führte zu weitläufigem Verlust der Enzymaktivität, während kurzfristiges Heizen selbst bei 106 °C nur einen Aktivitätsverlust nahe dem Draht verursacht hat. Zusätzlich konnte gezeigt werden, dass Heizpulse zu einer bis zu 22-fach erhöhten Empfindlichkeit von Glucoseoxidase gegenüber Glucose führten.

Ein Nebenprojekt dieser Arbeit bezog sich auf das Einbringen von forcierter Konvektion in SECM-Messungen. Das Konzept wurde bereits in vorhergehenden Projekten unserer

Arbeitsgruppe etabliert und hat nachweislich zu einer höheren Reproduzierbarkeit und höherem Kontrast von SECM-Bildaufnahmen geführt. In dieser Arbeit wurde das Projekt weitergeführt, indem eine 3D-gedruckte elektrochemische Flusszelle entwickelt wurde, in welcher mittels Spritzenpumpe forcierte Konvektion erzeugt wurde. Der Messaufbau wurde charakterisiert und mit einem Setup aus einem vorhergehenden Projekt verglichen, welches eine PTFE-Flusszelle beinhaltete. Beide Aufbauten zeigten vergleichbares und reproduzierbares elektrochemisches Verhalten in den Generation/Collection-Modi des SECM. Des Weiteren diente die 3D-gedruckte Zelle als miniaturisierter Prototyp eines elektrochemischen Flussreaktors, in welchem mittels SECM Elektrokatalysator abgeschieden und erneuert werden konnte.

In einem letzten Nebenprojekt wurden TiS_2 und $TiSe_2$ als Vertreter der geschichteten TMDs der Gruppe IV hochauflösend bezüglich ihrer elektrokatalytischen Aktivität untersucht. Da andere Schichtmaterialen wie zum Beispiel Graphit, geschichtete Pnictogene oder TMDs der Gruppe VI eine erhöhte elektrochemische Aktivität an Kristallkanten im Vergleich zu Basalflächen aufweisen, wurde untersucht, ob dasselbe auch für TMDs der Gruppe IV gilt. Dieser Trend konnte bestätigt werden, da erhöhte elektrochemische Ströme an Kanten von TiS_2 und $TiSe_2$ mittels SECM im SG/TC-Modus gemessen werden konnten. Die Ergebnisse konnten durch SEM-, EDS- und AFM-Aufnahmen korreliert werden.

Zusammengefasst wurden folgende erweiterte SECM-Messaufbauten mit unterschiedlichen Vorteilen und Anwendungsgebieten konzipiert:

- Kosteneffizientes, kombiniertes SECM und SICM zum Entkoppeln von elektrochemischer und topografischer Information
- Einfach zugänglicher Flusszellenaufbau bestehend aus 3D-gedruckter Flusszelle mit Spritzenpumpe zur Generierung forcierter Konvektion für höheren Kontrast und reproduzierbarere Messungen
- Heizbare Substrate für höhere Kontraste und reproduzierbarere SECM-Messungen und zur lokalen Untersuchung von temperaturabhängigen elektrochemischen Prozessen

Eidesstattliche Erklärung

Ich habe die vorliegende Arbeit selbstständig verfasst, keine anderen als die angegebenen Quellen und Hilfsmittel benutzt und bisher keiner anderen Prüfungsbehörde vorgelegt. Von den in §27 Abs. 5 vorgesehenen Rechtsfolgen habe ich Kenntnis genommen.

Regensburg, den 15. April 2021

_____

Stefan Wert